



universität
wien

DISSERTATION

Titel der Dissertation

Structure and assembly mechanism of TbBILBO1, an
essential flagellar pocket collar protein

Verfasser

Keni Vidilaseris

angestrebter akademischer Grad

Doctor of Philosophy (PhD)

Wien, 2014

Studienkennzahl lt. Studienblatt:

A 094 490

Dissertationsgebiet lt. Studienblatt:

Molekulare Biologie

Betreuer:

Dr. Gang Dong

Acknowledgements

All praises and thanks to the grace of almighty God (**Allah**), the Beneficent, the Merciful, and the supreme source of all knowledge. To Him do I serve and to Him I ask for help. I submit in obedience before my Lord, who gave me the strength and drive to achieve this task and made me reach this present pedestal of knowledge.

I would like to thank my supervisor **Dr. Gang Dong** for giving me the opportunity to do my PhD studies in his lab. I am very grateful for his keen interest, genial behavior, constant support and guidance during my studies.

I am grateful to **Dr. Brooke Morriswood** for his kindness, honesty and sharp scientific discussion during my studies, and for the time spent checking manuscripts and my dissertation. I also thank **Prof. Georg Kontaxis** for his help and support with NMR structure determination and discussion.

I thank my PhD committee members: **Prof. Graham Warren**, who gave me valuable feedback and input throughout my project and allowed me to join his group meetings to enhance my scientific knowledge; **Prof. Robert Konrat**, for valuable discussions and for teaching me the basic principles of NMR spectroscopy; and **Dr. Sasha Martens** for discussion and experimental help with the liposome binding assays.

I thank **Gunter Resch** and **Marlene Brandstetter** for their help in preparing rotary metal shadowing grids and recording electron micrographs.

I would like to thank past and present lab members **Ekaterina Shimanovskaya**, **Clara Pleban**, **Renpin Qiao**, **Johannes Lesigang**, and **Yubo Zhang** for generating a great lab environment and a lot of funny and interesting discussions. And a special thanks to Ekaterina Shimanovskaya for recording electron micrographs and Johannes Lesigang for his technical assistance in the laboratory.

I thank also Graham Warren's Lab members (**Emine Seville Davidson Yavuz**, **Lars Demmel**, **Marco Sealey**, **Kyojiro Ikeda**, **Chris de Graffenried**, **Katharina Havlicek**,

Ana Lozano, Katy Schmidt, and Brooke Morriswood) for help, discussion and a nice environment during my working time with trypanosomes. And a special thanks to Ana for helping me with the FACS experiments, and Marco for the IC₅₀ experiment.

I thank **Kristina Djinovic-Carugo's Lab** and **Robert Konrat's Lab** for a lot of help and discussion during my studies. Special thank to **Muhammad Bashir Khan** for discussion, help, and company whenever I needed it. I thank also **Julius Konstan, Georg Mlynek, and Irina Grishkovskaya** for helping me during my work in the VBC5 for protein purification, crystallization, and X-ray diffraction measurements.

I thank my family – my parents **Suhada** and **Murniati**, my siblings **Helmy, Sylvia**, and **Indira** for their prayer and support for me at all times.

I thank my wife, **Fitri Nurfitriani**, for her constant support, faith and comfort during my last year of study.

I thank also all my **Indonesian friends** in Vienna for all of our happy and cheerful times together.

Last but not least, I would like to thank the **OeAD Asea-Uninet scholarship** for providing me with funding during my first three years of graduate study.

Abbreviations

1D	one dimensional
2D	two dimensional
3D	three dimensional
aa	amino acid
anti-GFP	anti – green fluorescent protein
aPKC	atypical protein kinase C
BioID	proximity-dependent biotin identification
BSF	bloodstream form
CCD	coiled-coil domain
CD	circular dichroism
CTD	C-terminal domain
DFMO	α -difluoromethylornithine
DNA	deoxyribonucleic acid
DRC	Democratic Republic of the Congo
DTT	dithiothreitol
EFh	EF-hand
EGFP	enhanced green fluorescent protein
EM	electron microscopy
ER	endoplasmic reticulum

ESRF	European Synchrotron Radiation Facility
FAZ	flagellum attachment zone
FL	full length
Fla1	flagellum adhesion glycoprotein
FP	flagellar pocket
FPC	flagellar pocket collar
GAPDH	glyceraldehyde 3-phosphate dehydrogenase
GPI-PLC	glycosylphosphatidylinositol-specific phospholipase C
GTP	guanosine triphosphate
hCLP	human calmodulin-like protein
HSQC	heteronuclear single quantum coherence
IPTG	isopropylthio- β -D-galactoside
kDa	kilodalton
kDNA	kinetoplast DNA
LAMP	lysosome-associated membrane protein
LZ	leucine zipper
MAPK	mitogen-activated protein kinase
MBP	maltose binding protein
MTOC	microtubule-organizing center
MtQ	microtubule quartet
MW	molecular weight
NMR	nuclear magnetic resonance

NOE	nuclear Overhauser effect
NTD	N-terminal domain
NECT	nifurtimox-elfornithine combination therapy
ODC	ornithine decarboxylase
PBS	phosphate-buffered saline
PCF	procyclic form
PCR	polymerase chain reaction
PDB	protein data bank
PEGMME	polyethylene glycol monomethyl ether
PFR	paraflagellar rod
PI	Phosphatidylinositol
PI3K	phosphoinositide 3-kinase
PI3P	Phosphatidylinositol 3-phosphate
RDCs	residual dipolar couplings
RNAi	RNA interference
SAD	single anomalous dispersion
SDS-PAGE	sodium dodecyl sulfate polyacrylamide gel electrophoresis
SEC	size exclusion chromatography
SeMet	seleno-methionine
SIF	stumpy induction factor
SLS	static light scattering
TAC	tripartite attachment complex

<i>Tb</i>	<i>Trypanosoma brucei</i>
TEV	<i>tobacco etch virus</i>
TOR	target of rapamycin
VSG	variant surface glycoprotein
YFP	yellow fluorescent protein
ZFK	zinc finger kinase

Table of Contents

1	Abstract.....	15
2	Zusammenfassung.....	16
3	Introduction	19
3.1	Sleeping sickness	19
3.2	Trypanosoma brucei	21
3.2.1	Life cycle of <i>T. brucei</i>	21
3.2.2	The cellular architecture of <i>T. brucei</i>	23
3.3	Flagellar Pocket.....	29
3.3.1	The function of flagellar pocket.....	30
3.3.2	Flagellar pocket biogenesis.....	33
3.4	Flagellar pocket collar.....	34
3.5	TbBILB01.....	36
3.6	Protein structure determination by multidimensional NMR spectroscopy	38
3.7	Protein structure determination by X-ray crystallography	46
4	Aims of the study.....	51
5	Materials and methods	53
5.1	Antibodies and reagents	53
5.2	Cloning and site-directed mutagenesis.....	53
5.3	Cell lines, culture and generation.....	55
5.4	Protein expression and purification.....	56

5.5	NMR spectroscopy and structure calculations.....	58
5.6	Crystallization and data collection of the N-terminal domain of TbBILBO1	59
5.7	Crystallization of the complex TbBILBO1-NH and TbBILBO1-CH.....	60
5.8	Rotary metal shadowing electron microscopy.....	60
5.9	Negative staining and nanogold-labeling electron microscopy	60
5.10	Immunoblots.....	61
5.11	Growth inhibition assay	61
5.12	Propidium Iodate/Annexin V viability assay	62
5.13	Immunofluorescence microscopy	63
5.14	Protein MW determination with Static Light Scattering (SLS)	63
5.15	Protein secondary structure determination by circular dichroism (CD).....	64
5.16	Thermal shift assay	64
6	Structure of the TbBILBO1-NTD from <i>Trypanosoma brucei</i> reveals an essential requirement for a conserved surface patch	65
6.1	Aim	65
6.2	Targeting of TbBILBO1 to the FPC.....	65
6.3	Overexpression of TbBILBO1-ΔNTD has a dominant negative effect on cell growth.....	66
6.4	The NMR structure of the TbBILBO1-NTD	68
6.5	Crystal structure of the TbBILBO1-NTD	73
6.6	The NTD has a conserved surface patch essential for TbBILBO1 function.....	78
6.7	Impaired TbBILBO1 function is lethal.....	85
6.8	Discussion.....	86

7	Oligomerization and assembly mechanisms of TbBILBO1	89
7.1	Summary	89
7.2	The TbBILBO1-CCD forms an antiparallel homodimer	89
7.3	The TbBILBO1-LZ mediates oligomerization	91
7.4	The TbBILBO1-LZ mediates filament assembly	92
7.5	TbBILBO1 assembles into fibers.....	94
7.6	Discussion.....	96
8	The EF-hand motif, filament junction visualization, and a TbBILBO1 binding partner	100
8.1	Summary	100
8.2	Calcium-binding property of the TbBILBO1-EFh motif.....	100
8.3	Visualization of the filament junction formation	102
8.4	FPC4 is a TbBILBO1 binding partner	104
8.5	Discussion.....	109
9	Conclusions and perspectives.....	111
	References.....	115
	Appendix.....	129
	CURRICULUM VITAE.....	159

Table of Figures

Figure 1 Life cycle of <i>Tripanosoma brucei</i>	22
Figure 2 Schematic diagram of the cell architecture of <i>T. brucei</i> illustrating and its major organelles.....	24
Figure 3 Cross section of <i>T. brucei</i> cell showing the flagellum with its axoneme, paraflagellar rod, and attachment zone.	25
Figure 4 Schematic diagram of FP biogenesis.....	34
Figure 5 Schematic position of the FPC relative to other cytoskeletal components.....	35
Figure 6 TbBILBO1 domain organization and sequence alignment.....	37
Figure 7 Schematic of the protein structure determination process by NMR.....	39
Figure 8 Schematic of NMR spectra of 1 D, 2 D, and 3 D.	40
Figure 9 The magnetization pathways (red arrow) and observed correlation (blue shaded nuclei) of the heteronuclear NMR spectroscopy.	41
Figure 10 Flowchart of protein structure determination by X-ray crystallography.....	47
Figure 11 The TbBILBO1-LZ is necessary but not sufficient for targeting to the FPC.....	66
Figure 12 Essential function of the TbBILBO1-NTD.....	68
Figure 13 NMR spectra of the TbBILBO1-NTD.	69
Figure 14 Backbone chemical shifts of the TbBILBO1-NTD.	70
Figure 15 NMR structure of the TbBILBO1-NTD.	71
Figure 16 The TbBILBO1-NTD has a ubiquitin-like fold.	73
Figure 17 Cloning strategy and SDS-PAGE of purified/crystallized TbBILBO1-NTD.	74
Figure 18 A typical crystal of the TbBILBO1-NTD.....	75
Figure 19 X-ray diffraction image of the TbBILBO1-NTD crystal.....	75
Figure 20 Crystal structure of the TbBILBO1-NTD.	77
Figure 21 A conserved surface patch on the TbBILBO1-NTD.....	79
Figure 22 A conserved surface patch on the TbBILBO1-NTD is essential for the function of the protein <i>in vivo</i>	81
Figure 23 Overexpression of different Ty1-tagged TbBILBO1 constructs <i>in vivo</i>	82
Figure 24 The detached flagellum in overexpressing cells has an associated basal body.....	84

Figure 25 Overexpression of TbBILBO1-NTD deletion or mutation constructs causes cell death.	85
Figure 26 Structural comparison between the TbBILBO1-NTD and Par6 in the Par6-aPKC complex.....	88
Figure 27 The TbBILBO1-CCD forms an antiparallel dimer.	90
Figure 28 Solubility test of TbBILBO1 with an N-terminal 6×His or MBP-10×His.....	91
Figure 29 Analysis of TbBILBO1 oligomerization by size exclusion chromatography.....	92
Figure 30 The TbBILBO1-LZ is essential for oligomerization.....	93
Figure 31 TbBILBO1 linear oligomers further form condensed lateral assemblies.	95
Figure 32 Assembly mechanisms of TbBILBO1 at the FPC.....	99
Figure 33 Calcium-binding property of the TbBILBO1-EFh motifs.....	101
Figure 34 Attempts to structurally characterize the complex formation at the filament junction.....	104
Figure 35 Predicted ligand binding sites on the N-terminal domain of TbBILBO1.....	105
Figure 36 Primary sequence based bioinformatics analyses of <i>T. brucei</i> FPC4.....	106
Figure 37 Formation of a stable complex between the TbBILBO1-NTD and the FPC4-CTD.....	108
Figure 38 Predicted assembly mechanisms of TbBILBO1 at the FPC.....	113

1 Abstract

Trypanosoma brucei is a unicellular parasite transmitted by tsetse flies that causes sleeping sickness in Africa. *T. brucei* has a single flagellum that emerges near the posterior end of the cell. The flagellum is important for the parasite's motility and attachment to the tsetse fly salivary gland epithelium. At the base of the flagellum is a unique organelle termed the flagellar pocket (FP). The FP is the sole site for all endo- and exocytosis and plays crucial roles in the cell's defense against the host immune system. At the neck region of the FP is a cytoskeletal barrier element termed the flagellar pocket collar (FPC). *T. brucei* BILBO1 (TbBILBO1) was the first characterized component of the FPC. This protein is highly conserved among trypanosomatids and essential for both FP biogenesis and the viability of the parasite. Here, I report structural characterizations of the 67-kDa TbBILBO1.

Based on secondary structure predictions, TbBILBO1 consists of a globular N-terminal domain (NTD, residues 1-110), two EF-hand motifs (EFh, residues 183-249), and a central coiled-coil domain (CCD, residues 263-533) followed by a C-terminal leucine zipper (LZ, residues 534-578). My localization analysis in the procyclic form of *T. brucei* showed that the LZ is essential for targeting of TbBILBO1 to the FPC. Overexpression of TbBILBO1-ΔNTD (a construct lacking the NTD), but not the full-length TbBILBO1, was lethal after 4 days of induction. The NMR and X-ray structures of the TbBILBO1-NTD revealed that it adopts a ubiquitin-like fold with a conserved aromatic/basic surface patch that is critical for TbBILBO1 function *in vivo*, implying that it is a potential target for therapeutic drugs. This patch also interacted with the C-terminal domain of FPC4, another newly identified FPC component. I also demonstrated that full-length TbBILBO1 forms a filament-like structure via both the antiparallel arrangement of the central coiled-coil and the LZ-mediated inter-dimer interaction. This structure seems to further assemble into condensed fibers via lateral association between the filaments. Taken together, these data suggest that TbBILBO1 has the properties needed to form a collar structure and the with EFh being potentially essential to control the gating function of the FPC.

2 Zusammenfassung

Trypanosoma brucei ist ein einzelliger Parasit, der von der Tsetse Fliege übertragen wird und die Schlafkrankheit in Afrika verursacht. *T. Brucei* hat ein einzelnes Flagellum, das nahe dem hinteren Ende der Zelle herausragt. Dieses Flagellum ist von Bedeutung für die Beweglichkeit des Parasiten und für seine Anhaftung an das Epithelium der Speicheldrüse der Tsetse Fliege. An der Basis der Geißel befindet sich eine einzigartige Organelle, genannt *Flagellar Pocket* (FP). FP ist der einzige Ort für alle Vorgänge der Endo- und Exozytose und spielt eine entscheidende Rolle in der Verteidigung der Zelle gegen das Immunsystem des Wirts. Am oberen Ansatz der FP befindet sich ein Element der zytoskelettalen Barriere, die sogenannte *Flagellar Pocket Collar* (FPC). *T. brucei* BILBO (TbBILBO1) war die erste charakterisierte Komponente von FPC. Dieses Protein ist in hohem Maße unter Trypanosomatiden konserviert und ist sowohl für die FP Biogenese als auch für die Lebensfähigkeit der Parasiten essentiell. In dieser Studie wird die strukturelle Charakterisation des 67-kDa Proteins TbBILBO1 beschrieben.

Basierend auf der Vorhersage der Sekundärstruktur besteht TbBILBO1 aus einer kugelförmigen N- terminalen Domäne (NTD, aa 1-110), zwei EF-Hand Motiven (EFh, aa 183-249), und einer zentralen coiled-coil Domäne (CCD, aa 263 -533), gefolgt von einem C-terminalen Leucin-Zipper (LZ, aa 534-578). Meine Lokalisierungsanalysen in der prozyklischen Form von *T. brucei* zeigten, dass der LZ von wesentlicher Bedeutung für die genaue Ausrichtung von TbBILBO1 an der FPC ist. Die Überexpression einer TbBILBO1 Mutante, bei der die NTD fehlte (TbBILBO1-ΔNTD), wirkte sich 4 Tage nach der Induktion lethal auf die Zellen aus, nicht dagegen die Überexpression des kompletten Proteins (TbBILBO1-FL). NMR-und Röntgenstrukturanalysen von TbBILBO1 - NTD zeigten, dass es eine Ubiquitin - ähnliche Faltung mit einer konservierten aromatisch/basischen Stelle an der Oberflächen annahm, die kritisch für die TbBILBO1 Funktion *in vivo* war und ein potenzielles Ziel für therapeutische Medikamente darstellt. Diese Stelle interagiert auch mit der C- terminalen Domäne von FPC4, eine weitere, neulich identifizierte Komponente von FPC. Weiters wird beschrieben, dass das komplette TbBILBO1 eine filament ähnliche Struktur sowohl durch die antiparallele

Anordnung der zentrale Coiled-Coil Domain als auch durch die LZ -vermittelte inter - Dimer Interaktion bildete. Diese Struktur wurde dann in verkürzten Fasern über seitliche Assoziation zwischen den Filamenten aufgebaut. Zusammengefasst zeigten meine Daten, dass TbBILB01 die Eigenschaften besitzt, um eine Membran-gebundene manschetten-ähnliche Struktur zu bilden und dass das Auftreten von EFh wesentlich für die Steuerung der Gating-Funktion des FPC ist.

3 Introduction

3.1 Sleeping sickness

Sleeping sickness (human African trypanosomiasis) is a disease caused by the unicellular unflagellated parasite *Trypanosoma brucei*. Sleeping sickness is only found in sub-Saharan Africa in the region between 14°N and 20°S. The presence of this disease is dependent on the distribution of its insect vector, tsetse flies of the genus *Glossina* (Malvy and Chappuis 2011). This genus consists of 30 species and subspecies. Based on their habitats, the flies are separated into three different groups - *fusca* group species that are mainly forest-dwelling, *palpalis* group species that inhabit forests and riverine-forest, and *morsitans* group species that inhabit woodland savannah where, both human and domesticated animals live (Rogers, Hendrickx et al. 1994).

Sleeping sickness is fatal if left untreated. Major outbreaks in the 19th century caused the death of approximately 800,000 people (Louis and Simarro 2005). Thanks to effective control mechanisms, by early 1960, the disease was almost exterminated. However, due to a lack of surveillance and control activities, it re-emerged again in the 1970s by infecting about 300,000 people in the Democratic Republic of the Congo (DRC), Angola, southern Sudan, Central African Republic, and Uganda (Smith, Pepin et al. 1998). From 1999, control activities were increased again and resulted in a drop of the reported cases to below 10,000 as of 2009 (Simarro, Diarra et al. 2011).

There are two forms of sleeping sickness based on epidemiology and geographical range - the disease in central and west Africa, which is caused by the subspecies *T. brucei gambiense*, and the disease in east and southern Africa, which is caused by *T. brucei rhodesiense* (Brun, Blum et al. 2010). *T. brucei gambiense* is transmitted by tsetse flies of the *Glossina palpalis* group, while *T. brucei rhodesiense* is transmitted by tsetse flies of the *Glossina morsitans* group (Malvy and Chappuis 2011). *T. brucei gambiense* causes 97% of human cases whereas *T. brucei rhodesiense* causes approximately 3% of the human cases (Brun, Blum et al. 2010).

After infection, the disease progresses in two distinct stages. The first stage is the haemolymphatic stage. At this stage, the trypanosomes propagation is restricted to the blood and the lymphatic system. The second stage is the meningo-encephalitic stage. At this stage, trypanosomes actively invade the central nervous system, causing circadian disruption and neuropsychiatric disorders which lead to coma and death if left untreated. The infection caused by *T. brucei gambiense* is chronic and is fatal within about 3 years, whereas the infection caused by *T. brucei rhodesiense*, is lethal within several months if left untreated (Checchi, Filipe et al. 2008).

Currently, no vaccine is available to treat the sleeping sickness due to the ability of the parasite to evade the immune response of the host (Absalon, Blisnick et al. 2008). To date, the disease is treated only with suramin, pentamidine, elfornithine, and the toxic organo-arsenical melarsoprol (Burri 2010). These drugs are unsatisfactory because of their cost, toxicity, difficulty of delivery, long treatment, and low efficacy. The treatment is determined primarily by the stage of the disease and the causative pathogen.

For sleeping sickness caused by *T. brucei gambiense*, first-stage patients are treated with pentamidine by intramuscular injection. It often gives adverse effects such as pain at the injection site, hypoglycaemia, and hypotension. Second-stage patients are treated by melarsoprol, which is an arsenic derivative - therefore it frequently has very high adverse effects, including an encephalopathic syndrome which often kills the patient (Burri 2010). The other adverse effects are peripheral neuropathy, skin rash, hepatic toxicity, acute phlebitis, and vein sclerosis (Malvy and Chappuis 2011). An effort to find drug replacement has resulted in the finding of elfornithine (α -difluoromethylornithine, DFMO). Elfornithine has the capability to irreversibly inhibit the enzyme activity of ornithine decarboxylase (ODC), one of the essential enzymes in the polyamine biosynthetic pathway (Metcalf, Bey et al. 1978). A comparative study between melarsoprol and elfornithine shows that elfornithine could reduce mortality and cumulative incidence better than melarsoprol (Chappuis, Udayraj et al. 2005).

The treatment of sleeping sickness caused by *T. brucei rhodesiense* is also divided into two stages. Suramin is the drug used for the first-stage infection with adverse effects such as peripheral neuropathy, nephrotoxicity, and bone marrow toxicity. For the second stage of infection, melarsoprol is the only drug available due to the natural

resistance of the *T. brucei rhodesiense* to eflornithine. This resistance is because the ODC activity in *T. brucei rhodesiense* has higher specific activity and faster enzyme turnover compared to the ODC activity in *T. brucei gambiense* (Iten, Mett et al. 1997).

Efforts to find new medicines to fight sleep sickness still continue. One example is using combination of drugs to prevent the development of resistance, such as the use of nifurtimox-eflornithine combination therapy (NECT) in the treatment of *T. brucei gambiense* infection (Priotto, Kasparian et al. 2009). Fenidazole and its derivatives are the other drug candidates for the disease. *In vivo* studies in mice suggest effectiveness at killing both *T. brucei gambiense* and *T. brucei rhodesiense* (Kaiser, Bray et al. 2011). An orally active benzoxaborole (SCYX-7158) is another drug candidate for treatment of both stages of the disease caused by both *T. brucei gambiense* and *T. brucei rhodesiense* (Jacobs, Nare et al. 2011).

3.2 *Trypanosoma brucei*

3.2.1 Life cycle of *T. brucei*

T. brucei has several developmental forms during its life cycle in both mammalian and insect hosts (Figure 1) (Fenn and Matthews 2007). When an infected tsetse fly bites human skin, metacyclic trypomastigotes are transmitted to the skin and then to the bloodstream from the salivary glands of the fly. In the body fluid, such as blood or lymphatic/spinal fluid, the trypomastigotes transform into the bloodstream form (BSF) trypomastigotes and multiply by binary fission. In the bloodstream, as the population increases, the “long slender” proliferating cells differentiate into cell cycle-arrested cells called the “short stumpy” form due to the action of a parasite-derived factor, stumpy induction factor (SIF) (Vassella, Reuner et al. 1997).

SIF activity, which operates through the cAMP signaling pathway, triggers cell cycle arrest in G1/G0 phase and induces differentiation with high efficiency and rapid kinetics (Shapiro, Naessens et al. 1984; Vassella, Reuner et al. 1997). Several protein families of SIF have been discovered. They include a PX-FVYVE family zinc finger kinase (ZFK) and a MAP kinase family member (TbMAPK5). Genetic depletion of both of these proteins in

pleomorphic lines resulted in a developmental acceleration to the stumpy form and reduced growth in culture and in mice (Vassella, Kramer et al. 2001; Domenicali Pfister, Burkard et al. 2006). The stumpy form is the pre-adapted form of BSF *T. brucei* for transmission to the tsetse fly. The protein that induces cell cycle arrest in the stumpy form is tyrosine phosphatase (TbPTP1) (Szoor, Wilson et al. 2006). The ablation of this protein by RNAi induced spontaneous differentiation to the PCF.

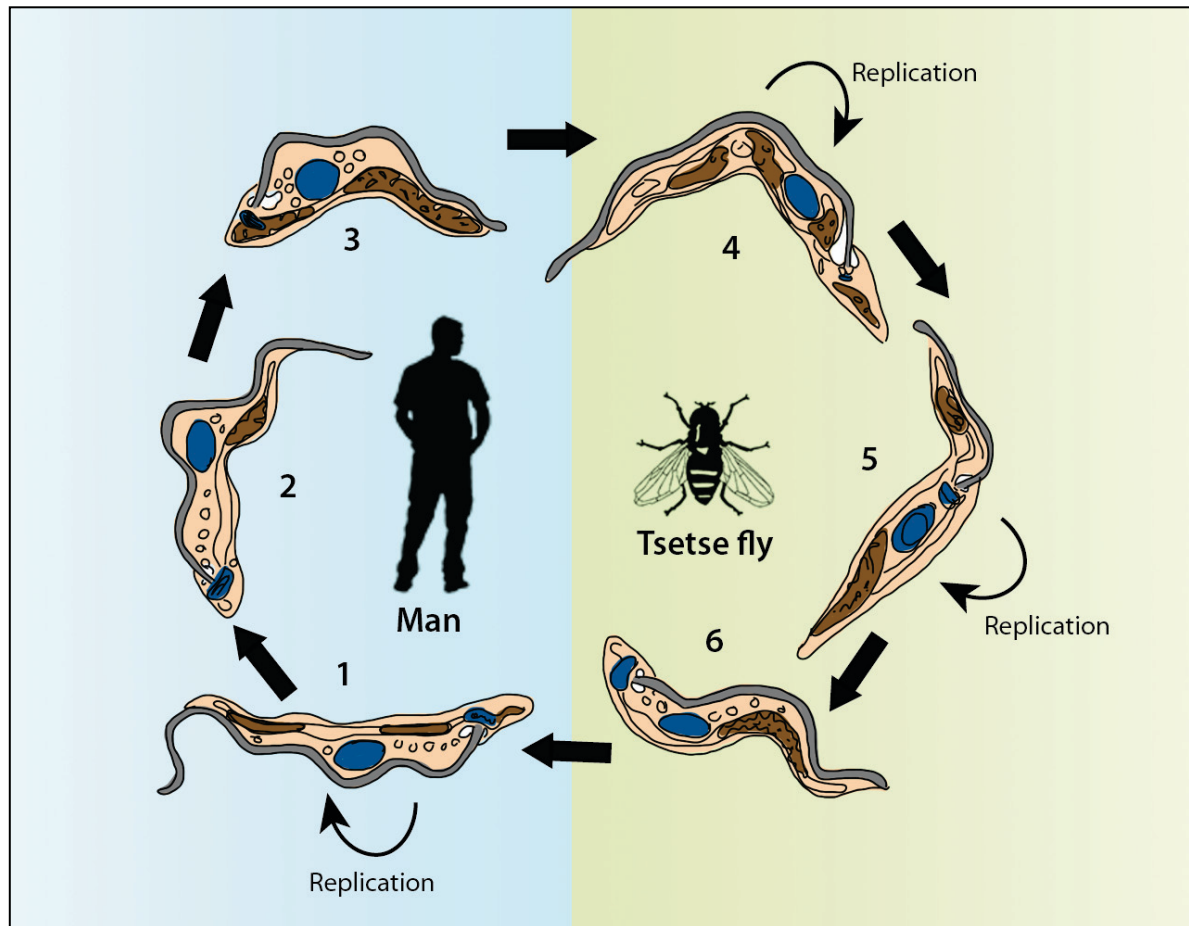


Figure 1 Life cycle of *Tripanosoma brucei*.

The BSF has a slender form (1) which can replicate (curved arrow). It transforms into the intermediate form (2), and then into the stumpy form (3). In the tsetse fly, the BSF transforms into the dividing PCF (4) in the midgut, then to the epimastigote form (5). During blood sucking by tsetse fly, this form migrates to the salivary gland and becomes the infective metacyclic form (6). Figure is reproduced from (Brun, Blum et al. 2010).

When an infected human is bitten by another tsetse fly, the BSF trypomastigotes are transferred to the fly's midgut and transform into the PSF. In the transition process, the parasite undergoes pre-adaptation processes such as growth arrest, cellular architecture remodeling, activating cytochrome-mediated metabolism in the mitochondrion, and major changes in gene expression (Field and Carrington 2009). This

transformation and differentiation can be triggered by a temperature drop, exposure to citrate/*cis*-aconitate, or exposure to environmentally reduced pH (Czichos, Nonnengaesser et al. 1986; Overath, Czichos et al. 1986; Rolin, Hancocq-Quertier et al. 1998; Sbicego, Vassella et al. 1999). In the midgut, the PSF can multiply by binary fission. When it migrates to the salivary glands, the PSF undergoes an asymmetric cell division generating a long and a short epimastigote form (Van Den Abbeele, Claes et al. 1999). The short form is destined for attachment to the salivary gland and proliferation by sexual exchange (Gibson, Peacock et al. 2006). The epimastigote transforms further and matures into metacyclic trypomastigotes. The complete differentiation steps in a tsetse fly take place over three to five weeks.

3.2.2 The cellular architecture of *T. brucei*

The cell body of *T. brucei* has an elongated shape (15 to 40 µm long) and is tapered at both anterior and posterior ends. The shape of the cells is maintained by their cytoskeleton that consists of a corset of subpellicular microtubules present in all cell cycle stages (Sherwin and Gull 1989). These microtubules (diameter of 24 nm) are helically arranged along the axis of the cell with regular spacing (18-22 nm) and variable length (Sherwin and Gull 1989).

T. brucei has a single flagellum that emerges near the posterior end of the cell (Figure 2). The flagellum is important for the parasite's motility and attachment to the tsetse fly salivary gland epithelium (Tetley and Vickerman 1985). It has a canonical axoneme (Figure 3) with nine outer doublet microtubules surrounding a central pair. The outer doublet consist of a complete A-tubule with 13 α/β -tubulin protofilaments and an incomplete B-tubule with 10 protofilaments and one additional filament (Ralston, Kabututu et al. 2009). The central pair of microtubules is nucleated from the basal body and continues until the end of the flagellum. Projecting from each outer A-tubule doublet are outer and inner arm dyneins which provide the force for motility. Dynein is a complex molecular motor consisting of at least 13 different components (King 2003). It usually consists of one to three catalytic heavy chains, some associated light chains, intermediate chains, and light-intermediate chains (King 2003). In addition, the radial spokes project from each outer doublet to the central pair (Ralston and Hill 2008).

Together with the central pair, radial spokes are essential as mechano-chemical sensors to control motility in 9+2 cilia and flagella (Smith and Yang 2004).

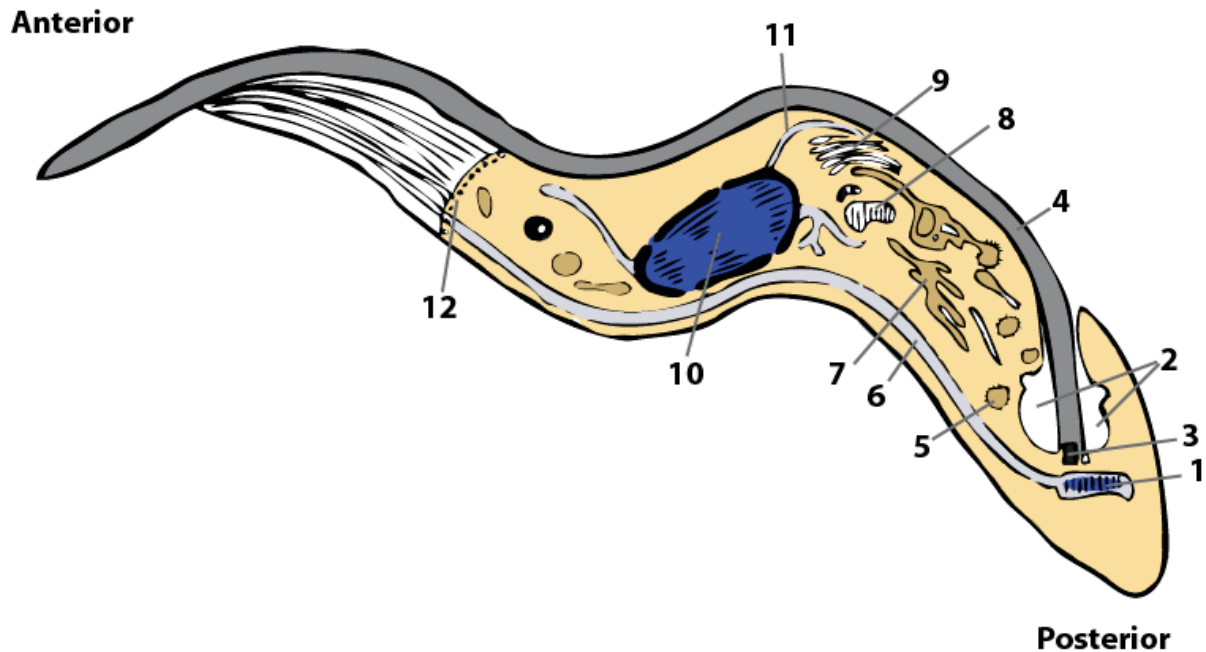


Figure 2 Schematic diagram of the cell architecture of *T. brucei* illustrating its major organelles.

1. Kinetoplast, 2. Flagellar pocket, 3. Basal body, 4. Flagellum, 5. Vesicle, 6. Mitochondrion, 7. Endosomes, 8. Lysosome, 9. Golgi apparatus, 10. Nucleus, 11. Endoplasmic reticulum (ER), 12. Pellicular microtubules.

Alongside the axoneme, a peculiar structural feature termed as paraflagellar rod (PFR) is present (Figure 3). It is formed of paracrystalline filaments attached to one face of the axoneme and is present once the flagellum has exited the flagellar pocket neck (Cachon, Cachon et al. 1988). Based on its structural morphology and position relative to the axoneme, the PFR is classified into three distinct regions - proximal, intermediate, and distal (Maga and LeBowitz 1999). The proximal and distal regions each contain filaments of 7-10 nm, which intersect at an angle of 100°. The proximal region is connected to the axonemal doublets of the flagellum. The intermediate region consists of 5 nm thin filaments that intersect at an angle of 45° and connect the proximal with the distal regions (Maga and LeBowitz 1999). Several proteins have been characterized as the building block of PFR, namely PFR1, PFR2, and two of PFR-associate adenylate kinase; ADK-A and ADK-B (Russell, Newsam et al. 1983; Ginger, Ngazoa et al. 2005). TbrPDEB1 and TbrPDEB2 are the other known PFR-associated, which have cAMP phosphodiesterase activity involved in nucleotide metabolism (Oberholzer, Marti et al. 2007).

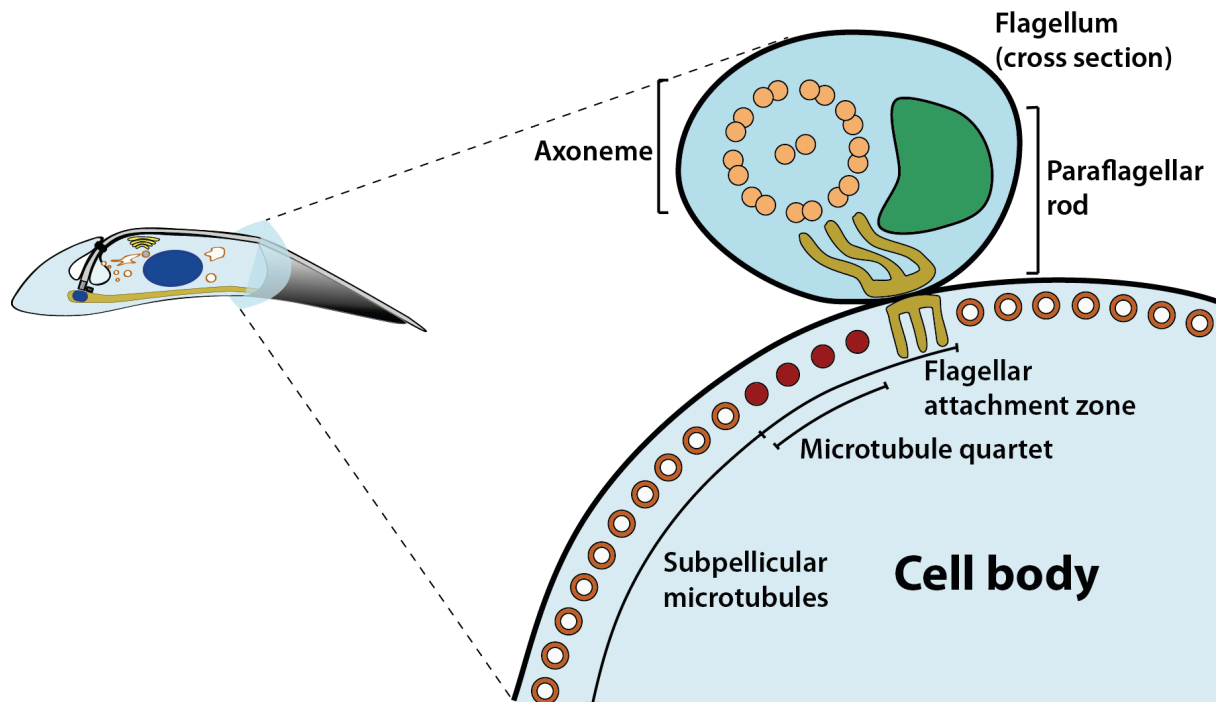


Figure 3 Cross section of *T. brucei* cell showing the flagellum with its axoneme (gold circles), paraflagellar rod (dark green), and attachment zone (yellowish green).

In the cell body, the distribution of subpellicular microtubule (brown ring) and microtubule quartet (brown circle) are also shown. Flagellar attachment zone is located in both flagellum and cell body. The picture is reproduced from (Field and Carrington 2009).

The flagellum is attached to the cell body via a cytoskeletal network and membranous connection called the flagellum attachment zone (FAZ) (Figure 3) (Ralston, Kabututu et al. 2009). The FAZ comprises an electron-dense cytoplasmic filament and a specialized microtubule quartet (MtQ) associated with the smooth ER (LaCount, Barrett et al. 2002). FAZ1, a low-complexity protein containing 14-residue repeats, was the first FAZ filament protein to be identified (Vaughan, Kohl et al. 2008). The ablation of this protein by RNAi produces aberrant FAZ assembly and cytokinesis defects that lead to unequal nuclear segregation and production of non-nucleated daughter cells (Vaughan, Kohl et al. 2008). Zhou *et al* identified another FAZ component, namely CC2D, which consist of coiled-coil motifs and a C-terminal C2 domain (Zhou, Liu et al. 2011). CC2D is present on the FAZ filament, FAZ-juxtaposed ER membrane and basal body. CC2D depletion by RNAi inhibits the assembly of the new FAZ filament, perturbs subpellicular microtubule organization, and generates short daughter cells. Additionally, there are three known membrane proteins that are important for flagellum attachment: flagellum adhesion glycoprotein1 (Fla1), FS179, and Fla3 (LaCount, Bruse et al. 2000; Oberholzer, Langousis et al. 2011; Woods, Nic a'Bhaird et al. 2013). Fla1 is essential for flagellum

attachment in both PCF and BSF of *T. brucei*. FS179 is a putative calcium channel that is important for maintaining Ca^{2+} homeostasis at the flagellum-cell body interface (Oberholzer, Langousis et al. 2011). Fla3 is an essential *T. brucei* bloodstream-stage specific protein for flagellar attachment (Woods, Nic a'Bhaird et al. 2013). Depletion of Fla3 by RNAi disrupts flagellar attachment and results in FAZ1 mislocalization to the posterior end of the cell.

The flagellum is nucleated from the basal body, a microtubule-organizing center (MTOC) for the flagellar axonemal microtubules (Figure 2)(Gull 2003). The basal body is a barrel-shaped structure consisting of nine triplet microtubules analogous to the centriole (Ralston, Kabututu et al. 2009). A probasal body lies orthogonal to the basal body. Several proteins have been identified that localize to the basal body, such as γ -tubulin, centrin, TbLRRP (the polycystic kidney disease protein, *seahorse*), and TbNRKC (the NIMA-related kinase) (Dilbeck, Berberof et al. 1999; McKean, Baines et al. 2003; Morgan, Denny et al. 2005; Pradel, Bonhivers et al. 2006). The basal body is essential for the segregation of kinetoplast during cell division (Robinson and Gull 1991; Ralston, Kabututu et al. 2009).

The kinetoplast is the mitochondrial genome and contains thousands of molecules of topologically interlocked circular DNA (Robinson and Gull 1991). It is located orthogonally next to the basal body (Figure 2). It consists of maxicircles and minicircles. Maxicircles encode mitochondrial proteins and ribosomal RNA, whereas minicircles encode guide RNA molecules that are essential for editing maxicircles mRNA transcripts (Shapiro and Englund 1995). The kinetoplast is replicated early in the cell cycle and segregates during the moving apart of the basal bodies before mitosis (Klingbeil, Drew et al. 2001). Cells treated with 2 μM of the microtubule depolymerizing drug ansamitocin, which prevents separation of the basal bodies, also prevents kinetoplast segregation in dividing cells (Robinson and Gull 1991).

The tight association between basal body and kinetoplast is mediated by a filamentous network that extends from the proximal side of the basal body to the kinetoplast DNA (kDNA) (Ogbadoyi, Robinson et al. 2003). This connector is termed the tripartite attachment complex (TAC). The TAC is present throughout kDNA duplication and mediates kDNA network segregation, pulling the new networks into the daughter cells

by their linkage to the basal body (Ogbadoyi, Robinson et al. 2003). p166 is the first identified molecular component of the TAC (Zhao, Lindsay et al. 2008). It localizes in between of the kDNA disk and the flagellar basal body. p166 knockdown by RNAi caused shrinking or lost of kDNA, which indicates an important role in kDNA segregation.

In the region of the proximal end of the flagellum, the flagellar pocket (FP) is present. The FP is an invagination of the plasma membrane that surrounds the base of the flagellum from where the flagellum emerges from the cell. The FP is an essential organelle and is the only site for endo-/exocytotic activity (Overath and Engstler 2004). Further discussion about this organelle will be presented in the next section (3.3 Flagellar pocket).

Beginning at the basal body, a set of four specialized microtubules termed the MtQ wrap around the FP and then run alongside the FAZ filament to the cell's anterior tip. The MtQ is positioned on the same side as doublets 6 - 9 of the axoneme and closely associated with a segment of the ER which interdigitates between the individual microtubules. The MtQ can be recognized using the monoclonal antibody 1B41 that identifies a specific β -tubulin isoform. Immunofluorescence analysis showed that the antibody only stains the MtQ with no signal on any other microtubules (Gallo, Précigout et al. 1988).

Close to the FP are several canonical eukaryotic endomembrane organelles, such as the ER, Golgi, endosomes, and lysosomes. The ER is a highly branched tubular network extending throughout the cell but excluded from the flagellum (Bangs, Uyetake et al. 1993). The ER is contiguous with the nuclear envelope and a connected system of cisternal or tubular membranes that are frequently closely connected with the plasma membrane. This organelle is responsible for initial assembly of cell surface proteins or lysosomes and for synthesis of membrane phospho- and glycolipids (McConville, Mullin et al. 2002).

The proteins and lipids that are newly synthesized and assembled in the ER are collected at an ER exit site and sent to the Golgi for processing in an ordered manner by glycosidases and glycosyltransferases. Based on electron tomography analysis, the Golgi of *T. brucei* is located near the FP (Lacomble, Vaughan et al. 2009). The single Golgi apparatus comprises a stack of *cis*-Golgi network, *medial* cisternae, and *trans*-Golgi network with a total surface area of about 2 μm^2 (Yelinek, He et al. 2009). After the

newly processed proteins and lipids reach the *trans*-Golgi network, they are sorted and delivered to various destinations.

The lysosomes are lytic vacuoles that receive material from the Golgi via endosome intermediates. Their morphology varies in different trypanosome stages; the mature lysosomes consist of a series of prominent spherical vacuoles that have a perinuclear distribution. This morphological variation reflects the changing requirements for lysosomal degradation in regulating protein turnover and nutrients acquisition during the parasite life cycle (McConville, Mullin et al. 2002). p67 is a lysosome-associated membrane protein (LAMP)-like type I transmembrane lysosomal glycoprotein. This protein has a short cytoplasmic domain consisting of a classical dileucine sequence that is embedded in the acidic region required for normal lysosomal morphology. p67 ablation in BSF *T. brucei* by RNAi results in a dramatic effect on lysosomal morphology with the internal membrane profiles similar with the autophagic vacuoles. This suggests that p67 plays an important role in maintaining the normal structure and physiology of the lysosome (Peck, Shiflett et al. 2008).

Proteome analysis of the membrane composition of BSF *T. brucei* showed that the plasma membrane contains a large amount of integral membrane proteins, such as ion pumps and channels, nucleoside/nucleobase transporters, and adenylate cyclases (Bridges, Pitt et al. 2008). The plasma membrane is attached to the dense corset of stable and cross-linked subpellicular microtubules. The protein composition of the plasma membrane is dominated by a single glycoprotein isoform named variant surface glycoproteins (VSGs), which are essential for parasite protection against host immune responses. In BSF cells, the surface of *T. brucei* is densely covered by a VSG monolayer with $\sim 5 \times 10^6$ VSG dimers per cell (Cross 1975). This amount comprises around 10% of its total cellular proteins (Mayor and Riezman 2004; Overath and Engstler 2004). One molecule of VSG consists of an elongated NTD, a GPI anchor that contains a dimyristoyl-glycerol moiety, and a CTD (Cross 1996). Other surface proteins include invariant surface glycoprotein 65 (ISG65), ISG75, and AT1 (Cross 1975; Ziegelbauer and Overath 1993; Field and Carrington 2009).

3.3 Flagellar pocket

As mentioned earlier, the FP is an invagination of the plasma membrane that surrounds the base of the flagellum from where the flagellum emerges from the cell. The FP is present in all trypanosomatids although the morphology is different in each organism. In *T. brucei*, the FP is located near the posterior end of the cell. The flagellum enters the FP asymmetrically, producing a bulge structure on one side close to where the probasal body and Golgi complex are located (Lacomble, Vaughan et al. 2009). There are two boundaries defining the FP. These boundaries differentiate the FP membrane from the plasma membrane and from the flagellar membrane that surrounding the flagellum. The first boundary is the area surrounding the transition zone of the flagellum. This defines the flagellum entry at the base of the pocket. The second boundary is the area where the flagellum emerges to the cell exterior at the top of the pocket that is characterized by an electron-dense cytoskeletal barrier element termed the flagellar pocket collar (FPC) and the neck region (a vase-shaped area between the FPC and the flagellum exit site from the cell body) (Lacomble, Vaughan et al. 2009).

Even though these three membranes (FP, flagellum membrane, FP neck) are all contiguous subdomains of the plasma membrane, they have different biological functions. Compared to the plasma membrane, the FP membrane has a different protein composition. It has several polypeptides, which are found only at this structure, such as transferrin receptor, SRA, LDL receptor, HPHBR, and CRAM (Kabiri and Steverding 2000; Pal, Hall et al. 2002; Vanhamme, Paturiaux-Hanocq et al. 2003; Mussmann, Engstler et al. 2004; Qiao, Chuang et al. 2006; Vanhollebeke, De Muylder et al. 2008). The transferrin receptor is important for *T. brucei* to provide iron by acquiring host transferrin from the bloodstream. This receptor consists of one GPI membrane anchor and eight N-glycosylation sites (Mehlert, Wormald et al. 2012). These receptor subunits consist of the endoglycosydase H-sensitive and the endoglycosidase H-resistant N-glycans that contain oligomannose and paucimannose. Different from the FP membrane, the flagellum membrane of *T. brucei* has several membrane proteins with a broad range of molecular functions (such as signaling), and many that are upregulated in the mammalian-infectious stage of the parasite life cycle (Oberholzer, Langousis et al. 2011). Some proteins characterized as being present on the flagellum surface are required for

VSG clearance and antigenetic variation (VSG, MSP-A, and GPI-specific phospholipase C), for host nutrient uptake (transferring receptors and glucose transporter), and for host-parasite signaling (adenylate cyclases and calflagins).

An analogous structure to the FP appears to be present in mammalian cells, known as the ciliary pocket. Sorokin reported that the cells from fibroblasts and smooth muscle of chicken duodenum show this pocket at the base of their primary cilia (Sorokin 1962). Furthermore, the ciliary pocket is also observed in *Xenopus* rod photoreceptor at the base of the connecting cilium, in mouse 3T3 cells, in human retinal pigment epithelial cells, in murine embryonic fibroblast, and in the primary cilium of the mouse kidney epithelial (IMCD3) cells (Papermaster, Schneider et al. 1985; Molla-Herman, Boularan et al. 2008; Molla-Herman, Ghossoub et al. 2010; Rohatgi and Snell 2010).

3.3.1 The function of flagellar pocket

In *T. brucei*, the FP is the only site for all endo-/exocytotic activities. All endomembrane components, such as the Golgi complex, some part of ER, lysosome and endosomes, are coordinately distributed facing the FP. In eukaryotes, endocytosis of cell surface components can occur by a mechanism involving the coat protein clathrin requirement or not (Nichols and Lippincott-Schwartz 2001). Clathrin can form a triskelion shape consist of three clathrin heavy chain (MW=190 kDa) and three clathrin light chain (MW=25-29 kDa) (Edeling, Smith et al. 2006). Clathrin can spontaneously form a cage-like structure. In the presence of adaptor proteins, it can assemble into coats. In yeast, clathrin is not essential for endocytosis and no major alterations are observed in the cells lacking functional clathrin (Nichols and Lippincott-Schwartz 2001). In mammalian cells, the endocytosis of interleukin 2 (IL2) receptors proceeds normally even when clathrin function is disrupted (Lamaze, Dujancourt et al. 2001). This clathrin-independent endocytosis needs dynamin for its process and is regulated by Rho family GTPase (Lamaze, Dujancourt et al. 2001). Some clathrin-independent mechanisms of endocytosis in eukaryotes are Arf6-dependent, flotillin-dependent, and macropinocytosis pathways (Doherty and McMahon 2009).

Unlike the higher eukaryotic organisms that have several different endocytosis mechanisms, endocytosis activity in trypanosome depends solely on clathrin due to a lack of clathrin-independent pathways (Grunfelder, Engstler et al. 2003). Clathrin-coated pits and vesicles are abundant in the area close to the FP (Grunfelder, Engstler et al. 2003). TbCLH is the clathrin heavy chain protein in *T. brucei* and is present in both endocytotic vesicles and post-Golgi elements. Depletion of TbCLH expression by RNAi results in the rapid lethality of the BSF with a massive enlargement of FP. This suggests that depletion of TbCLH does not affect membrane delivery, but its removal is blocked (Allen, Goulding et al. 2003). Similar results are seen in the PCF. Depletion of TbCLH by RNAi results in the inhibition of the export of the FP-associated transmembrane receptor CRAM from the ER to the FP. However, the trafficking of the GPI-anchored procyclin coat is not significantly affected (Hung, Qiao et al. 2004).

Besides the requirement of clathrin, endocytosis and exocytosis also depend on Rab proteins. Rab proteins are small GTPases that are essential for eukaryotic intracellular transport including the tethering of vesicles to the membrane targets, vesicle interaction with cytoskeletal elements, and probably vesicle budding (Zerial and McBride 2001). These proteins are found in all eukaryotes and their number increases according to the complexity of the organism (Ackers, Dhir et al. 2005). The structural features that provide specificity functions to these proteins are the conserved NTD, which has GTPase activity, and a non-conserved CTD, which is believed to be essential for binding of different effectors proteins that mediate the specific activities of each Rab (Gonzalez Jr and Scheller 1999). In the trypanosome genome, there are sixteen Rab and Rab-related proteins encoded, which mediate the specificity of vesicle fusion and cytoskeletal and coat protein interactions (Ackers, Dhir et al. 2005). Eight of them, namely Rab1A, 1B, 2, 4, 5A, 6, 7, and 11 have orthologues/homologues in higher eukaryotes. Rab1 and Rab2 are important for ER and Golgi transport, Rab5 for trafficking through the early endosome, Rab4 and Rab11 for recycling, Rab7 for delivery to the late endosome/lysosome, and Rab6 for retrograde transport through the Golgi complex (Ackers, Dhir et al. 2005). In the PCF, Rab11 is localized on a compartment near the basal body. However, in the BSF, Rab11 is localized on the endomembranes anterior to the FP near collecting tubules, similar to the Rab5A localization site (Jeffries, Morgan et al. 2001).

The rapid endocytosis/exocytosis activity in trypanosome is essential for periodically switching its major GPI-anchored VSG, which is important for the parasite to evade the immune response of the host (O'Beirne, Lowry et al. 1998). If *T. brucei* had only one VSG variant, it would rapidly be killed by a VSG-specific antibody-dependent complement cytotoxicity. However, due to the high number of VSG variants and frequent switching of VSG expression, *T. brucei* can survive by generating distinct antigenic variants that cannot be recognized by the host's immune response. The high number of VSG molecules makes their diffusion in the coat relatively slow due to the steric hindrance caused by dense packing (Overath and Engstler 2004). *T. brucei* encodes different VSG isoforms that are located at the subtelomeric chromosome of all genome classes (Melville, Leech et al. 1998). The sequence diversity of VSG, with only 15-20% primary sequence identity shared by different VSG isoforms, is the reason why *T. brucei* has antigenic variation.

VSG-specific immunoglobulins are removed from the cell surface by a special mechanism. At low temperatures, VSG-specific immunoglobulins are observed to be uniformly distributed over the cell surface. However, cell incubation at 37 °C results in the internalization of immunoglobulins at the FP therefore reducing the antibody-dependent efficacy of killing (Barry 1979). In the FP, VSG-bound immunoglobulins are segregated from unbound-VSGs, endocytosed by Rab5A containing vesicles, and degraded to small peptides (Pal, Hall et al. 2003). Meanwhile, the unbound-VSGs are recycled separately.

The FP is also involved in signaling pathways. Phosphoinositide 3-kinase (PI3K) and target of rapamycin (TOR) signaling pathways interact with the FP. Vps34 is a class III PI3K that mediates phosphorylation of PI to PI3P. In yeast, Vps34 regulates transport to the vacuole, whereas in humans, Vps34 is required for multivesicular body morphogenesis and for lysosomal protein transport (Herman and Emr 1990; Brown, DeWald et al. 1995; Fernandez-Borja, Wubbolts et al. 1999). Vps34 is the component that is essential for endocytosis in *T. brucei*. Its knock-down causes FP morphological abnormality and an accumulation of membrane-bound paracrystalline inclusions containing flagellar and PFR proteins. Its knock down also causes inhibition of both VSG export and the Golgi complex segregation (Hall, Gabernet-Castello et al. 2006).

TOR kinases are essential for controlling cell growth through the action of the TORC1 and TORC2 complexes (Field and Carrington 2009). These proteins are conserved in trypanosomes. TORC1 controls temporal cell growth and is rapamycin sensitive. In contrast, TORC2 regulates spatial cell growth and is rapamycin resistant. In trypanosomes, however, TORC2 is the rapamycin target and its depletion interferes with actin localization and endocytosis activity. Exposing trypanosomes to rapamycin causes an inhibition in cell growth and an enlargement of the FP (Barquilla, Crespo et al. 2008).

3.3.2 Flagellar pocket biogenesis

FP biogenesis is closely associated with basal body duplication in the initial stages of cell division (Figure 4) (Lacomble, Vaughan et al. 2010). At the beginning of the cell cycle, the probasal body is positioned anterior to the basal body of the existing (old) flagellum. At the transition of G1-S, a new MtQ is nucleated anterior to the old MtQ in the region of the old probasal body. Afterwards, the probasal body matures and elongates to form a transitional zone and new axoneme. Once the axoneme has extended ~240 nm from the basal body, its tip connects to the old flagellum via the flagellar connector, a mobile transmembrane complex which guides the position of the new flagellum along the cell body. Thereafter, the new probasal bodies are formed and a new FPC starts to form while the axoneme continues to elongate. At this stage, the kinetoplast is elongated. The new flagellum, which is positioned anterior to the old flagellum, continues grows in the existing FP in the bulge side. The new basal body then undergoes an anti-clockwise rotation around the old flagellum. This makes the position of the new basal body posterior to the old one. This rotation is also associated with the division of the FP (Lacomble, Vaughan et al. 2010). During the rotation, the new collar is formed on the nascent pocket. Further separation of the basal bodies segregates the FP into two distinct entities, with a single flagellum in each of them. Basal bodies separation also segregates the replicated kDNA (Ogbadoyi, Robinson et al. 2003). Finally, the process is completed by karyokinesis and cytokinesis.

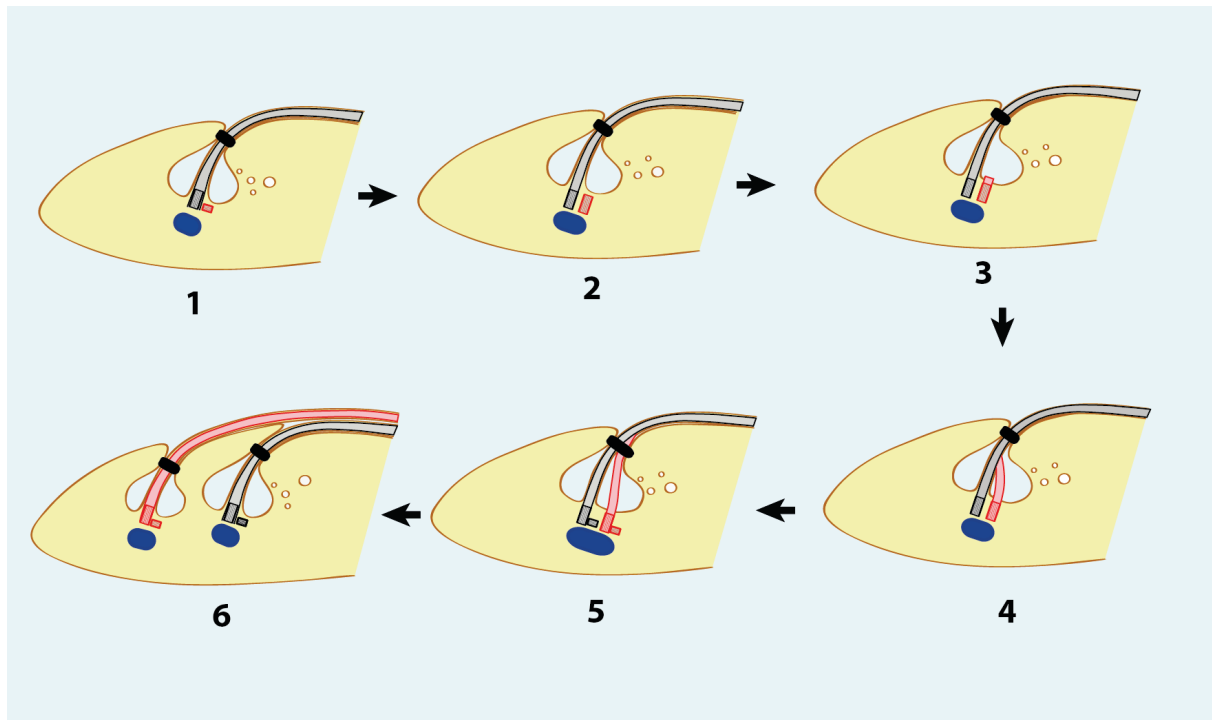


Figure 4 Schematic diagram of FP biogenesis.

1. Normal single cell, 2. probasal body matures, 3. Probasal body elongates to form a transitional zone and new axoneme, 4. The tip of new axoneme connects to the old flagellum via flagellar connector, 5. The new probasal bodies form, the new collar starts to emerge and the axoneme continues to elongate. At this stage, the kinetoplast is elongated, 6. The new basal body undergoes an anti-clockwise rotation around the old flagellum, which positions the new basal body posterior to the old one. This rotation is also associated with the division of the FP (Lacomble, Vaughan et al. 2010).

3.4 Flagellar pocket collar

At the neck region of the FP is an electron-dense cytoskeletal structure called the flagellar pocket collar (FPC), which has a diameter slightly larger than the flagellum (Figure 5)(Lacomble, Vaughan et al. 2009). The collar presumably serves to anchor the FP membrane to the flagellum membrane, and provides a positioning mechanism for the flagellum in the cytoskeletal arrangement (Field and Carrington 2009). It is believed that the collar does not completely encircle the flagellum. Since the MtQ is always tightly attached to the inner face of the pocket membrane, it suggests that the collar is locally dislocated in this region (Lacomble, Vaughan et al. 2009). Above the FPC, the bilobe (which forms a "fishhook" structure) can be observed (Figure 5) (Morriswood, He et al. 2009; Esson, Morriswood et al. 2012). The bilobe is a cytoskeletal structure positioned above the FPC, presumably in the FP neck. TbMORN1 was the first protein characterized

that is exclusively localized in this area (Morriswood, He et al. 2009). Currently, using the novel proximity-dependent biotinylation identification (BioID) technique, seven new bilobe constituents were identified (Morriswood, Havlicek et al. 2013). The bilobe is intriguing since electron microscopy (EM) studies and tomographic reconstructions of the FP region did not observe it (Gadelha, Rothery et al. 2009; Lacomble, Vaughan et al. 2009; Lacomble, Vaughan et al. 2010). Adjacent to the bilobe, TbCentrin4 is present. Besides that, this protein also localizes to the basal body (Shi, Franklin et al. 2008; Esson, Morriswood et al. 2012). Together with TbMORN1, TbCentrin4 forms a hairpin-like structure with both arms flanking the MtQ and the FAZ filament.

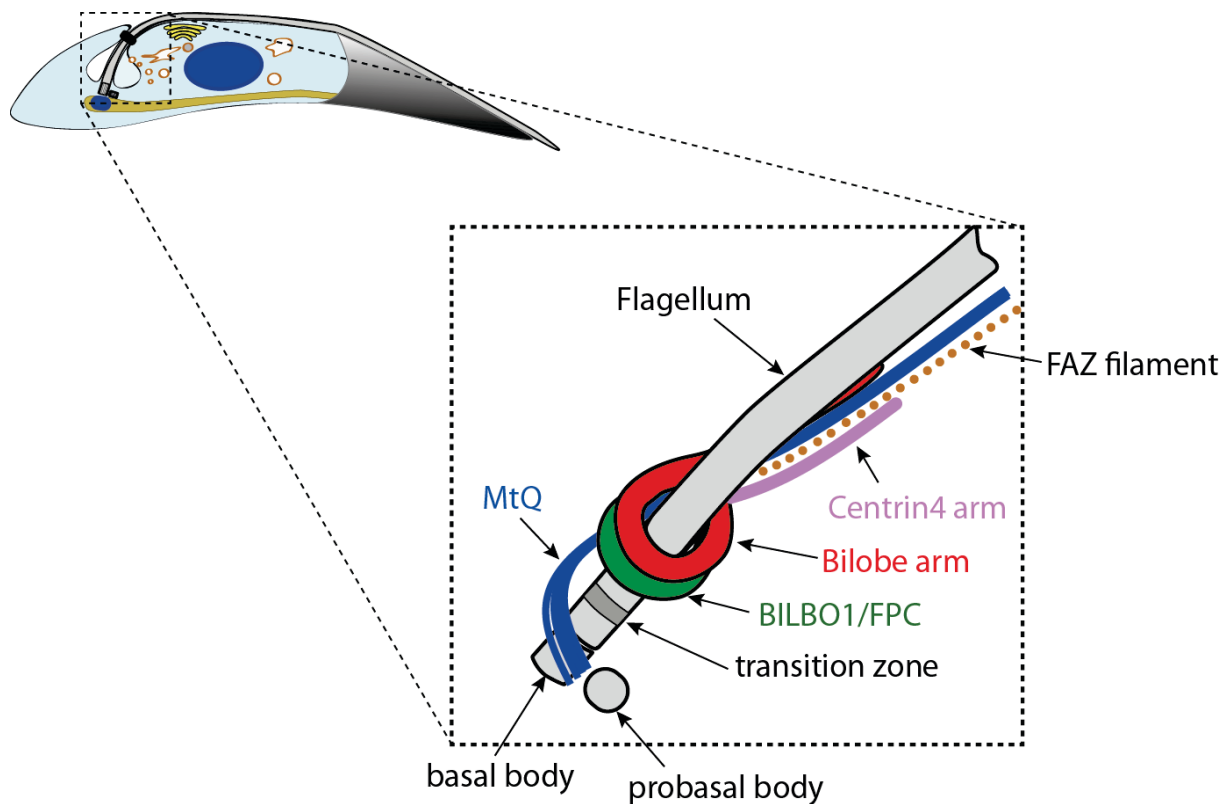


Figure 5 Schematic position of the FPC relative to other cytoskeletal components.

The FPC is an electron dense structure that encircles the flagellum at its membrane exit site. The FPC is positioned beneath the bilobe hook structure. It is dislocated in the region where the MtQ passes by along the flagellum (on the other side of the figure). The figure is adapted from (Esson, Morriswood et al. 2012).

3.5 TbBILBO1

TbBILBO1 was the first component of the FPC to be identified (Bonhivers, Nowacki et al. 2008). Based on primary sequence analysis, TbBILBO1 appears to consist of four structured domains - an N-terminal domain (NTD, residues 1-110), two putative EF-hands (EFh, residues 183-213 and 219-249), a central coiled-coil domain (CCD, residues 263-533), and a C-terminal leucine zipper (LZ, residues 534-578) (Figure 6A). TbBILBO1 is only found in kinetoplastids; no homologous proteins are present in other eukaryotes (Figure 6B) (Bonhivers, Nowacki et al. 2008). The four domains pack closely together in the primary sequence, with the exception of a linker region that lies between the NTD and the EFh. *T. brucei* and *T. cruzi* exhibit a short (6 aa) insertion in this linker region, which is not found in *Leishmania* species. Sequence conservation in the linker region is also lower than in the structured domains.

Depletion of TbBILBO1 protein levels by RNAi causes several effects (Bonhivers, Nowacki et al. 2008). It disrupts the biogenesis of new FP and FPC, causing the detachment of the new flagellum; the new basal body and transition zone are external to the cell body. In the TbBILBO1 RNAi induced cells, no FAZ filament is found along the detached new flagella. This suggests that flagellum and basal body formation are not sufficient for FAZ formation, implying a possible requirement of the FPC and/or FP for FAZ formation (Bonhivers, Nowacki et al. 2008).

Another effect of TbBILBO1 depletion is the inhibition of endocytosis activity (Bonhivers, Nowacki et al. 2008). Since there is no new FP formed in the dividing cells, no endocytosis activity is observed in the new flagellum. It seems that, in the dividing cells, TbBILBO1 depletion induces an endocytic imbalance due to there being only one functional FP instead of two. This is confirmed by the absence of early endocytosis markers such as clathrin and Rab5A near the base of the new flagellum (Bonhivers, Nowacki et al. 2008).

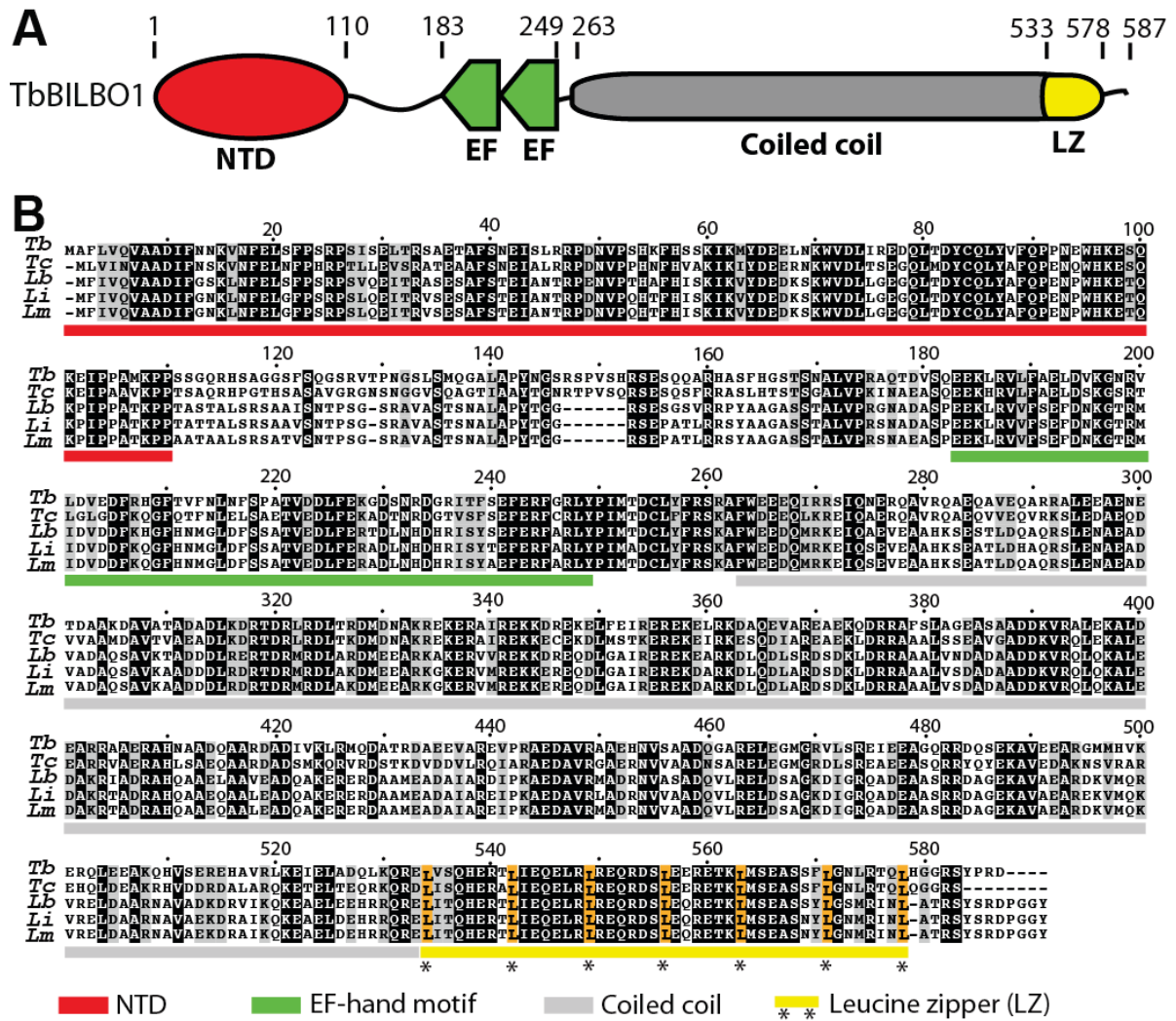


Figure 6 TbBILBO1 domain organization and sequence alignment of homologous proteins.

(A) Schematic depicting the arrangement of the four structured domains of TbBILBO1 - N-terminal domain (NTD), EF-hand (EF), coiled-coil domain (coiled coil), and leucine zipper (LZ). Amino acid numbers are indicated above the diagram. (B) Sequence alignment of TbBILBO1 and homologs from related parasitic kinetoplastids. Identical and similar residues are shaded in black and grey, respectively. Domains are indicated by bars under the aligned sequences using the same color scheme as in (A). Conserved leucines in the C-terminal LZ are highlighted in gold. *T.b.*, *Trypanosoma brucei*; *T.c.*, *T. cruzi*; *L.b.*, *Leishmania braziliensis*; *L.i.*, *L. infantum*; *L.m.*, *L. major*.

3.6 Protein structure determination by multidimensional NMR spectroscopy

NMR spectroscopy measures the quantum mechanical properties of the atomic nucleus, which depends on its local molecular environment. NMR spectroscopy provides visualization of how atoms are chemically linked, how close they are in space, how they interact, and how rapidly they move with respect to each other. The interaction of external magnetic fields with the magnetic moment of atomic nuclei causes the promotion of nuclear spin from a ground state to an excited state. The lifetime of the excited state of the nuclear spin is approximately 10^9 times longer than that of an excited electron. This implies that the long lifetime of the excited state has very narrow spectral lines. Therefore, small organic molecules that have line widths below 1 Hz are easily resolved. The long lifetime of the excited state also facilitates the application of multi dimensional spectroscopy and allows the measurement of molecular dynamics over a wide range of time scales (Rule and Hitchens 2006).

NMR spectroscopy is able to determine protein structures in solution. However, to date it is limited to proteins with molecular weights below 40-60 kDa; therefore NMR spectroscopy provides an alternative method for structure determination if a protein that cannot be crystallized is relatively small. Other than that, NMR spectroscopy is also useful to detect molecular motions and inter-molecular interactions in solutions, such as protein-protein, protein-DNA/RNA, or protein-drug interactions (Rule and Hitchens 2006).

The process of protein structure determination by NMR is depicted in Figure 7. The first step is sample preparation. The protein sample must be very pure and well folded in solution, and should consist of about 300-600 μ l with the concentration about 1 mM. The purity of the sample is very important since even minor macromolecular impurities may affect the result (Wuthrich 1995). For proteins with large molecular weights (>10 kDa), the sample needs to be enriched with ^{15}N and ^{13}C for heteronuclear NMR experiments.

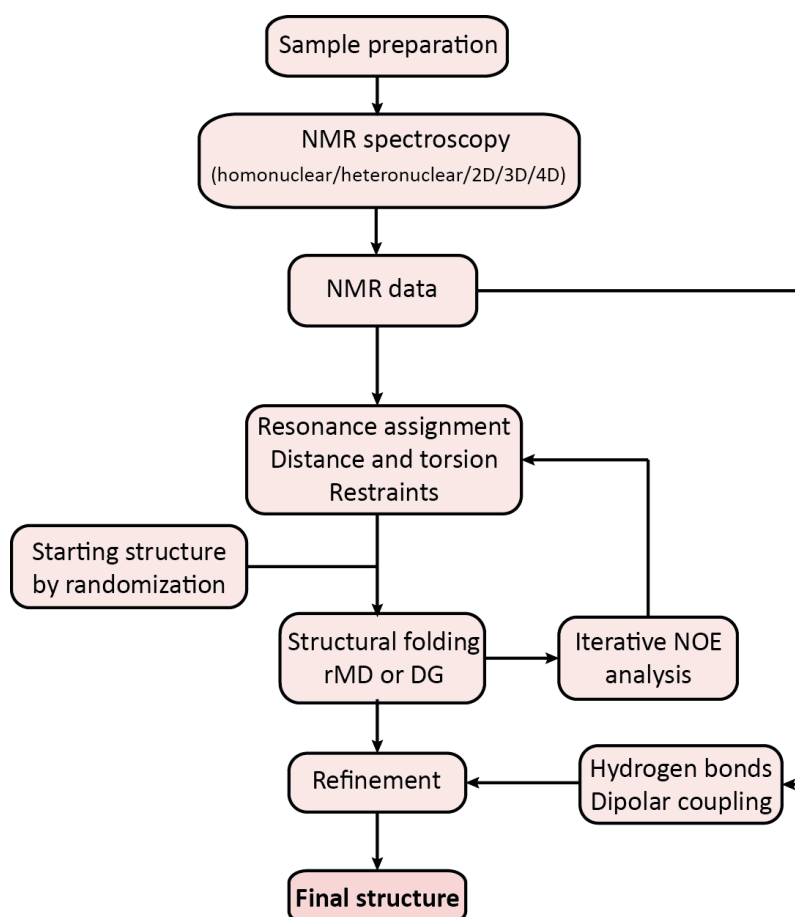


Figure 7 Schematic of the protein structure determination process by NMR.

The process begins with sample preparation, NMR experiments, and data processing. Then it is followed by sequence assignment, NOESY assignment, and other conformational restraints and finally structure calculation and refinement to produce the final structural model. Adapted from (Wuthrich 1995; Teng 2005).

Large numbers of resonance lines in the ^1H NMR spectrum that can be observed as separate peaks are needed for structure determination. It also requires the establishment of selective correlations between pairs of spins. Moreover, since the information about three-dimensional structure primarily comes from NOE distance constraints that give ^1H - ^1H distances in space within 5 Å, the maximum number of ^1H - ^1H NOEs must be resolved and identified. These requirements can be achieved by the implementation of multidimensional NMR (Wuthrich 1995). The differences and the advantages of each dimension of NMR experiments are depicted in Figure 8. In the one dimensional (1D) ^1H NMR spectrum, most of the resonance peaks are overlapping with only a small percentage of well-separated resonance lines. In the two dimensional (2D) ^1H NMR spectrum, even though the diagonal corresponding peaks are overlapping, the additional cross peaks in the 2D frequency plane which correspond to the correlation

between pairs of diagonal peaks are much better resolved than in the 1D NMR spectrum. However, with increasing molecular weight of the molecule, the number of NMR peaks also increases. Therefore it becomes more difficult to resolve the overlapping peaks and assign each individual resonance. To overcome this problem, the implementation of three dimensional (3D) NMR methods is a rational choice. Protein uniformly labeled with ^{15}N and ^{13}C is used to record the heteronuclear 3D spectra. This produces more dispersed peaks in a third dimension along the ^{15}N and ^{13}C chemical shift axes; therefore in addition to the ^1H NMR, ^{13}C and ^{15}N NMR information can be acquired for structure determination.

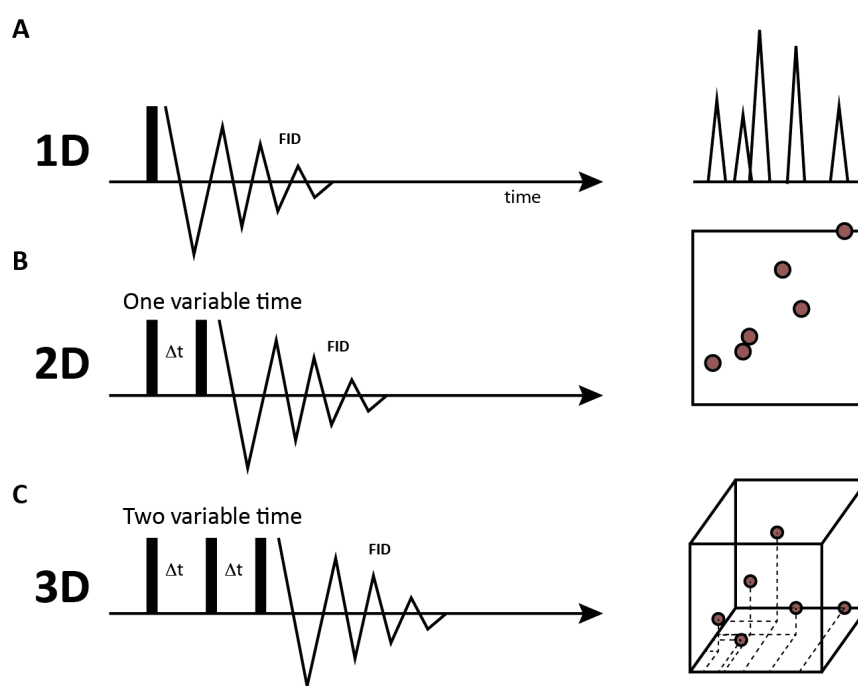


Figure 8 Schematic of NMR spectra of 1D, 2D, and 3D.

(A) In 1D NMR, a large number of resonance peaks are overlap. (B) The 2D NMR can resolve some of the overlapping resonance peaks, but as the sample molecular weight increases, some of overlapping peaks still cannot be resolved. (C) In 3D NMR, most of the overlapping peaks in 1D and 2D NMR can be distinguished. FID = free induction decay.

Structure determination with NMR needs to identify the spectral resonances before using the structural information and relaxation parameters to build a model (Figure 9). The standard initial heteronuclear experiment before other 3D heteronuclear experiments is the 2D ^1H - ^{15}N heteronuclear single quantum coherence (HSQC) experiment (Bodenhausen and Ruben 1980; Cavanagh, Fairbrother et al. 2006). This experiment shows all ^1H - ^{15}N correlations in the amide groups of the protein (mainly

backbone amide groups and also Trp side chain $N\epsilon$ - $H\epsilon$ groups and Asn/Gln side chain $N\delta$ - $H\delta$ / $H\epsilon$ - $H\epsilon$ groups). In this experiment, the magnetization is transferred from a 1H to its attached ^{15}N via the $^1J_{N-H}$ -coupling and the chemical shift is evolved on ^{15}N nuclei. The magnetization is then transferred back to 1H for detection.

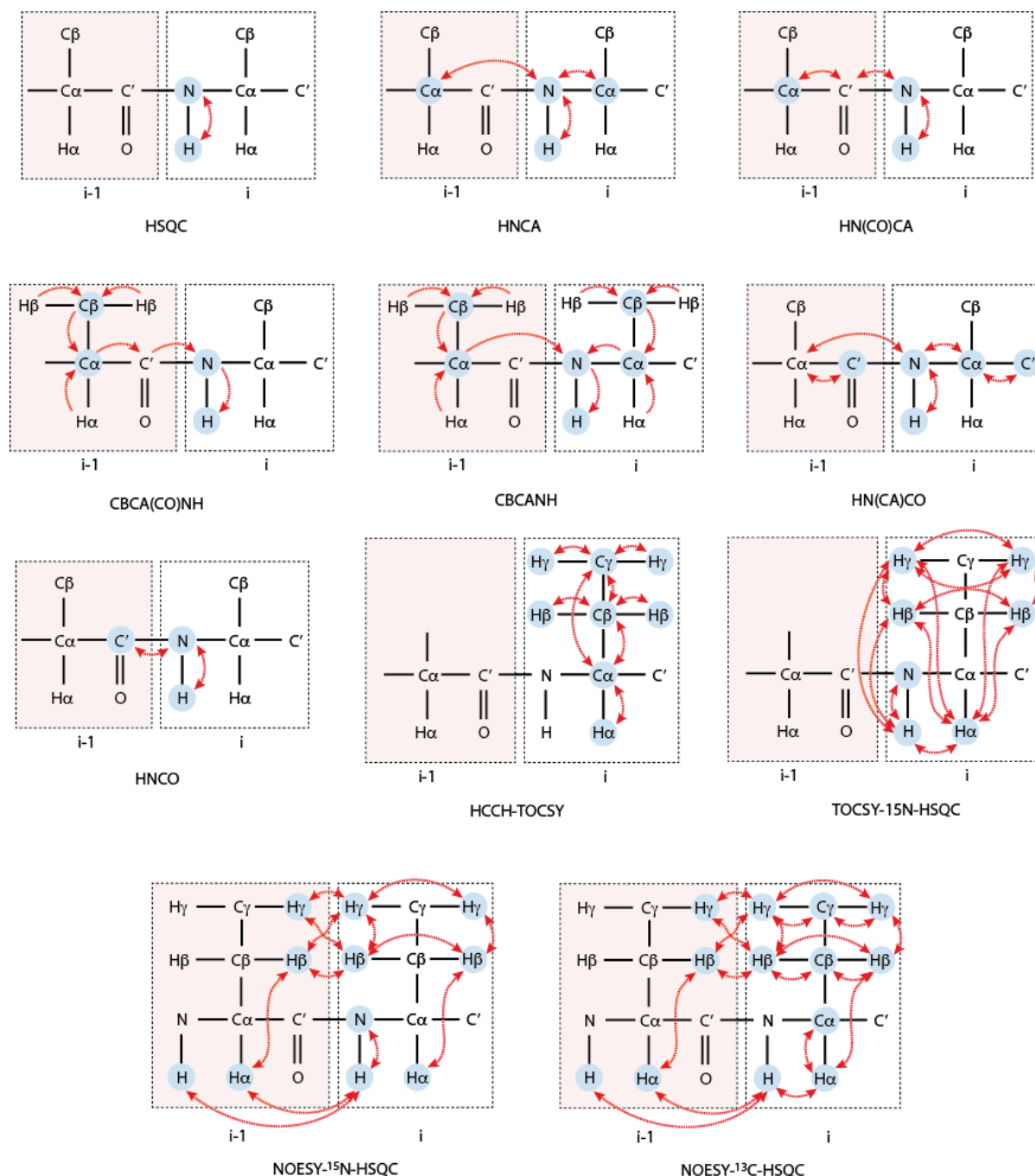


Figure 9 The magnetization pathways (red arrow) and observed correlation (blue shaded nuclei) of the heteronuclear NMR spectroscopy.

The 2D 1H - ^{15}N HSQC experiment is used to show all H-N correlations in the amide groups of the protein. The HNCA, HN(CO)CA, CBCA(CO)NH, HNCACB, HN(CA)CO, and HNCO are 3D heteronuclear experiments to determine sequence-specific assignments of the backbone resonances. The HCCH-TOCSY and TOCSY-

^{15}N -HSQC experiments are used for side-chain assignments. The 3D NOESY- ^{15}N -HSQC and NOESY- ^{13}C -HSQC experiments are to determine the NOE cross peaks between ^1H nuclei in the space. Adapted from (Teng 2005).

The 2D ^1H - ^{15}N HSQC experiment is the experiment performed to analyze whether the protein is well folded in solution or not, and to assess whether other heteronuclear experiments are worth performing. Since this experiment detects each backbone amide group in the amino acid (except proline since it does not have the ^1H attached to the ^{15}N of the backbone amide group), the spectrum is rather like a fingerprint of the protein, which needs to be analyzed by sequence-specific assignments. To achieve this, various 3D triple resonance experiments are needed. A typical suite of experiments are HNCA, HN(CO)CA, CBCA(CO)NH, HNCACB, HN(CA)CO, and HNCO. The HNCA experiment gives two backbone correlations - within the residue ($\text{H}_i(\text{N})$, N_i , and $\text{C}_i(\alpha)$) and the preceding residue ($\text{H}_i(\text{N})$, N_i , and $\text{C}_{i-1}(\alpha)$) (Kay, Ikura et al. 1990). In this experiment, the magnetization is transferred from ^1H to ^{15}N and then via the $^1\text{J}_{\text{N-C}\alpha}$ -coupling to the $^{13}\text{C}\alpha$ and then transferred back to ^{15}N and ^1H hydrogen for detection. The chemical shift is evolved for $^1\text{H}^{\text{N}}$, $^{15}\text{N}^{\text{H}}$ and $^{13}\text{C}\alpha$ producing a 3D spectra.

In the HN(CO)CA experiment, ^1H and ^{15}N chemical shifts of the amide (H_i and N_i) are correlated with the preceding residue ^{13}C chemical shift ($\text{C}_{i-1}(\alpha)$) by relaying it through the $^{13}\text{CO}_{i-1}$ carbonyl for establishment of the backbone sequential connectivity across the peptide bond (Bax and Ikura 1991). In this experiment, the magnetization is transferred from ^1H to ^{15}N , continued to $^{13}\text{C}'$, then to $^{13}\text{C}\alpha$. Here, the chemical shift is evolved. The magnetization is transferred back via $^{13}\text{C}'$ and ^{15}N to ^1H for detection. The combination of information acquired from HNCA and HN(CO)CA experiment are useful for distinguishing both intra- and inter-residue connectivities.

The CBCA(CO)NH experiment correlates the chemical shifts of both $\text{C}_{i-1}(\alpha)$ and $\text{C}_{i-1}(\beta)$ carbons with $\text{H}_i(\text{N})$ and N_i (Grzesiek, Dobeli et al. 1992). In this experiment, the magnetization is transferred from $^1\text{H}\alpha$ to $^{13}\text{C}\alpha$ and from $^1\text{H}\beta$ to $^{13}\text{C}\beta$, and then from $^{13}\text{C}\beta$ to $^{13}\text{C}\alpha$. Furthermore, the magnetization is transferred to $^{13}\text{C}'$, then to $^{15}\text{N}^{\text{H}}$ and continued to $^1\text{H}^{\text{N}}$ for detection. The chemical shift is evolved on both $^{13}\text{C}\alpha$ and $^{13}\text{C}\beta$ simultaneously. This experiment provides information about the amino acid type of the preceding residue.

In combination with the CBCA(CO)NH experiment, the HNCACB or CBCANH experiment is performed. The HNCACB experiment correlates resonance of $H_i(N)$ and N_i with $C_i(\alpha)$ and $C_i(\beta)$, and $C_{i-1}(\alpha)$ and $C_{i-1}(\beta)$ carbons (Grzesiek, Dobeli et al. 1992). In this experiment, the magnetization is also transferred from $^1H\alpha$ to $^{13}C\alpha$ and from $^1H\beta$ to $^{13}C\beta$, and then from $^{13}C\beta$ to $^{13}C\alpha$. However, the magnetization is then directly transferred to ^{15}NH and continued to 1HN for detection. The magnetization from $C_{i-1}(\alpha)$ can be transferred to both $^{15}N_{i-1}$ and $^{15}N_i$; therefore every residue has two $C\alpha$ and $C\beta$ visible peaks. The chemical shift is evolved both on $^{13}C\alpha$ and $^{13}C\beta$ simultaneously, and also in ^{15}NH and 1HN .

The HN(CA)CO experiment correlates the resonance of $H_i(N)$ and N_i with C_i' (Clubb, Thanabal et al. 1992). In this experiment, the sequential connectivities from $H_i(N)$ and N_i with C_{i-1}' can be observed, similar to the HNCA experiment. The magnetization is transferred from 1H to ^{15}N and then to $^{13}C\alpha$ via N- $C\alpha$ J-coupling. Then, via the $^{13}C\alpha$ - $^{13}C'$ J-coupling, the magnetization is transferred to the $^{13}C'$. Finally, the magnetization is transferred back to 1H for detection. The chemical shift is evolved on 1H , ^{15}N and $^{13}C'$. Since the amide nitrogen is coupled to both the $C\alpha$ of its own residue and the preceding residue, both of these transfers occurs and then transfer back to both $^{13}C'$ nuclei.

The HNCO experiment correlates the resonance of $H_i(N)$ and N_i with C_{i-1}' but not C_i' because N_i - C_i' J-coupling value is close to zero (Kay, Ikura et al. 1990). The magnetization is transferred from 1H to ^{15}N and then to the $^{13}C'$ via the ^{15}NH - $^{13}C'$ J coupling, and transferred back via ^{15}N to 1H for detection. The chemical shift is evolved on these three nuclei. The C' chemical shift from this experiment can be used for secondary structure prediction; for example using program TALOS (Shen, Delaglio et al. 2009).

For side-chain assignment, HCCH-TOCSY, TOCSY- ^{15}N -HSQC, and HNHA experiments are often used (Marion, Driscoll et al. 1989; Bax, Clore et al. 1990; Garrett, Kuszewski et al. 1994). The HCCH-TOCSY experiment correlates all aliphatic 1H and ^{13}C spins within residues (Marion, Driscoll et al. 1989). It is used to assign aliphatic 1H and ^{13}C resonances and connect the chemical shift of the side-chain with the backbone assignments. The magnetization is transferred from the side-chain of 1H nuclei to the attached ^{13}C nuclei, followed by isotropic mixing of ^{13}C and then back to the 1H side-

chain for detection. In the TOCSY- ^{15}N -HSQC experiment, the isotropic mixing transfers the magnetization between ^1H spin, then to the neighboring ^{15}N , and then back to ^1H for detection (Bax, Clore et al. 1990). This experiment is used to identify the amino acid types. The HNHA experiment correlates $^1\text{H}^{\text{N}}$ and ^{15}N with $^1\text{H}\alpha$ (Garrett, Kuszewski et al. 1994). Complementary to TOCSY experiment, the HNHA experiment can unambiguously identify $\text{H}\alpha$ protons.

As mentioned before, the three-dimensional structure information primarily comes from NOE distance constraints. However, with the large molecular weight of a protein, the overlapping signal of ^1H spins becomes more severe, which prevents the precise interpretation of the spectrum (Wuthrich 1995). Therefore, 3D heteronuclear-edited experiments are required to resolve this problem by combining two 2D pulse sequences, for example 3D Nuclear Overhauser Effect spectroscopy (NOESY)- ^{15}N -HSQC and 3D NOESY- ^{13}C -HSQC experiment (Marion, Driscoll et al. 1989). These experiments are able to detect close inter-proton distances in the space with a maximum distance of 5-6 Å. The 3D NOESY-HSQC is generated by the combination of HSQC and NOESY experiments after removing the acquisition period of the NOESY and the preparation period of HSQC. In the 3D NOESY- ^{15}N -HSQC, the magnetization is exchanged closely among all interacting ^1H using the NOE; and then transferred to neighboring ^{15}N and finally transferred back to ^1H for detection. Similar with the 3D NOESY- ^{15}N -HSQC, in the 3D NOESY- ^{13}C -HSQC experiment, the magnetization is exchanged among all spatially close ^1H using the NOE, then transferred to neighboring ^{13}C and finally transferred back to ^1H for detection. The resulting spectra from both experiments provide distance restraints for structure calculations.

After NMR data collection, processing and interpretation, the next steps of protein structure determination are constraint assembly, model building and refinement based on the constraints, and interpretation of the models to resolve potential errors in the experimental data (Rule and Hitchens 2006). The input data comprise experimental and non-experimental data. The experimental constraints usually comprise of inter-proton distances (from NOESY experiments), bond orientations (from single bond RDCs), torsion angles (from three bond ^3J -coupling measurements), hydrogen bonds (from amide exchange data), and peptide main chain torsion angles (from chemical shifts or ^3J

coupling constants). Non-experimental constraints include bond angles, torsion angles, improper torsions, bond lengths, and Van der Waals interactions.

For structure calculations, some important parameters need to be generated - the chemical shifts that give most of the protein's secondary structure information, the J coupling constants that give the geometric angle within molecules, NOEs that give ^1H - ^1H distances within 5-6 Å, and RDCs that give structural restraints. Several algorithms exist for structure calculation, such as metric matrix distance geometry (DG-II) and restrained molecular dynamics (rMD) (XPLOR). The distance geometry approach is performed to produce structures with the distance and restraints orientation from NOEs and J coupling constants using a metric matrix or dihedral angle space distance algorithm. Meanwhile, the restrained molecular dynamics approach is performed by calculating the structures using NMR restraints and energy minimization with potential energy functions using the following equation:

$$V_{\text{tot}} = V_{\text{classic}} + V_{\text{NOE}} + V_{\text{j coupling}} + V_{\text{Hbond}} + V_{\text{dipolar}} + V_{\text{cs}} + V_{\text{other}}$$

V_{classic} is the potential function of the molecular classical energy, which consists of V_{bond} , V_{angle} , V_{dihedral} , $V_{\text{van der waals}}$, and $V_{\text{electrostatic}}$. The other pseudo-energies (V_{NOE} , $V_{\text{j coupling}}$, V_{Hbond} , V_{dipolar} , V_{cs} , and V_{other}) are derived from the NMR data. The local minima energy barriers are solved by energy minimization using molecular dynamics (Teng 2005).

The molecular dynamics simulation is performed to solve Newtonian motion equations using the forces generated by the potential energy variations as a function of the protein structures. The accurate and stable simulation is maintained by keeping the time step for integration smaller than the fastest molecular local motion (usually using time step in the range of femtoseconds for simulation in picoseconds). To overcome the energy barriers of the system, the simulation temperature of the system is raised sufficient to increase the kinetic energy during the simulation and pass through higher energy barriers. Then, the system is slowly cooled down to room temperature. During this process, the system energy is minimized over the potential energy surface to find stable structures at lower temperatures. The heating and cooling processes are repeated many times until an ensemble of stable structures with acceptable final parameters is achieved. After refinement, the final ensembles of structures with the lowest energy and acceptable parameters are checked for their accuracy by some programs, such as

PROCHECK and WHAT_CHECK. These programs examine the values of bond lengths and angles, the Ramachandran diagram, the number and scale of violations, of experimental restraints, potential energy, and others (Teng 2005).

3.7 Protein structure determination by X-ray crystallography

Besides NMR, another method for high-resolution protein structure determination is X-ray crystallography. This method can determine the macromolecular structures accurately and precisely to atomic resolution. Currently, most of the protein structures (about 90%) deposited in the PDB are determined by X-ray crystallography with only about 10% of them determined by NMR (Rupp 2010).

The flowchart to determine a protein structure by X-ray crystallography is shown in Figure 10. As a starting point, a high-quality crystal of the pure protein needs to be produced; this is often the bottleneck for X-ray crystallography. For that, cloning and preparation of different protein constructs needs to be done to obtain pure and easily crystallized protein. Some of the protein construct preparations that are commonly used involve using different affinity tags, limited truncation experiment to determine stable domains, different vectors, and different expression hosts. Once a pure, soluble, and stable protein is produced, the next step is to do initial crystallization screening. If initial screening produces some crystal hints, optimization is needed to get single and nicely diffracting crystals. Some of the optimizations often performed involve variation of buffer and pH, temperature, salt concentration, and precipitant. The proteins in the crystal are highly ordered with ideally every molecule in precisely the same position relative to its neighbors. The crystals suitable for X-ray diffraction are then harvested from their mother liquor and mounted on a diffractometer for data collection. Since the protein crystals are susceptible to severe radiation damage in the X-ray beam, cryocooling of the crystals to cryogenic temperatures is necessary to reduce damage (Hendrickson 1976). During this process, the formation of crystalline ice in the mother liquor around the crystal must be avoided because it will destroy the sensitive protein crystals. For that, the optimization of cryoprotectant solution is needed.

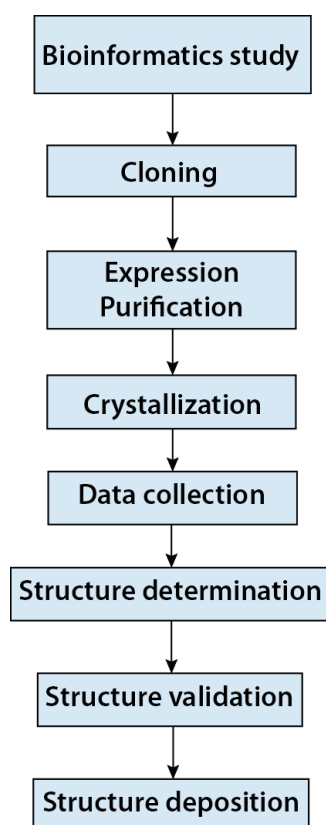


Figure 10 Flowchart of protein structure determination by X-ray crystallography.

The next step is to place the crystal in an X-ray beam to test for diffraction and/or data collection. When the X-ray beam (from an in-house source or synchrotron) encounters the crystal, its scattering can be observed in all directions. This scattering is the amplified contribution of every molecule in the periodic crystal lattice, which is discretely sampled in diffraction spots at diffraction angles given by Bragg's law ($2d_h \sin \theta = n\lambda$; where d is interplanar spacing, λ is wavelength of the X-ray beam, and θ is the impinge and reflected beam angle on the plane, and n is an integer).

The overall scattering in a given reciprocal lattice direction \mathbf{h} is proportional to the sum of all scattering factor (f_j) contributions of each and every j atoms at position \mathbf{x}_j in the unit cell, which reverses as complex structure factor $\mathbf{F}_\mathbf{h}$.

$$\mathbf{F}_\mathbf{h} = \sum_{j=1}^{atoms} f_{s,j}^0 \exp(2\pi i \mathbf{h} \mathbf{x}_j)$$

with $\mathbf{h} \cdot \mathbf{x}_j$ being a dimensionless scalar product. Every atom j in the unit cell contributes a partial wave to every reflection \mathbf{h} (Rupp 2010). Therefore the scattered radiation should be recorded as much as possible by the X-ray detector.

The diffraction images recorded on the detector are then indexed, integrated, scaled, and the unit cell and space group are determined. There are two kind of information obtained from the diffraction images - the first is the geometrical arrangement of the reflections that gives information about the crystal lattice and crystal symmetry, and the second is the intensity of the reflection that gives some information about the content of the lattice (but lacks the phases). During indexing of the diffraction images, the spots found are analyzed, named with integer numbers of Miller indices (h, k, l) and the crystal geometry is determined so the intensities can be integrated accurately (Evans 2006). The raw intensity of the measured and indexed diffraction spots are then converted into a list of scaled intensities and their estimated standard error. It is then integrated and partial reflections are combined into single reflections. The integrated raw data contains the list of indices, the reflection intensity of each reflections, its standard error, and additional batch information for each frame. The data reduction is then applied with merging and scaling of multiple measurements of identical reflections based on initial indexing. The result is a reduced data set containing all reflections, but not yet the further merged symmetry equivalents. The reduced data is further analyzed to determine the Laue symmetry and the space group. Laue symmetry is the symmetry of the reciprocal space. The space group is a group of symmetry operations using one to three generators, which give rise to the general 230 (63 chiral) different arrangements of motifs in a 3D periodic crystal structure.

The measured intensities and reflections of the diffraction images only provide the amplitude of the diffracted X-ray without the phase relations between the reflections. These phases are necessary for reconstruction of the electron density. Therefore, direct reconstruction of the electron density of the macromolecules via Fourier transforms from the intensity/amplitude data alone is not possible. To overcome this problem, there are two methods that can be implemented. First is by the molecular replacement method (Messerschmidt 2007). In this method, a similar previously-determined structural model is used to calculate the initial phases. These initial phases are then used

for initial reconstruction of the electron density. This process involves searching for the correct position of the search molecule in the crystal.

The second method is by experimental phasing. This method is used if no suitable structural model is known. Experimental phasing depends on the determination of the marker atom substructure by exploiting the different intensities of isomorphous data sets. This method requires the incorporation of heavy atoms into the crystal. The isomorphous differences are calculated from the native and derivative crystals. The heavy atoms' ability to absorb X-rays at specific wavelengths also can be used to obtain phases from heavy atom derivatives. As the result, the reflections hkl have different intensities to the reflections $h\bar{k}l$. This inequality of symmetry-related reflections is called anomalous scattering. This technique is generally applicable for atoms heavier than H, C, N, and O, such as sulfur and selenium. Selenium can be used as the marker atom substructure because the amino acid methionine can be replaced with selenomethionine (SeMet) by overexpressing the protein in a suitable expression system. The Se in SeMet provides a site-specific source of an anomalous phasing signal (Strub, Hoh et al. 2003).

After the electron density map is obtained from the improved experimental phases, the protein structure model must be built and fit into the electron density. The initial model produced is then refined to adjust the atomic position coordinates and to achieve the minimum B-factor of the model compared to the observed diffraction data. During refinement, other corrections such as anisotropic scaling and bulk solvent corrections are also applied. The success of refinement is achieved when no more significant and interpretable difference densities in the $mF_o - DF_c$ maps can be observed, no more unexplained significant deviations from stereochemical target values and from plausible stereochemistry are present, and the model makes sense chemically and biologically. To check the correctness of the model during refinement and rebuilding, the models should always be subjected to the validation tools for model stereochemistry examination, such as using PROCHECK and MolProbity software (Laskowski, MacArthur et al. 1993; Chen, Arendall et al. 2010). Finally, after validation, the model structure is then deposited in the PDB.

4 Aims of the study

TbBILBO1 is the first protein component of the FPC to be identified and its depletion by RNAi causes disruption of FP/FPC biogenesis and inhibition of endo-/exocytosis activity. Furthermore, orthologs of TbBILBO1 are found in all trypanosomatids, but no homologous proteins are present in humans. Therefore, TbBILBO1 represents a plausible candidate for rational drug design. To date, no structural information of the protein is known. The availability of TbBILBO1 structural information will not only improve our understanding about the architecture and assembly of this protein in the FPC, but will also shed light for rational drug designs targeting this protein. Therefore, the aim of the project was to carry out structural dissections of TbBILBO1 by a combinatorial strategy involving X-ray crystallography, NMR spectroscopy, and electron microscopy. We further employed site-directed mutagenesis, *in vivo* immunofluorescence, and other biochemical methods, to analyze the TbBILBO1 assembly mechanism at the FPC *in vivo*.

5 Materials and methods

5.1 Antibodies and reagents

HRP-conjugated anti-mouse and HRP-conjugated anti-rabbit antibodies were purchased from Pierce and Dianova, respectively. A mouse anti-alpha-tubulin antibody and anti – green fluorescent protein (anti-GFP) were purchased from Roche. Alexa Fluor 488 goat anti-mouse and Alexa Fluor 568 goat anti-rabbit secondary antibodies were purchased from Invitrogen. The rabbit anti-LdCentrin4 polyclonal antibody and mouse monoclonal anti-Ty1 (BB2) antibody were gifts kindly received from Hira Nakhasi (FDA) and Cynthia He (National University of Singapore). 5 nm Ni-NTA-Nanogold® was purchased from Nanoprobe. Annexin V-FITC apoptosis detection Kit was purchased from eBioscience®. Ammonium chloride (15N, 99%) and D-Glucose (13C, 99%) were purchased from Cambridge Isotope Laboratories, Inc. and Euriso-top, respectively.

5.2 Cloning and site-directed mutagenesis

The full-length TbBILBO1 (TbBILBO1-FL) open reading frame was amplified by PCR from genomic DNA and ligated into the commercial vector pET15b (Novagen) and the custom vector HM15b. The vector pET15b provides an N-terminal 6×His tag (cleavable by thrombin). The custom vector HM15b was generated from vector pET15b, providing an N-terminal 6×His tag (cleavable by thrombin) and an N-terminal maltose binding protein (MBP) tag. The TbBILBO1-NTD (aa1-110) for NMR structure determination and the TbBILBO1-NTD' (aa1-120) for complex formation with the FPC4 were cloned into pET15b (Novagen). Truncations of TbBILBO1 [TbBILBO1-CCD (aa262-533), TbBILBO1-ΔNTD (aa111-587), TbBILBO1-ΔEFh (Δaa183-249), TbBILBO1-ΔLZ (aa1-533)] for rotary metal shadowing EM experiments were subcloned from the TbBILBO1-FL constructs. For the generation of stable cell lines, the TbBILBO1-FL and TbBILBO1-

Δ NTD open reading frames were amplified from the HM15b-TbBILBO1-FL shuttle vector by PCR with the addition of *Hind*III and *Bam*HI restriction enzyme sites and a 5'-end sequence encoding a Ty1 epitope tag. They were ligated into the pLEW100 expression vector using *Hind*III and *Bam*HI sites to generate the pLEW100_TbBILBO1 plasmids.

For crystallization of the TbBILBO1-NTD, DNA encoding the TbBILBO1-NTD+EFh (aa1-249; MW: 28.2 kDa) was amplified from the HM15b-TbBILBO1-FL by PCR with the primers 5'- GCAGCTGCATATGGCGTTTCTCGTACAAGTAG -3' and 5'- CGACGGATCCTTAGATTTGTTCTTCTTCCCAAAAAGC -3', which contain *Nde*I and *Bam*HI restriction sites, respectively. After double digestion by *Nde*I/*Bam*HI, the DNA product was ligated into the custom expression vector, MalpET. This vector provides an N-terminal MBP tag plus a 10 \times His tag, which are cleavable by the *tobacco etch virus* (TEV) protease. The incorporated sequence was subsequently checked by DNA sequencing.

For crystallization of the TbBILBO1 complex filament junction, the TbBILBO1-NH (N-terminal half, aa1-370) and the TbBILBO1-CH (C-terminal half, aa400-587) were subcloned from the HM15b-TbBILBO1-FL. The TbBILBO1-NH was cloned into the MalpET vector and the TbBILBO1-CH was cloned into pET-15b (Novagen).

The plasmids pET28a-FPC4-FL and pET28a-FPC4-CTD (aa357-440) were provided by Drs. Derrick Robinson and Melanie Bonhivers (Universite Bordeaux Segalen, France). The shorter construct consisting of residues 394-444 was amplified by PCR from the plasmid pET28a-FPC4-FL and ligated into the custom expression vector MalpET.

Mutations in the NTD of TbBILBO1 were generated by site-directed mutagenesis using a QuikChange kit (Stratagene) on the pLEW100_TbBILBO1-FL plasmid according to the manufacturer's instructions. Incorporation of mutations was confirmed by DNA sequencing. Two sets of mutations were generated, encoding Ty1-TbBILBO1-Mut1 (F12A, K15A, K60A, and K62A) and Ty1-TbBILBO1-Mut2 (W71A, Y87A, and F89A).

TbBILBO1 localization constructs were generated by amplification of the relevant portions of the TbBILBO1 open reading frame by PCR, with addition of a *Bam*HI restriction enzyme site and a 5'-end Ty1 epitope tag. The PCR products were ligated into

the pXS2 expression vector using the *Bam*HI site to generate the pXS2-TbBILBO1 plasmids (Bangs, Brouch et al. 1996).

5.3 Cell lines, culture and generation

The procyclic *T. brucei* 29.13 strain was used to generate cells inducibly expressing Ty1-TbBILBO1 constructs (TbBILBO1-FL, -ΔNTD, -Mut1, and -Mut2) (Wirtz, Leal et al. 1999). The pLEW100_TbBILBO1 constructs were linearized by *Not*I digestion and 30μg used to transfect 5×10^7 29.13 cells by electroporation. Electroporation was carried out using a Gene Pulser XCell (Bio-Rad) with the following parameters: 1500V, 25μF, 2 pulses with a 10s interval. Stable transformants were selected for growth in SDM79 medium supplemented with 5 μg/ml phleomycin by limiting dilution. Putative clones were screened for integration of the targeting construct in the genome by PCR, using genomic DNA as a template and primers that annealed within the Ty1 epitope and the 3' site of TbBILBO1 open reading frame. Genomic DNA was isolated using DNeasy genomic DNA isolation kits (QIAGEN). The presence of the engineered point mutations in the mutagenesis constructs was further confirmed by sequencing PCR products obtained from amplification of the integrated transgenes. Inducible expression of Ty1-TbBILBO1 constructs was confirmed by immunoblot and immunofluorescence analysis using anti-Ty1 antibodies.

The procyclic *T. brucei* 427 Lister strain was used for localization of TbBILBO1 targeting constructs. Cells were cultured in SDM79 medium supplemented with 7.5 μg/ml hemin, 20% heat-inactivated fetal calf serum (Sigma-Aldrich) at 27°C. 29-13 cells additionally required 15 μg/ml neomycin and 50 μg/ml hygromycin to maintain T7 polymerase and tetracycline repressor transgenes.

5.4 Protein expression and purification

For NMR structure determination, *Escherichia coli* BL21 (DE3) bacteria were transformed with the plasmid pET15b-TbBILBO1-NTD and grown in LB medium (37°C, overnight). The starter culture was then diluted 1:1000 (v/v) in M9 minimal medium containing $^{15}\text{NH}_4\text{Cl}$ as the sole nitrogen source and ^{13}C D-glucose as the sole carbon source. Bacteria were grown at 37°C to an $\text{OD}_{600} \sim 0.6\text{-}0.8$ and then subjected to cold shock (on ice, 30 min). Recombinant protein expression was induced by addition of 0.5 mM isopropylthio- β -D-galactoside (IPTG) and protein production was continued (16°C, overnight). Cells were harvested by centrifugation in a Sorvall GS3 rotor (6000 \times g, 12 min, 4°C) and cell pellets were resuspended in 25 ml lysis buffer (50 mM Tris-HCl pH 8.0, 300 mM NaCl, 20 mM imidazole, 5% (v/v) glycerol) per 1 L of expression culture. Bacteria were lysed by an EmulsiFlex-C3 homogenizer (Avestin) and then centrifuged (40,000 \times g, 40 min, 4°C) to remove cell debris. The supernatant was filtered (0.45 μm pore size) and loaded onto a Ni-HiTrap column (GE Healthcare) pre-equilibrated with the same lysis buffer. The column was washed with 5 \times column volume (cv) of lysis buffer, and bound protein was eluted by a linear gradient concentration of imidazole (20-600 mM, 10 \times cv) in the lysis buffer. The N-terminal 6 \times His tag was removed by incubation with 2% (w/w) of thrombin (overnight, 4°C). The volume was reduced to 2 ml by centrifugation in an Ultra-15 Centrifugal Filter Unit (Amicon) with a 3-kDa molecular weight cut-off and the protein further purified on a Superdex-200 16/60 column (GE Healthcare) pre-equilibrated with 20 mM Na-Phosphate buffer (pH 7.8) and 100 mM NaCl. The protein was then concentrated to ~ 1 mM in a volume of 0.5 ml for NMR measurements.

For crystallization of the NTD of TbBILBO1, the starter cultures of the TbBILBO1-NTD+EFh construct were diluted in LB media and grown and lysed as described above. The filtered supernatants were loaded onto a Ni-HiTrap column as described above. The N-terminal MBP-His tag was removed by addition of 2% (w/w) of the TEV protease. The sample was dialyzed against the lysis buffer to remove excessive imidazole (overnight, 4°C). The sample was loaded again onto a Ni-HiTrap column to remove the MBP-His tag. The protein in the flow-through fraction was cut by thrombin to separate the NTD from the EFh and then purified on an anion exchange HiTrap QFF column using anion

exchange buffer (20 mM Tris-HCl pH 8.0, 50 mM NaCl, 5% (v/v) glycerol) and a linear gradient concentration of NaCl (50 mM - 1 M, 25×cv). Elution fractions containing the NTD were pooled and further purified on a Superdex-200 16/60 column (GE Healthcare) pre-equilibrated with 20 mM Tris-HCl pH 8.0, 100 mM NaCl, and 5% (v/v) glycerol. The sample was concentrated to a final concentration of 20 mg/ml by centrifugation in an Ultra-15 Centrifugal Filter Unit (Amicon) with a 3-kDa molecular weight cut-off.

SeMet-substituted TbBILBO1-NTD+EFh was expressed using M9 minimal medium supplemented with all amino acids (2 mg/ml) except for methionine. Prior to induction, L-SeMet (80 mg/L), threonine (100 mg/L), lysine (100 mg/L), phenylalanine (100 mg/L), leucine (50 mg/L), isoleucine (50 mg/L), and valine (50 mg/L) were added. The protein was purified as described above using the same buffer with the addition of 15 mM β -mercaptoethanol for purification by Ni-HiTrap and 10 mM dithiothreitol (DTT) for size exclusion chromatography (SEC).

For rotary metal shadowing EM experiments, the starter cultures of the TbBILBO1 truncation constructs were diluted in LB medium and grown and lysed as described above. The filtered supernatants were loaded onto a Ni-HiTrap column as described above.

For TbBILBO1 complex filament junction formation, *E. coli* BL21 (DE3) bacteria were co-transformed with the MalpET-TbBILBO1-NH and pET15b-TbBILBO1-CH constructs. The starter cultures of the constructs were diluted in LB medium and grown and lysed as described above. The filtered supernatants were loaded onto a Ni-HiTrap column as described above. The proteins fraction was cut by thrombin to separate the MBP-TbBILBO1-NTD and His-tag from the complex and dialyzed as described above. The proteins were applied to the second Ni-HiTrap as before to remove the tags. The flow through fractions were then concentrated and applied to SEC as described above.

For complex formation between TbBILBO1 and FPC4, *E. coli* BL21 (DE3) bacteria were co-transformed with the pET15b-TbBILBO1-NTD' (aa1-120) and the MalpET-FPC4-CTD (aa357-440). The starter cultures of the constructs were diluted in LB medium, grown and lysed as described above. The filtered supernatants were loaded onto a Ni-HiTrap column (GE Healthcare) as described above. The further purification with second Ni-His

trap and SEC were performed as described before. A similar method was used to produce the complex of the pET15b-TbBILBO1-NTD' (residues 1-120) and the MalpET-FPC4-CTD' (aa394-444).

5.5 NMR spectroscopy and structure calculations

All NMR experiments were performed at 298 K on Varian Inova 500 MHz and 800 MHz and Varian Direct Drive 600 MHz spectrometers equipped with 5 mm triple resonance probes and pulsed field gradients. NMR spectra were processed with NMRipe, and analyzed with Sparky software (Delaglio, Grzesiek et al. 1995). NMR samples had a concentration of ~1 mM for triple resonance experiments or structure determination. In addition, the sample contained a 5-10% (v/v) $^2\text{H}_2\text{O}$ for field/frequency lock as well as 0.1-0.2% (w/v) NaN_3 to inhibit bacterial growth.

Backbone signal assignment for the TbBILBO1-NTD was obtained by a suite of standard (sensitivity enhanced) 3D triple resonance experiments acquired in pairs: HNCA/HN(CO)CA, CBCA(CO)NH/HNCACB, HN(CA)CO/HNCO were recorded for sequential backbone chemical shift assignment. Side-chain signal assignment of the TbBILBO1 NTD was obtained from 3D TOCSY- ^{15}N -HSQC, HNHA, HCCH-TOCSY, and NOE identification and assignment was obtained from 3D NOE spectroscopy, 3D NOESY- ^{15}N -HSQC and 3D NOESY- ^{13}C -HSQC. Backbone chemical shifts were analyzed using TALOS software (Shen, Delaglio et al. 2009).

To determine a detailed solution structure of the TbBILBO1-NTD, a simulated annealing procedure using the Xplor-NIH software package (version 2.17 and above) was used for structure calculations (Schwieters, Kuszewski et al. 2003). A set of structures were calculated with 1832 experimentally observed NOE constraints from 3D ^{15}N - and ^{13}C -NOESY-HSQC together with 140 backbone torsion angle predictions from TALOS based on chemical shift homology. Final NMR structures were selected for minimal restraint violation and minimal total energy. Structure analysis and calculation of backbone coordinate RMSD values were performed using MOLMOL (Koradi, Billeter et al. 1996).

5.6 Crystallization and data collection of the N-terminal domain of TbBILBO1

An initial crystallization screen was performed at both 277 and 295 K by the sitting drop vapor-diffusion method using commercial crystallization screens: Crystal Screen HT (Hampton Research), JBScreen Classic 1-4 (Jena Bioscience), Morpheus and PACT Premier (Molecular Dimension) in MRC2 well crystallization plates (Hampton Research) using the Crystal Phoenix robot (Art Robbins Instruments). Crystals were observed after 9 days at 295 K in a condition from JBScreen Classic 1-4 (0.1 M Na-acetate, 0.1 M MES-NaOH pH 6.5, 30% (w/v) polyethylene glycol monomethyl ether 2000 (PEGMME 2000)). The crystals could be reproduced only by micro-seeding. For that, original native crystals were crushed and suspended in 50 μ l mother liquor to prepare the seed stock. Crystallization was performed manually by the hanging drop vapor-diffusion method. The drops consisted of 1 μ l SeMet-substituted protein solution, 0.8 μ l mother liquor and 0.2 μ l seed stock, and were equilibrated against 200 μ l of the same mother liquor with varied concentrations of PEGMME 2000. Plate-shaped crystals were obtained from a condition with 0.1 M MES-NaOH pH 6.5, 0.1 M Na-acetate, 35% (w/v) PEGMME 2000, and 5mM DTT after two days. Single crystals of suitable dimensions were transferred into the same mother liquor solution supplemented with 5% (v/v) glycerol as the cryoprotectant, mounted on a CryoLoop (Hampton Research) and flash frozen in liquid nitrogen for X-ray diffraction studies.

Single anomalous dispersion (SAD) data sets at the absorption edge of Se ($\lambda = 0.9792$ Å) were collected on the beamline ID14-4 at the ESRF, Grenoble, France (McCarthy et al., 2009). The 300 frames of diffraction images were collected on the Q315r CCD detector (ADSC) with the oscillation angle of 1.4° per image and crystal-to-detector distance of 241.7 mm. The diffraction images were integrated and scaled using iMosflm (Battye et al., 2011) and SCALA (Evans, 2006), respectively. To locate the selenium sites and calculate the experimental electron density maps, phasing by AutoSol (Phenix suite software) was carried out (Terwilliger, Adams et al. 2009). The model building was done in COOT and refinement was carried out using the phenix.refine program from the Phenix software suite (Emsley and Cowtan 2004; Headd, Echols et al. 2012).

5.7 Crystallization of the complex TbBILBO1-NH and TbBILBO1-CH

An initial crystallization screen was performed in a similar manner to that described above. Crystals were observed after 4 days at 295 K in a condition from the Wizard screen in a condition containing 0.1M phosphate-citrate pH 4.2, 0.2M Li₂SO₄, and 20% (w/v) polyethylene glycol 1000. The crystals could be reproduced only by micro-seeding using the method described above. The initial diffraction experiments were carried out on the beamline ID14-4 at the ESRF in Grenoble, France (McCarthy et al., 2009).

5.8 Rotary metal shadowing electron microscopy

For rotary metal shadowing EM, purified 6×MBP-tagged TbBILBO1-FL, -ΔNTD, -ΔEF, and -ΔLZ were prepared at 0.05-0.1 mg/ml in the EM buffer (100 mM (NH₄)HCO₃-H₂CO₃ pH 7.5, 30% (v/v) glycerol) and sprayed onto freshly-cleaved mica chips. The specimens were dried in a BAF400 high vacuum coater (Balzers, Liechtenstein) for at least 6h and then rotary shadowed with 0.7 nm platinum/carbon at an elevation angle of 5° and backed with 10 nm Carbon at 90°C. Electron micrographs were taken on an FEI Morgagni 268D transmission electron microscope operated at 80 kV equipped with an Olympus-SIS CCD camera. Images were examined and analyzed using ImageJ (<http://rsbweb.nih.gov/ij/docs/menus/analyze.html#gels>).

5.9 Negative staining and nanogold-labeling electron microscopy

For negative staining EM, 6×His-MBP-TbBILBO1-FL purified by Ni-HiTrap column (Novagen) or further purified by SEC was used. For immunogold-labeling EM, 6×His-MBP-TbBILBO1-FL purified by Ni-HiTrap column was further dialyzed against the labeling buffer (50 mM Tris-HCl pH 8.0, 100 mM NaCl, 5% (v/v) glycerol) to remove the

excess of imidazole. Sample was incubated with 5 nm Ni-NTA-nanogold (Nanoprobes) with a 1:50 molar ratio in the labeling buffer (30 min, RT), and loaded onto a Sephacryl S-400 (16/60) gel filtration column (GE Healthcare) to remove the unbound gold particles. Labeled samples were subsequently adsorbed onto glow-discharged Formvar- and carbon-coated copper grids (30 sec) and stained in 2% (w/v) uranyl acetate (2 min, RT). The samples were viewed and images were recorded on an FEI Morgagni 80 kV electron microscope equipped with an Olympus-SIS CCD camera.

5.10 Immunoblots

Whole-cell lysates were prepared in 6×SDS-PAGE loading buffer and boiled for 10 min. Lysate from 2.5×10^6 cells was applied per lane in 10% polyacrylamide bis-Tris gels. Proteins were separated by SDS-PAGE (200 V, 45 min) and transferred to Whatman® Protran® nitrocellulose transfer membrane by wet electrophoretic blotting in transfer buffer (25 mM Tris-HCl pH 8.3, 192 mM glycine, 20% (v/v) methanol, 2% (w/v) SDS) (300 mA, 120 min). To confirm transfer, ponceau S staining (0.1% Ponceau S, 5% (v/v) acetic acid) was performed on the membranes. Membranes were blocked with blocking solution (10% (w/v) milk powder in 1×PBS, 0.3% (v/v) Tween-20) (30 min, RT) and then incubated with the primary antibody (60 min, RT). Blots were washed three times using wash buffer (1×PBS, 0.3% (v/v) Tween-20). Blots were incubated with HRP-conjugated secondary antibody (60 min, RT) and then washed as before. The bound antibodies were visualized by ECL using SuperSignal® West Pico (Thermo Scientific), and the films were imaged using the CURIX 60 (AGFA Healthcare) Image Station. Protein band intensities were analyzed using ImageJ software (<http://rsbweb.nih.gov/ij/docs/menus/analyze.html#gels>).

5.11 Growth inhibition assay

Cells (seeded at 2×10^6 cells/ml) were grown in 10 ml of SDM79 medium with the addition of 0, 5, 10, 20, 40, and 50 ng/ml tetracycline each day to induce and maintain

protein expression. A four-day time course was followed. Culture densities (cells/ml) were measured with a Z2 coulter® (Beckman Coulter™) every day and 2 ml of each was taken for immunoblotting analysis. Growth inhibition due to expression of TbBILBO1 construct at a given tetracycline concentration was calculated after four days with the following formula:

$$\text{Inhibition (\%)} = 100 - x \cdot 100 / x_0,$$

where x is the cell concentration at a given tetracycline concentration and x_0 is the cell concentration in the control (uninduced) population. The results were then plotted against tetracycline concentration using the SigmaPlot software. Tetracycline concentration required to reduce 50% of cells growth (IC_{50}) was determined from experimental cells growth versus drug concentrations by fitting the rectangular hyperbolic function:

$$I = I_{\max} C / (IC_{50} + C),$$

where I is percentage of inhibition, I_{\max} is 100% inhibition, and C is tetracycline concentration (Martin, Grimley et al. 2001).

5.12 Propidium Iodate/Annexin V viability assay

Cells (5×10^6) were centrifuged ($800 \times g$, 5 min) and washed with $1 \times$ PBS. The cell pellet was resuspended in 500 μ l of Annexin V-binding buffer (10 mM HEPES-NaOH pH 7.4, 140 mM NaCl, 2.5 mM $CaCl_2$) and Annexin V-FITC and propidium iodide were added to a final concentration of 5 μ g/ml. The suspension was incubated in the dark for 10 min and the fluorescence intensity was measured on FACS Calibur flow cytometer (BD Biosciences) and analyzed by Flowjo software (version 8.8.7).

5.13 Immunofluorescence microscopy

Cells were washed with 1×PBS, attached to cover slips by centrifugation (3000×g, 5 sec), and fixed in 4% (w/v) paraformaldehyde (20 min, RT). Fixed cells were washed with 1×PBS, permeabilized with 0.25% (v/v) Triton X-100 in 1×PBS (5 min, RT), washed again with 1×PBS, and blocked with 3% (w/v) BSA in 1×PBS (30 min, RT). The cover slips were incubated in a humidified chamber with primary antibodies diluted in 1×PBS (60 min, RT), washed three times with 1×PBS, and then incubated with secondary antibodies diluted in 1×PBS (60 min, RT). After three washes with 1×PBS, the cover slips were rinsed with milli-Q water and mounted on glass slides using Fluoromount G + DAPI (Southern Biotech). For preparation of detergent-extracted cytoskeletons, the cells were incubated in PEME buffer (0.1 M PIPES-NaOH pH 6.9, 2 mM EGTA, 1 mM MgSO₄, 0.1 mM EDTA) plus 0.5% (v/v) NP-40 (5 min, RT), washed three times with 1×PBS, and then treated as described previously for intact cells.

Cells were imaged using an inverted microscope (Axio Observer Z1, Carl Zeiss Microimaging Inc.) equipped with a PCO 1600 camera (PCO) and using manufacturer's drivers in a custom C++ program. A 100x/1.46 Plan-APOCHROMAT oil immersion lens and Immersol 518F (Zeiss) immersion oil were used. Image processing was carried out using ImageJ and Adobe Photoshop CS3 software (Adobe System, San Jose, CA).

5.14 Protein molecular weight determination by static light scattering (SLS)

SLS measurements were carried out on a mini-DAWNTM Treos[®] instrument (Wyatt Technology Corp) connected in-line to an AKTA Purifier equipped with a Superdex-200 10/300 GL SEC column. Before the experiment, the column was equilibrated overnight with the SLS buffer (20 mM Tris-Cl pH 8.0, 100 mM NaCl, and 2mM CaCl₂ or 2mM EDTA pH 8.0). 100 µl of TbBILBO1-EFh (10 mg/ml) was incubated in 2mM CaCl₂ or 2 mM EDTA pH 8.0 (1h, RT). Samples were then injected to the column and run with flow rate

0.5 ml/min. All measurements were done at room temperature. The results were analyzed using the ASTRA program.

5.15 Protein secondary structure determination by circular dichroism (CD)

CD measurements were performed using the Chirascan plus CD spectrometer (Applied Photophysics). 150 μ l of TbBILBO1-EFh (0.05 mg/ml) was incubated in 2mM CaCl_2 or 2 mM EDTA pH 8.0 (1h, RT). CD spectra were collected in duplicate from 190 to 260 nm using a 0.5 cm path-length cuvette. A sampling time per point of 1s, and a bandwidth of 1 nm were used. CD signals of buffer alone were subtracted from all sample measurements.

5.16 Thermal shift assay

This assay was carried out based on a previously-published protocol (Ericsson, U. B., 2006). Solutions of 7.5 ml of 17 \times Sypro Orange (Molecular Probes), 12.5 ml of protein buffer (20 mM Tris-Cl pH 8.0, 100 mM NaCl, and 5% (v/v) glycerol) containing 5 mM CaCl_2 or 5mM EDTA pH 8.0, and 5 ml of TbBILBO1-EFh (2.5 mg/ml) were added to a 96-well thin-wall PCR plate (Bio-Rad), sealed with Opriqual-Quality Sealing Tape (Bio-Rad) and heated in an iCycler iQ Real Time PCR Detection System (BioRad) from 20 to 95 $^{\circ}\text{C}$ with increments of 0.5 $^{\circ}\text{C}$.

6 Structure of the TbBILBO1-NTD from *Trypanosoma brucei* reveals an essential requirement for a conserved surface patch

6.1 Summary

TbBILBO1 is a modular protein with a distinct N-terminal domain with no known structures homologous to it. The results described here provide a high-resolution structure for this domain and a demonstration of its essential requirement *in vivo*. In particular, a conserved aromatic/basic patch is implicated as a potential site for pharmacological blockade.

6.2 Targeting of TbBILBO1 to the FPC

TbBILBO1 is localized to the electron dense material in the neck region of the FP termed the FPC (Bonhivers, Nowacki et al. 2008). To determine which part of TbBILBO1 is responsible for its targeting to the FPC, five different YFP-tagged truncation constructs were tested (Figure 11A). These constructs were transiently expressed in *T. brucei* and their localization analyzed by immunofluorescence microscopy. The expression of all truncation constructs was verified by immunoblots of whole-cell lysates taken from transfected cell cultures (Figure 11B). Full-length (FL) TbBILBO1 localized to a region between the nucleus and the kinetoplast (mitochondrial genome), and close to the point of flagellum entry into the cell (Figure 11C, arrowhead). This is consistent with an FPC localization and matches the distribution seen for the endogenous protein (Bonhivers, Nowacki et al. 2008). TbBILBO1- Δ NTD displayed a similar localization (Figure 11D, arrowhead), suggesting that the NTD was not required for targeting. Consistent with this, TbBILBO1-NTD did not localize to the FPC and exhibited a cytoplasmic distribution (Figure 11E).

A longer construct containing both the NTD and the EFh motifs also did not localize to the FPC (Figure 11F). Deletion of the LZ caused a different effect. This construct (TbBILBO1- Δ LZ) formed numerous cytoplasmic punctae. Although there was a concentration of these punctae in the region of the FPC, they did not correctly localize to the FPC (Figure 11G, arrow). However, the LZ by itself was cytoplasmic (Figure 11H). Therefore, it was concluded that the LZ is necessary but not sufficient for targeting to the FPC. A caveat is that protein levels varied considerably from construct to construct as a result of transient expression, although robust amounts were seen for the main ones (TbBILBO1-FL, -NTD, - Δ NTD, - Δ LZ).

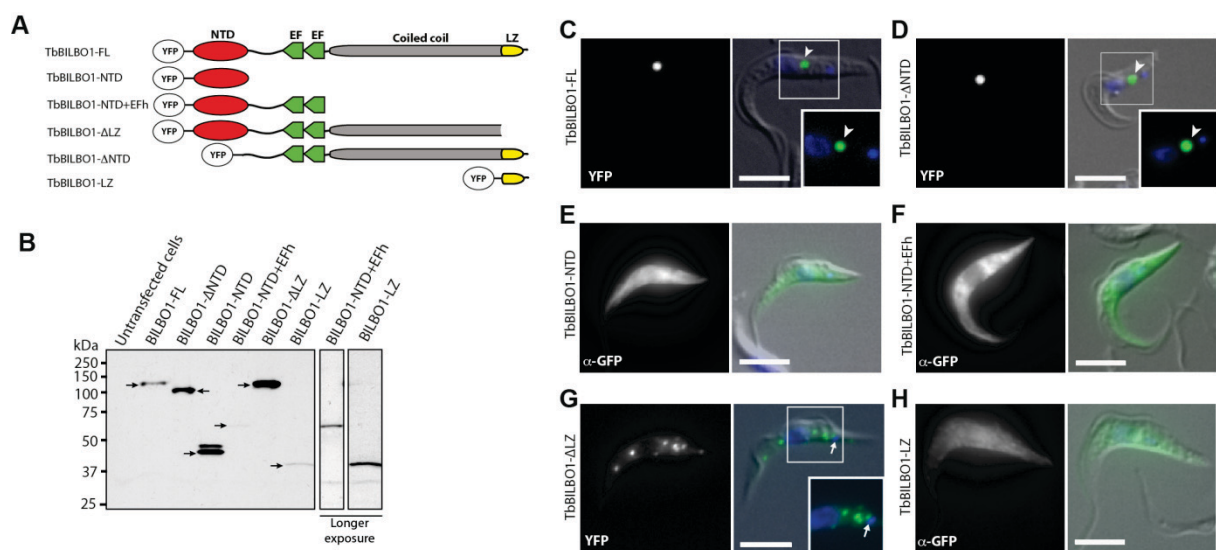


Figure 11 The TbBILBO1-LZ is necessary but not sufficient for targeting to the FPC.

(A) Summary of TbBILBO1 truncation constructs used for the experiment. Abbreviations are defined in the text. (B) Immunoblot of whole-cell lysates from transiently-transfected *T. brucei* cells, probed using anti-GFP antibodies. Arrows indicate the expected size of the YFP-tagged TbBILBO1 constructs. (C-H) Localization of YFP-tagged TbBILBO1 truncations in transiently-transfected *T. brucei* cells. Intact cells were analyzed by immunofluorescence microscopy. When low expression levels precluded observation of YFP, anti-GFP antibodies were used to visualize the protein as indicated. DAPI was used to stain DNA (blue). Regions enlarged in insets are indicated with white boxes. Scale bars, 5 μ m.

6.3 Overexpression of TbBILBO1- Δ NTD has a dominant negative effect on cell growth

As the localization data indicated that the TbBILBO1-NTD was not required for targeting the protein to the FPC, it was hypothesized that it performed a functional role. If so, then

the TbBILBO1- Δ NTD construct lacking the NTD should have a dominant negative effect when overexpressed. To test this, stable cell lines inducibly expressing either Ty1-tagged TbBILBO1-FL or TbBILBO1- Δ NTD were generated. PCR amplification of genomic DNA confirmed that the transgenes were present (Figure 12A). Tight and tetracycline-inducible control over protein expression was confirmed by immunoblotting with anti-Ty1 antibodies (Figure 12B). As expected, both constructs localized correctly to the region of the cell corresponding to the FPC; in the absence of tetracycline no expression was seen (Figure 12C-E). Expression of each construct was then induced over a range of drug concentrations and the effect on cell growth measured. Overexpression of Ty1-TbBILBO1-FL caused only mild growth inhibition even at the maximal concentration of tetracycline tested; however, overexpression of Ty1-TbBILBO1- Δ NTD caused a strong growth defect. Complete growth inhibition was achieved at 20 ng/ml of tetracycline (Figure 12F). This supported the hypothesis that the NTD performs an essential functional role *in vivo*. Immunoblots confirmed that the two constructs had comparable expression levels at each drug concentration (Figure 12G).

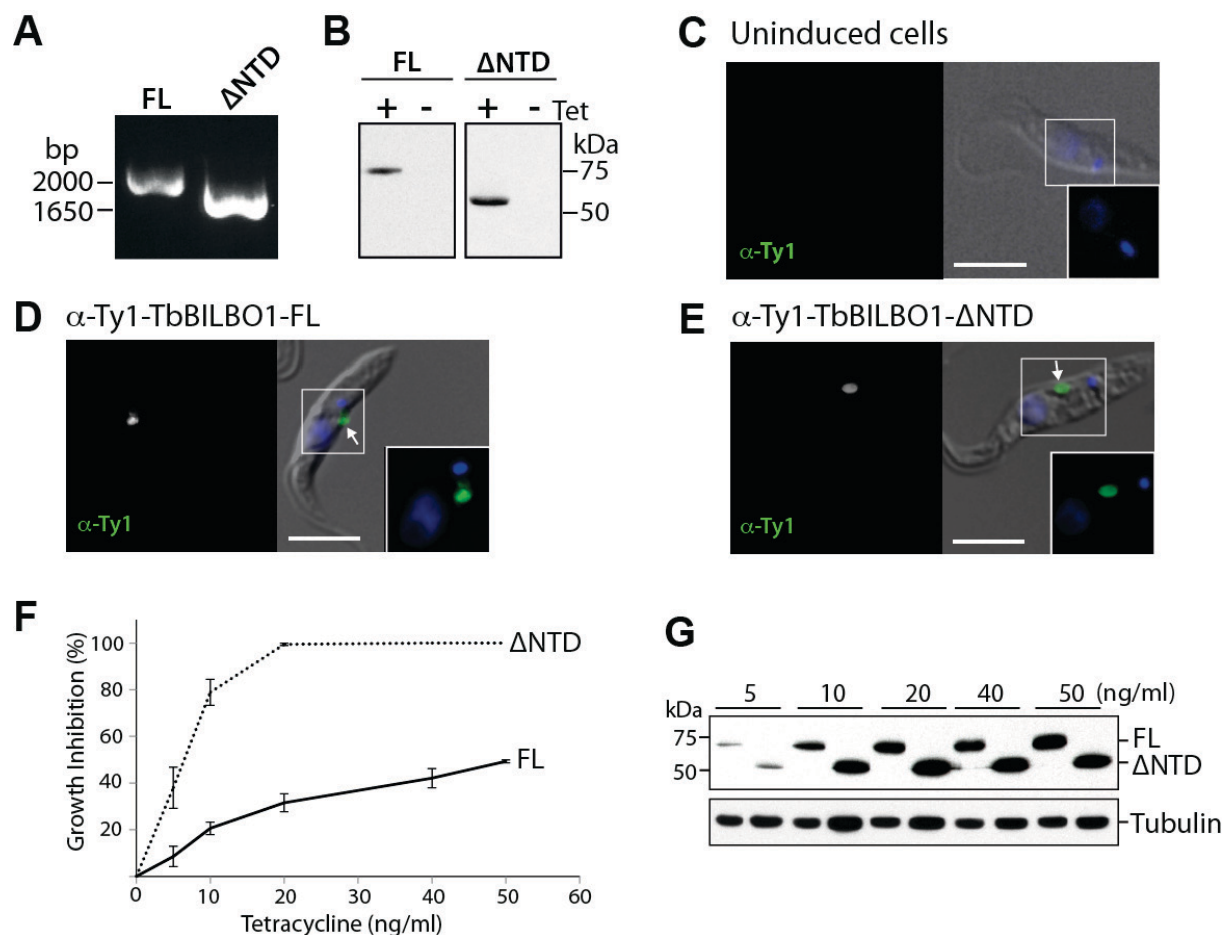


Figure 12 Essential function of the TbBILBO1-NTD.

(A) PCR amplification of genomic DNA from putative clones confirmed the presence of the indicated TbBILBO1 transgenes. Primers annealing to sequences encoding the Ty1 epitope tag (5' end) and ORF (3' end) were used. (B) Immunoblots of whole-cell lysates from cells inducibly expressing the indicated Ty1-tagged TbBILBO1 transgenes in the presence or absence of 20 ng/ml tetracycline. Probing with anti-Ty1 antibodies confirmed that both transgenes were inducibly and tightly expressed. (C-E) The cells were analyzed by immunofluorescence microscopy using anti-Ty1 antibodies to confirm localization. DAPI was used to stain DNA (blue). Scale bars, 5 μ m. (C) No labeling was seen in the absence of tetracycline. (D&E) Ty1-tagged TbBILBO1-FL and - Δ NTD constructs localized correctly. Arrows indicate the point of flagellum entry into the cell. Boxed area enlarged in insets. (F) Growth inhibition curves from stably-transfected cells inducibly expressing Ty1-tagged full-length (FL) or NTD-deleted (Δ NTD) TbBILBO1 at different concentrations of tetracycline by the end of a four day time course. Values were calculated from the mean of at least three independent experiments. Bars show standard errors. (G) Immunoblot analysis of whole-cell lysates taken from cells expressing TbBILBO1-FL and - Δ NTD at different concentrations of tetracycline after four days of induction. TbBILBO1 constructs were detected using anti-Ty1 antibodies (upper panel). An immunoblot using anti-tubulin antibodies was used as a loading control (lower panel).

6.4 NMR structure of the TbBILBO1 N-terminal domain

A search of the protein data bank (PDB) at NCBI by blastp using the primary sequence of TbBILBO1-FL did not lead to any known structures homologous to the TbBILBO1-NTD. This implied that the NTD might have a novel fold. To investigate this, structural studies on the TbBILBO1-NTD were carried out by multidimensional NMR spectroscopy.

Recombinant TbBILBO1-NTD was expressed in *E. coli* and purified to homogeneity (see 5.4). The purified protein was monomeric, soluble, and properly folded as indicated by the well-dispersed resonances in a 1D ^1H NMR (Figure 13A) and 2D ^1H - ^{15}N HSQC spectrum (Figure 13B). Since the TbBILBO1-NTD contains ten prolines, there are ten missing signals in 2D ^1H - ^{15}N HSQC spectrum (Figure 13B).

The 3D structure was subsequently determined by multidimensional NMR spectroscopy. Backbone signal assignment from 3D triple resonance experiments was acquired by sequential walking method using HNCA/HN(CO)CA, CBCA(CO)NH/HNCACB, HN(CA)CO/HNCO spectrums. Figure 13C and D show the results of the sequential backbone chemical shift assignment of HN(CO)CA/HNCA spectrum and HNCO/HN(CA)CO spectrum, respectively. Secondary structure analysis based on backbone chemical shifts of $\text{C}\alpha$ and $\text{C}\beta$ are shown in Figure 14. Amino acids from residue 28 to 46 have propensity to form α -helix and the other residues are tend to form β -strand. Distance constraints were derived from observed NOE intensities; torsion angle

A

B

69

(A) 1D NMR spectrum shows sharp and dispersed proton chemical shifts indicating that the protein is folded. (B) ^{15}N - ^1H correlated HSQC spectrum collected for the TbBILB01-NTD sample at 25°C in a 20 mM sodium phosphate buffer (pH 7.8) containing 100 mM NaCl, 10% (v/v) $^2\text{H}_2\text{O}$, and 0.2% (w/v) NaN_3 . Resonance assignments for all resolved cross peaks are labeled. (C) Example of the sequential backbone chemical shift assignment based on HN(CO)CA/HNCA spectra of residues 64-69. The HNCA spectrum recognizes the $\text{C}_i(\alpha)$ within the residue and the preceding residue; whereas the HN(CA)CO spectrum only recognizes the $\text{C}_i(\alpha)$ of the preceding residue. (D) Example of the sequential backbone chemical shift assignment based on HNCO/HN(CA)CO spectra of residue 66-68. The HN(CA)CO spectrum recognizes the C_i' within the residue and the preceding residue; whereas the HNCO spectrum only recognizes only the C_i' of the preceding residue.

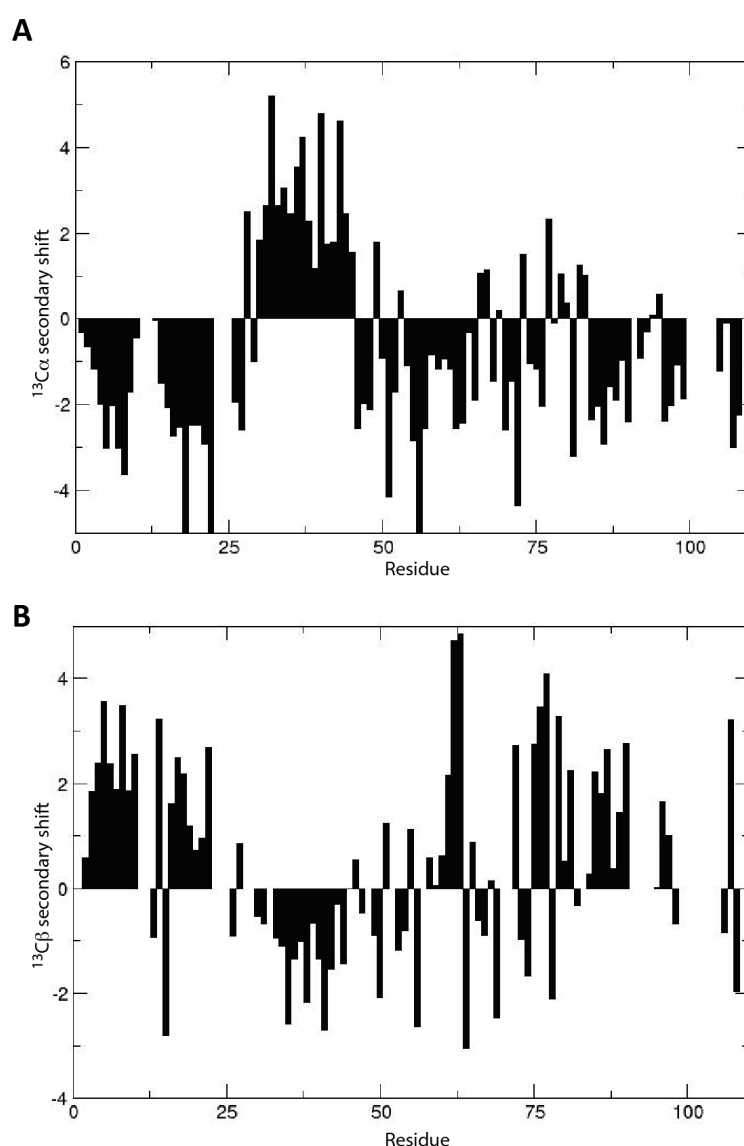


Figure 14 Backbone chemical shifts of the TbBILB01-NTD.

(A) $^{13}\text{C}\alpha$ chemical shifts of the TbBILB01-NTD. The negative shifts correspond to β -strand structures and the positive shifts correspond to α -helix structures. (B) $^{13}\text{C}\beta$ chemical shift. The negative shifts correspond to α -helix structures and positive shifts correspond to β -strand structures, opposite to the chemical shift result of $^{13}\text{C}\alpha$. Missing chemical shifts correspond to unassigned residues (mostly prolines).

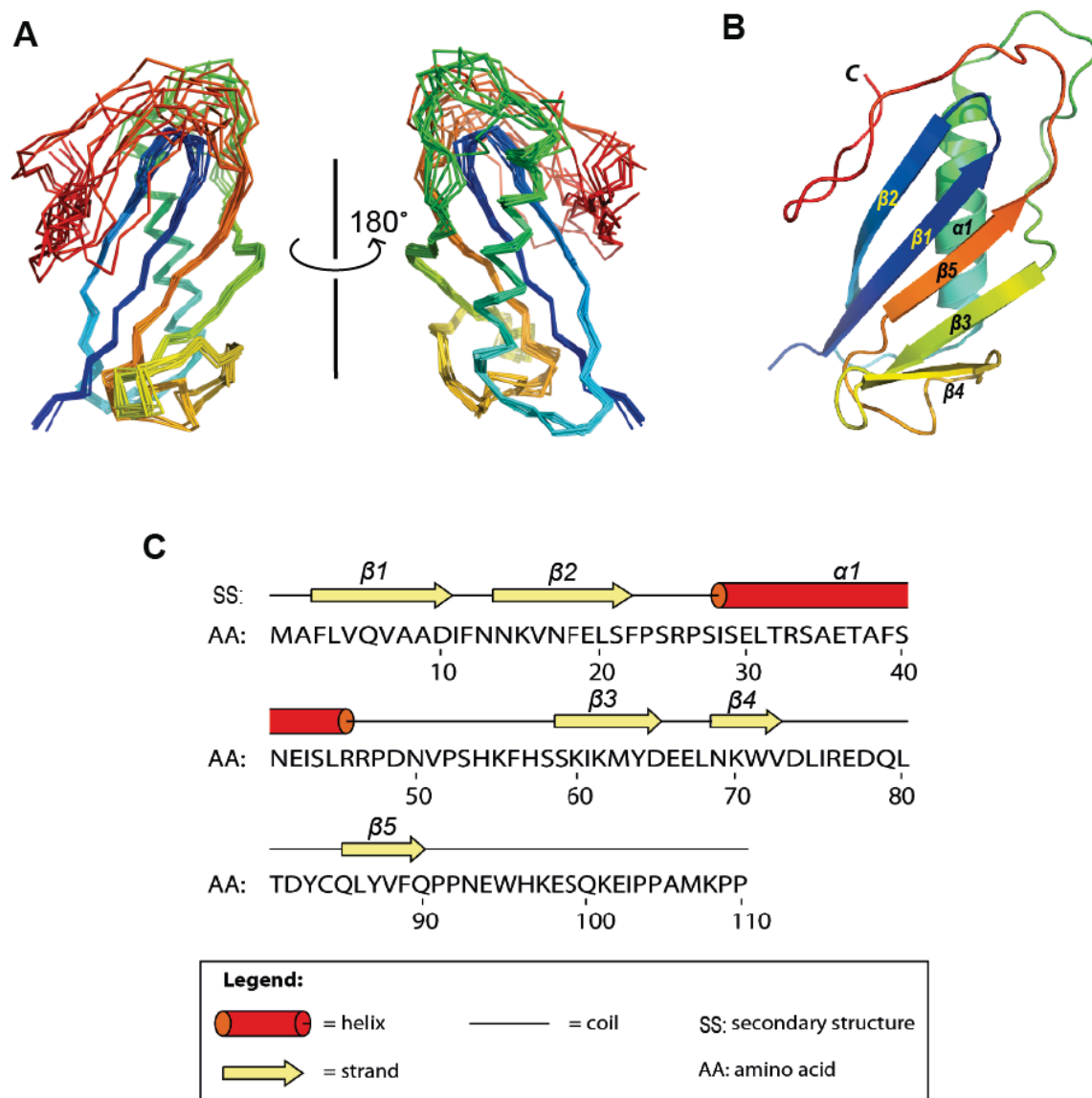


Figure 15 NMR structure of the TbBILBO1-NTD.

(A) Two views of superimposed 10 energy-minimized NMR conformers of the TbBILBO1-NTD. (B) Ribbon diagram of the TbBILBO1-NTD structure, color-ramped from blue at the N-terminus to red at the C-terminus. The five β strands ($\beta 1 - \beta 5$) and the single α helix ($\alpha 1$) are labeled. (C) Diagram showing the secondary structure elements of the TbBILBO1-NTD aligned on its primary sequence.

Table 1 Summary of conformationally restricting experimental constraints ^a

NOE-based distance constraints			
total	859		
intra-residue [i = j]	111		
sequential [i - j = 1]	341		
medium range [1 < i - j < 5]	151		
long range [i - j ≥ 5]	256		
NOE constraints per restrained residue ^b	8.2		
Hydrogen bond constraints			
total	86		
long range [i - j ≥ 5]	51		
Dihedral-angle constraints	140		
Total number of restraints ^b	1085		
Total number of restraints per restrained residue ^b	10.3		
Restricting long-range constraints per restrained residue ^b	2.9		
Total structures computed / selected	500 / 21		
Residual constraint violations ^{a,c}			
Distance violations per structure (> 1 Å)	25		
RMS of distance violation per constraint	0.409 Å		
Maximum distance violation ^d	2.8 Å		
Dihedral angle violations per structure (> 10°)	0		
RMS of dihedral angle violation per constraint	0.868 °		
Maximum dihedral angle violation ^d	3.2 °		
RMSD Values	all	ordered ^e	selected ^f
all backbone atoms	1.9 Å	1.3 Å	1.3 Å
all heavy atoms	2.6 Å	1.8 Å	1.8 Å
Structure Quality Factors - overall statistics	mean score	SD	Z-score ^g
Procheck G-factor ^e (phi / psi only)	-0.22	N/A	-0.55
Procheck G-factor ^e (all dihedral angles)	-0.45	N/A	-2.66
Verify3D	0.13	0.0374	-5.3
MolProbity clashscore	2.18	1.2211	1.15
Ramachandran Plot Summary from Procheck ^f			
Most favoured regions	94.10%		
Additionally allowed regions	4.10%		
Generously allowed regions	1.70%		
Disallowed regions	0.00%		

^a Analysed for the TbBILBO1-NTD (residues 1 to 110)^b There are 105 out of 110 residues with conformationally restricting constraints^c Using average r⁻⁶ averaging^d Largest constraint violation among all the reported structures^e Residues with sum of phi and psi order parameters > 1.8

/Ordered residue ranges: 2A-10D,13N-23P,27I-45L,55K-72V,74L-76R,78D-80L,84C-91P,97K-99S,104P-108K/

^f Residues selected based on: Dihedral angle order parameter, with S(phi)+S(psi) ≥ 1.8

/Selected residue ranges: 2A-10D,13N-23P,27I-45L,55K-72V,74L-76R,78D-80L,84C-91P,97K-99S,104P-108K/

^g With respect to mean and standard deviation for a set of 252 X-ray structures < 500 residues, of resolution ≤ 1.80 Å, R-factor ≤ 0.25 and R-free ≤ 0.28; a positive value indicates a 'better' score

The solved NMR structure further allowed a search using the 3D structure-based protein comparison program DaliLite v3 (Holm and Rosenstrom 2010). The top hit of the searches was the PB1 domain of Par6, which has a ubiquitin-like fold. The root mean square deviation was 2.4 Å ($Z = 5.2$) for backbone atoms in the 70 aligned residues, suggesting a high similarity between the two structures (Figure 16A). Although the topological arrangement of the five-stranded β -sheet and the α helix in the two structures is very similar, $\beta 1$, $\beta 2$ and $\alpha 1$ are all significantly longer in the TbBILBO1-NTD, leading to a more elongated structure for the TbBILBO1-NTD as a whole (Figure 16B).

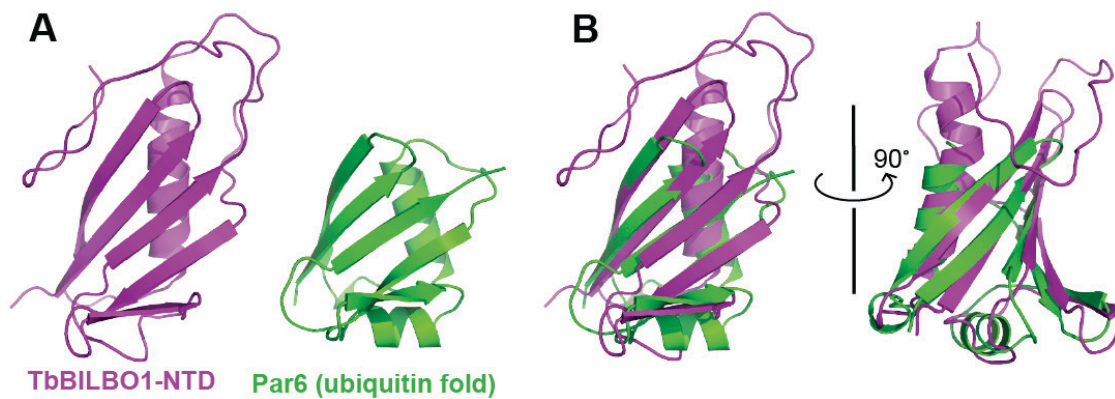


Figure 16 The TbBILBO1-NTD has a ubiquitin-like fold.

(A) Structural comparison between the TbBILBO1-NTD and the ubiquitin-like fold of Par6 (1WMH.pdb).
 (B) Two different views of the TbBILBO1-NTD structure superimposed on Par6.

6.5 Crystal structure of the TbBILBO1-NTD

The NMR structure of the N-terminal domain of TbBILBO1 provides a high-resolution view of the protein. However, the C-terminal tail of the NTD is very flexible, which can attribute to either the intrinsic dynamic nature of the tail or the unavailable assignments of the prolines in this region. Therefore, we tried to solve the structure of the TbBILBO1-NTD by X-ray crystallography using a longer protein construct. The TbBILBO1-NTD+EFh was cloned into the custom vector MalpET, which provides an N-terminal MBP-10×His tag (Figure 17A). The protein was successfully overexpressed in *E.coli* BL21 (DE3).

Initial affinity purification was carried out on a Ni-HiTrap column. After elution by imidazole, the TEV protease was added to the eluted fraction to cut off the MBP-10×His tag. After dialysis to remove excessive imidazole, a second Ni-HiTrap affinity purification was performed to remove the cleaved MBP-10×His tag. Since there is a thrombin cleavage site in the linker region between the two domains, thrombin was subsequently added to the Ni-HiTrap flow-through to separate the NTD and the EFh. Due to the different isoelectric points of the NTD (pI = 7.94) and EFh (pI = 4.7), the sample was then applied to an anion exchange HiTrap QFF column for further purification. The NTD fractions were concentrated and further purified on a Superdex-200 16/60 column. After SEC, two major bands of protein were observed by SDS-PAGE with molecular weights of 18 and 13 kDa with the latter likely being the degradation product (Figure 17B, lane 1). The protein was concentrated to approximately 20 mg/ml and used for crystallization.

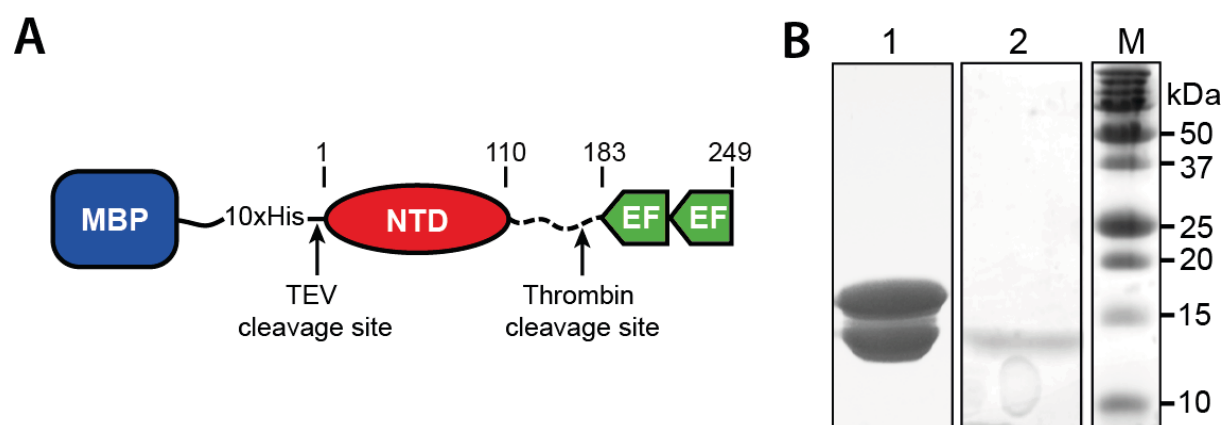


Figure 17 Cloning strategy and SDS-PAGE of purified/crystallized TbBILB01-NTD.

(A) Schematic depicting the construct used for protein expression. MBP: maltose binding protein. (B) SDS-PAGE of protein used for crystallization (lane 1) and the band of washed crystals (lane 2). M, molecular weight marker.

An initial crystallization hit was obtained from the JBScreen Classic 1-4 screen. Our attempt to reproduce crystals manually in this condition did not succeed. The crystallization could be repeated only by micro-seeding. We tried but could not solve the structure by the molecular replacement method. Therefore, we resorted to the single-wavelength anomalous dispersion (SAD) method using SeMet-substituted crystals (Karle 1980). Crystallization of SeMet-substituted protein was carried out by micro-seeding using crashed native protein crystals as the seeds. Plate-shaped crystals with dimensions of $0.2 \times 0.1 \times 0.02$ mm were obtained after two days (Figure 18). When the

crystals were subjected to SDS-PAGE analysis, only a single band at approximately 13 kDa was observed, which corresponded to the lower band of the protein sample used for crystallization (Figure 17B, lane 2).

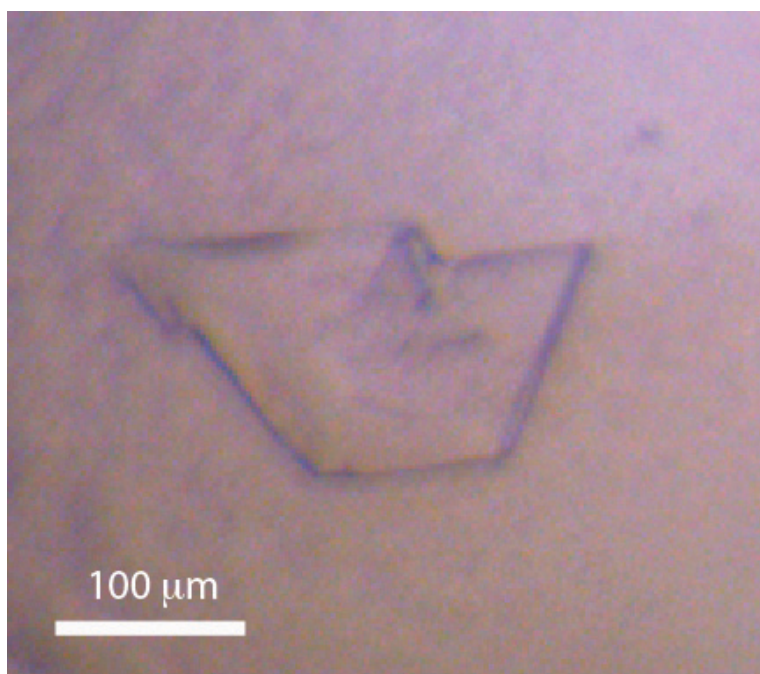


Figure 18 A typical crystal of the TbBILB01-NTD.

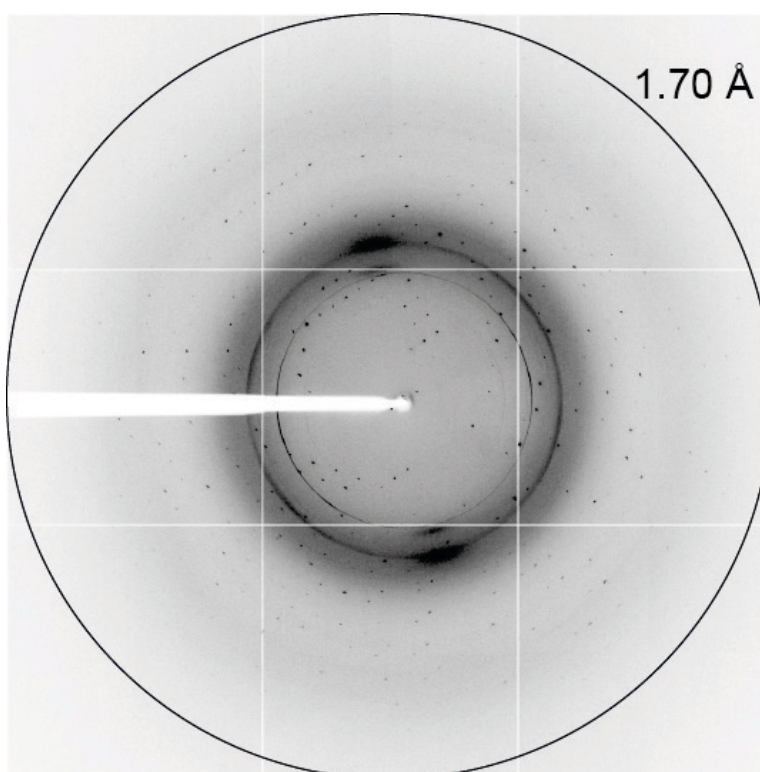


Figure 19 X-ray diffraction image of the TbBILB01-NTD crystal.

X-ray diffraction data were collected on the beamline ID14-4 at the ESRF. The crystal diffracted X-rays to a maximal resolution of approximately 1.6 Å (Figure 19). The crystal belonged to space group $P2_1$ with unit-cell parameters $a = 29.69$ Å, $b = 50.80$ Å, $c = 37.22$ Å, and $\beta = 94.61^\circ$. The Matthews coefficient of 1.88 Å³ Da⁻¹ and the solvent content of 34.48% (Matthews, 1968) suggested that there is probably one molecule in the asymmetric unit. Data collection and refinement statistics are shown in Table 2.

Table 2 X-ray data collection and refinement statistic of TbBILBO1-NTD

Data collection	
Space group	$P2_1$
Cell dimensions	
a, b, c (Å)	29.69 50.80 37.22
β (°)	94.61
Resolution (Å)	37.1-1.69 (1.78-1.69)*
No. Of observed reflections	98,166 (13,228)
No. of unique reflections	12,398 (1,744)
R_{merge}^\dagger	0.099(0.972)
$I / \sigma I$	12.7 (2.1)
Completeness (%)	99.7 (97.9)
Redundancy	7.9 (7.6)
Refinement	
Resolution (Å)	20-1.60
R_{work} / R_{free} (%)	0.169/0.198
No. atoms	
Protein	981
Waters	135
R.m.s. deviations	
Bond lengths (Å)	0.008
Bond angles (°)	1.17

*Values in parentheses are for the highest resolution shell.

$^\dagger R_{merge} = \sum_{hkl} \sum_i |I_i(hkl) - \langle I(hkl) \rangle| / \sum_{hkl} \sum_i I_i(hkl)$, where $I_i(hkl)$ is the i^{th} observation of reflection hkl and $\langle I_i(hkl) \rangle$ is the weighted average intensity for all observations of reflection hkl .

The structure of the TbBILBO1-NTD was solved by the SAD method using AutoSol and refinement was carried out using phenix.refine (both are part of the PHENIX program suite). Because of the high resolution (1.6 Å), the electron density of each residue could be easily resolved and the model could be unambiguously built. Figure 20A shows that even the aromatic rings of phenylalanine, tryptophan, histidine and tyrosine could be easily distinguished. The thrombin cleavage site in the linker region between the NTD and EFh is located at residue R175, which makes the NTD consist of 175 residues. However, the solved structure showed that the NTD only has 115 residues, which means

that either thrombin can also cleave the linker region at position R115 or residues after R115 is disordered. Given that protein in the crystals had a lower molecular weight (~13kDa) than expected (~18kDa) (Figure 17, compare lanes 1 and 2), the variable linker region (residues 116-175) was likely degraded during the incubation time of crystallization. The structure of the NTD solved by X-ray crystallography has a ubiquitin-like fold, similar to the NMR structure (Figure 20B, C). However, the C-terminal tail of the X-ray structure is much better defined, twisting in front of $\beta 1$, $\beta 2$ and the N-terminus of $\alpha 1$ to form a crescent-like structure (Figure 20B). Therefore the flexibility of the C-terminal tail in the NMR structure is likely due to the absence of most of the NOE restraints in this region; there are six prolines in this region which could not be assigned in the 2D ^1H - ^{15}N HSQC spectrum (Figure 15C).

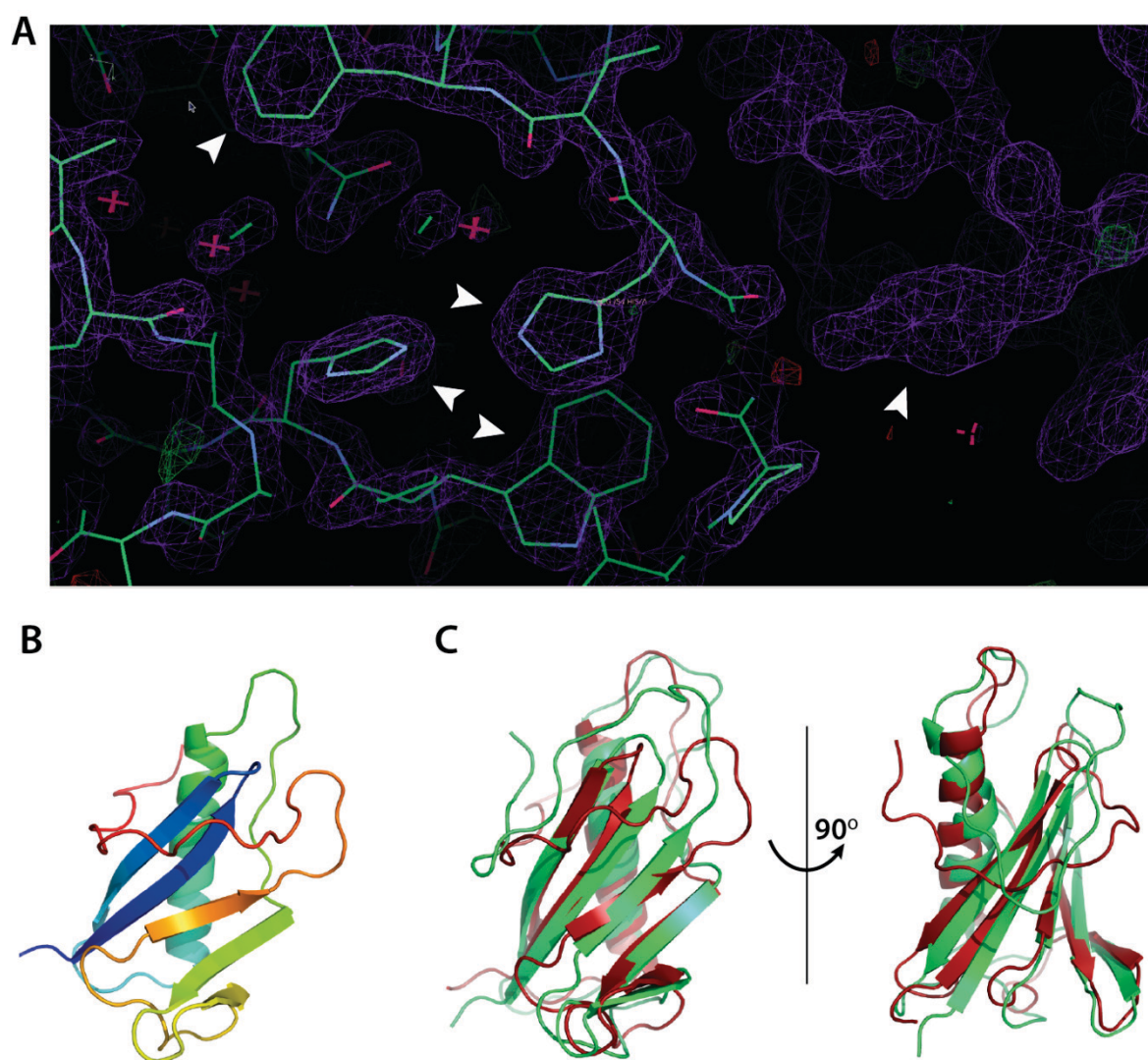


Figure 20 Crystal structure of the TbBILBO1-NTD.

(A) The $2F_o - F_c$ electron density map of the TbBILBO1-NTD SeMet crystal. Arrowheads show the aromatic ring of phenylalanine, tryptophan and histidine in the refined model. A tyrosine residue of a neighboring molecule in the crystal is also indicated (right). (B) Ribbon diagram of the crystal structure of the TbBILBO1-NTD. The structure is color-ramped from blue at the N-terminus to red at the C-terminus. (C) Two different views of the TbBILBO1-NTD crystal structure (red) superimposed on the NMR structure (green).

6.6 The NTD has a conserved surface patch essential for TbBILBO1 function

Mapping the primary sequence alignments (Figure 6) onto the 3D structure of the NTD revealed the presence of an extensive conserved patch. This patch is on the solvent-exposed side of the β -sheet and contains four aromatic residues (F12, W71, Y87 and F89) and three basic ones (K15, K60 and K62) (Figure 21A). These residues together generate a crater-like structure on an otherwise flat surface, with three of the four aromatic residues (W71, Y87 and F89) lying at the bottom of the crater and four other conserved residues forming the surrounding rim (Figure 21B). To find out whether this surface patch is essential for the function of the TbBILBO1-NTD, two site-directed mutagenesis constructs were derived from TbBILBO1-FL (Figure 21C). Mut1 (F12A, K15A, K60A and K62A) substitutes the "rim" residues with alanines; Mut2 (W71A, Y87A and F89A) substitutes the aromatic "bottom" residues with alanines.

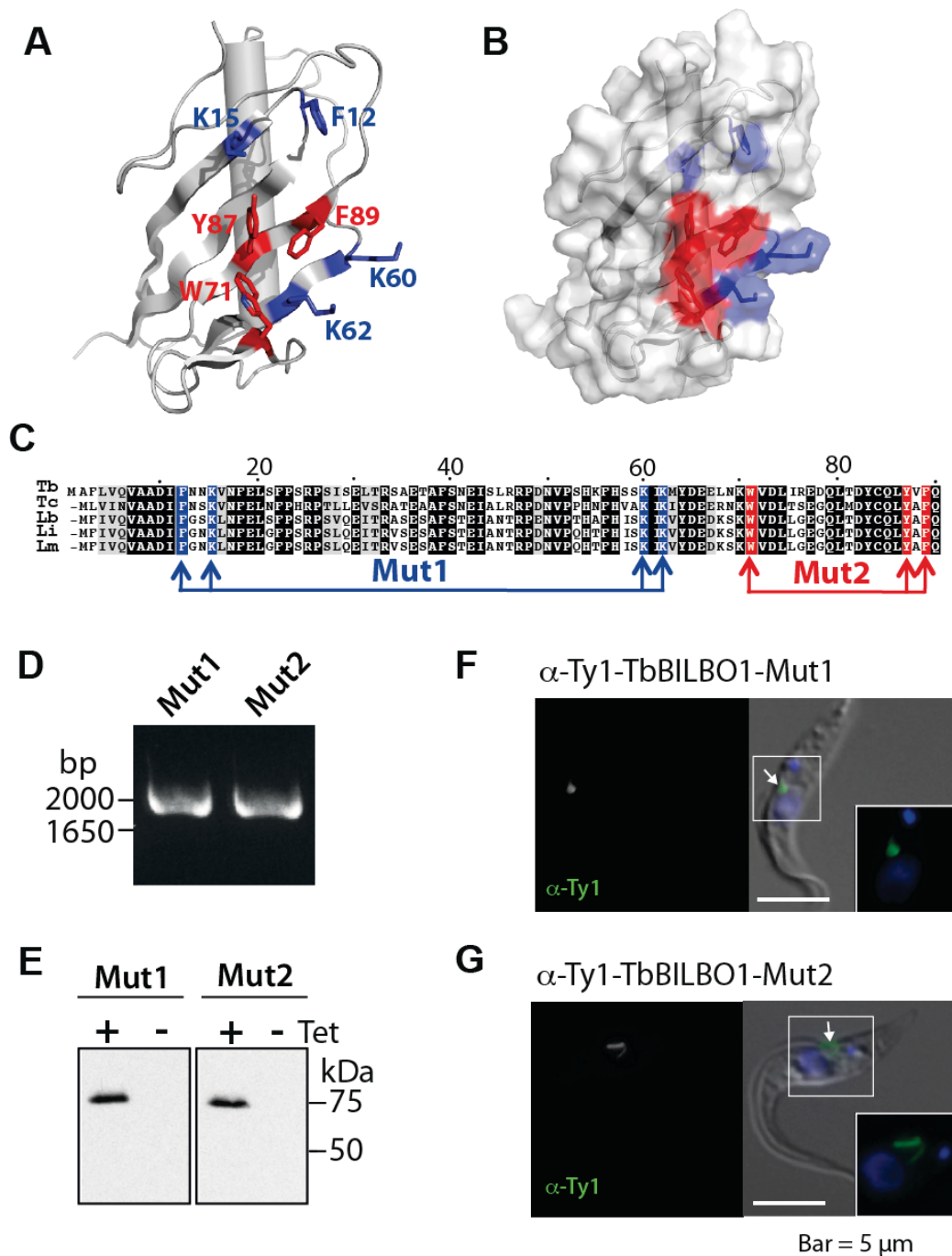


Figure 21 A conserved surface patch on the TbBILBO1-NTD.

(A) Ribbon diagram of the TbBILBO1-NTD with the seven conserved residues shown as sticks. The three aromatic residues at the bottom of the conserved crater are colored in red; the four flanking residues at the rim are shown in blue. (B) Surface plot with the same orientation and color scheme as in (A). (C) Primary sequence alignment of the NTDs of TbBILBO1 and homologs. Residues altered by site-directed mutagenesis in the Mut1 ("rim" residues) and Mut2 ("bottom" residues) constructs are indicated. (D) PCR amplification of genomic DNA from putative clones confirmed the presence of the indicated TbBILBO1 transgenes. Primers annealing to sequences encoding the Ty1 epitope tag (5' end) and ORF (3' end) were used. (E) Immunoblots of whole-cell lysates from cells inducibly expressing the indicated Ty1-tagged TbBILBO1 transgenes in the presence or absence of 20 ng/ml tetracycline. Probing with anti-Ty1 antibodies confirmed that both transgenes were inducibly and tightly expressed. (F & G) Ty1-tagged TbBILBO1-FL and -NTD constructs localized correctly to the FPC. Arrows indicate the point of flagellum entry into the cell. Boxed areas are enlarged in insets.

Stable cell lines inducibly expressing the respective mutagenized constructs with N-terminal Ty1 epitope tags were generated. As before, integration of the transgene into the genomic DNA was confirmed by PCR, and tight and inducible expression verified by immunoblotting with anti-Ty1 antibodies (Figure 21D, E). Correct localization of the two mutagenesis constructs was confirmed by immunofluorescence using anti-Ty1 antibodies (Figure 21F, G). The effects of overexpression of the two mutagenesis constructs were then compared to that of overexpressed Ty1-TbBILBO1-FL and Ty1-TbBILBO1- Δ NTD. Remarkably, both mutagenesis constructs recapitulated the level of growth inhibition seen upon deletion of the entire NTD (Figure 22A). The tetracycline concentrations required to reduce cell growth by 50% (IC_{50}) for Ty1-TbBILBO1- Δ NTD, -Mut1, and -Mut2 were calculated to be 4.5, 6.3 and 5.8 ng/ml, respectively. This is over one order of magnitude lower than the value calculated for Ty1-TbBILBO1-FL (77.9 ng/ml). This suggested that the seven residues comprising the conserved surface patch were essential for the NTD function.

To observe the effect of the NTD deletion and the two mutations *in vivo*, cells overexpressing these Ty1-tagged TbBILBO1 constructs were analyzed by immunofluorescence microscopy. In dividing cells, Ty1-TbBILBO1-FL was associated with both the old and new flagellum (Figure 22B, arrows). Interestingly, cells overexpressing Ty1-TbBILBO1- Δ NTD, -Mut1, and -Mut2 all exhibited detached new flagella at the posterior end of the cell (Figure 22C-E, arrowheads). The new kinetoplast was near this new flagellum, but Ty1-TbBILBO1- Δ NTD, -Mut1, and -Mut2 labeling was associated only with the old but not the new flagellum (Figure 22C-E, arrows). Approximately equivalent expression levels of the four constructs at each tetracycline concentration used for induction were verified by immunoblotting (Figure 22H). A gallery of images showing the phenotypic effects of overexpression of the four TbBILBO1 constructs is provided (Figure 23A-D). The TbBILBO1-Mut2 construct was consistently found to form thread-like morphologies, while the others exhibited a more canonical punctate morphology (Figure 23D).

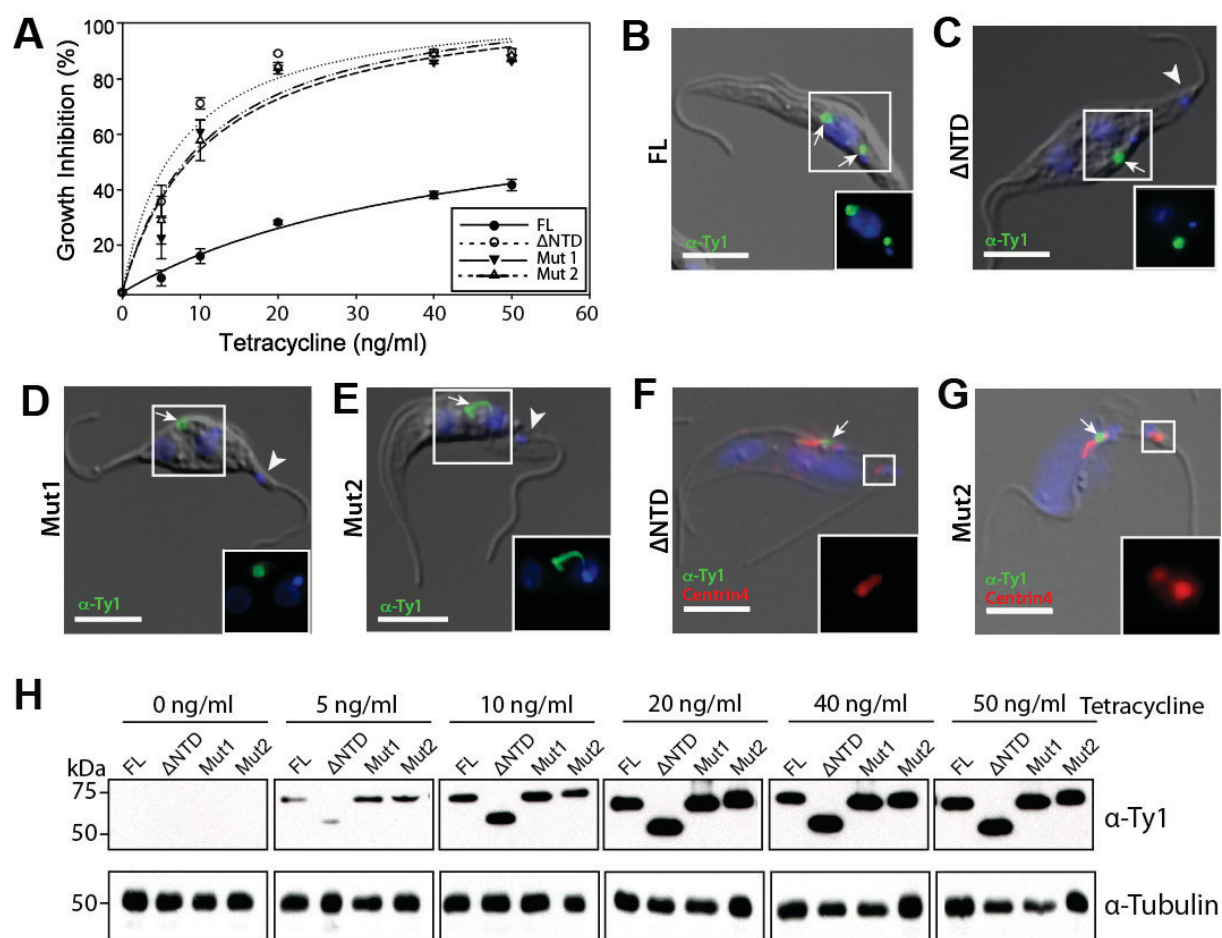


Figure 22 A conserved surface patch on the TbBILBO1-NTD is essential for the function of the protein *in vivo*.

(A) Mutagenesis of the TbBILBO1-NTD causes cell growth inhibition. Growth inhibition curves from stably-transfected cells inducibly expressing Ty1-tagged TbBILBO1 constructs at different concentrations of tetracycline after four days of induction. (B-E) TbBILBO1 NTD deletion or mutations causes dominant negative effects. Cells conditionally overexpressing the indicated constructs with an N-terminal Ty1 tag were analyzed after four days of induction by immunofluorescence microscopy. Anti-Ty1 antibodies were used to label the cells. Arrows indicate the position of correctly localized TbBILBO1 constructs. Arrowheads indicate the kinetoplast at the base of the detached flagellum. Note the absence of TbBILBO1 labeling at the detached flagella. (F & G) Immunofluorescence assay of cells overexpressing the indicated constructs after four days of induction. Detergent-extracted cells were co-labeled with Anti-Ty1 and Anti-TbCentrin4 antibodies. The detached flagella are associated with a TbCentrin4-positive basal body (insets). DAPI was used to stain DNA (blue). Scale bars, 5 μ m. (H) Immunoblots of whole-cell lysates from the four cell lines taken at various concentrations of tetracycline and probed using anti-Ty1 antibodies (upper panels). The expression of all four constructs was approximately the same at each tetracycline concentration, and saturated at around 20 ng/ml. Immunoblotting with anti-tubulin antibodies was used as a loading control (lower panels).

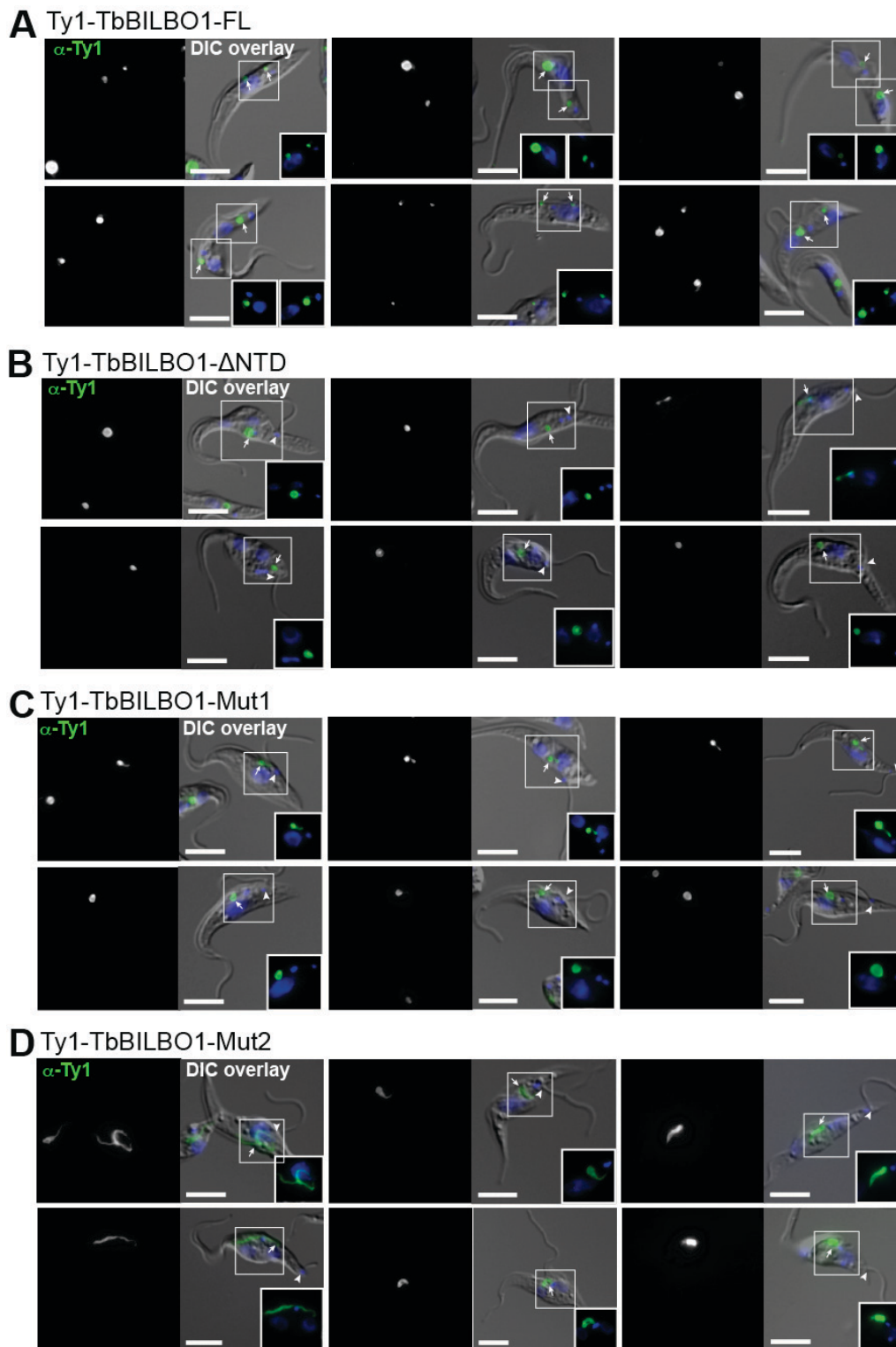


Figure 23 Overexpression of different Ty1-tagged TbBILBO1 constructs *in vivo*.

All cells were assayed by immunofluorescence microscopy after a two-day induction using 20 ng/ml tetracycline. Cells were labeled using anti-Ty1 antibodies; DAPI was used to stain DNA (blue). Boxed regions are enlarged in insets. (A) Ty1-TbBILBO1-FL did not cause significant morphological abnormalities. In replicating cells, Ty1-TbBILBO1-FL was associated with both old and new flagella. (B-D) Overexpression of Ty1-TbBILBO1-NTD, -Mut1, and -Mut2 caused gross morphological effects, notably a detached new flagellum in replicating cells. No TbBILBO1 signal was associated with the new flagellum in replicating cells. Scale bars, 5 μ m.

These morphological alterations of the cells overexpressing Ty1-TbBILBO1- Δ NTD/Mut1/Mut2 were strikingly similar to those described upon depletion of TbBILBO1 by RNAi. In TbBILBO1 RNAi cells, a feature associated with the detached posterior flagellum is the presence of the nucleating basal body at the plasma membrane (Bonhivers, Nowacki et al. 2008). To analyze whether the detached flagella were proximally associated with a basal body, the cells were co-labeled with TbCentrin4. In duplicating cells overexpressing Ty1-TbBILBO1-FL, TbCentrin4-labeled basal bodies were observed at the base of both old and new flagella (Figure 24A). Similarly, in duplicating cells overexpressing Ty1-TbBILBO1- Δ NTD, -Mut1 and -Mut2, TbCentrin4-labeled basal bodies were observed at the base of both the old and the detached new flagellum (Figure 22F, G; Figure 24B-D). No TbCentrin4-labeled bilobe structure was observed in the vicinity of the detached new flagellum (Figure 24B-D). This indicated that overexpression of Ty1-TbBILBO1- Δ NTD, -Mut1, and -Mut2 generated a dominant negative effect, with several aspects appearing to recapitulate the RNAi phenotype (Bonhivers, Nowacki et al. 2008).

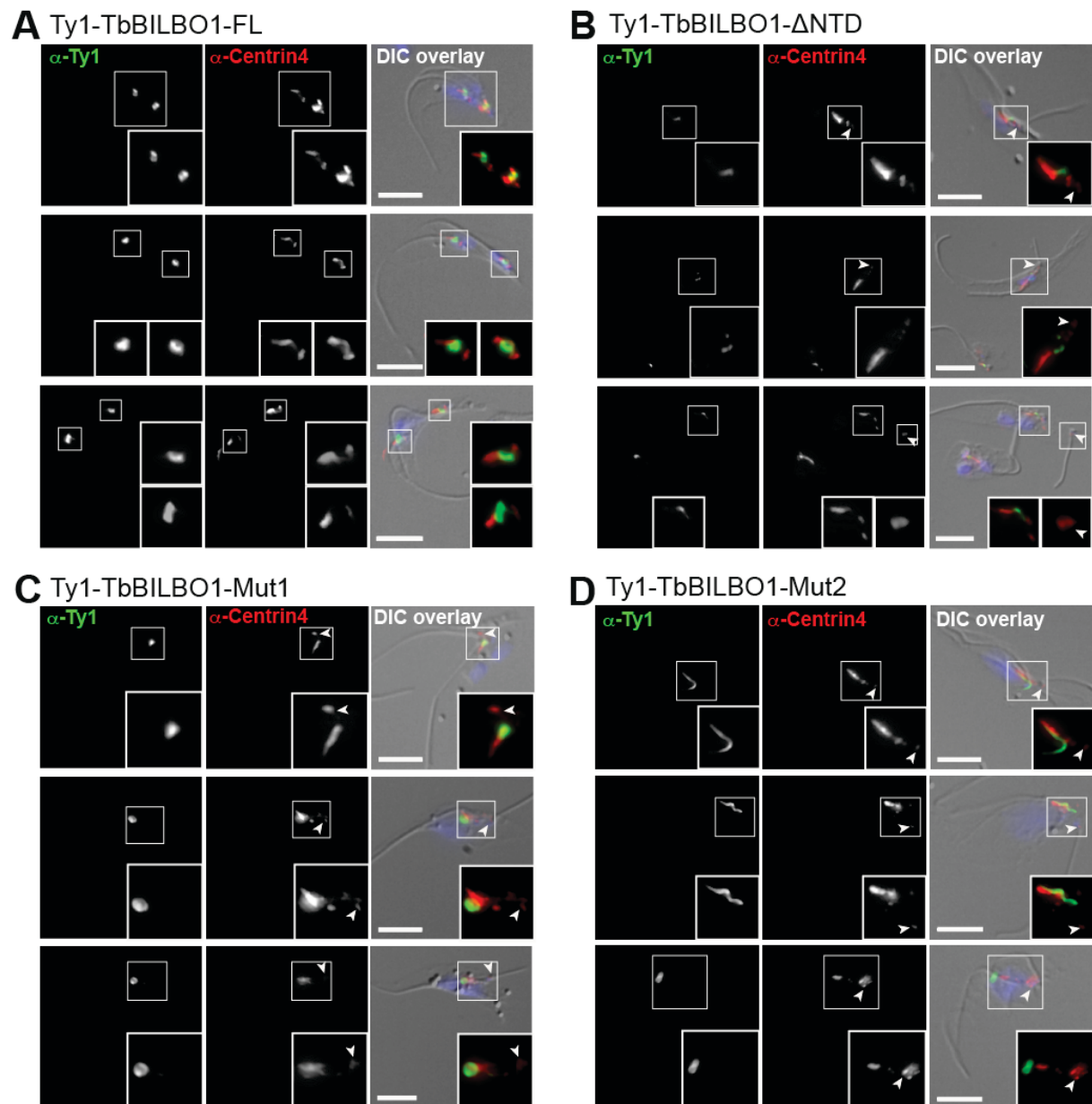


Figure 24 The detached flagellum in overexpressing cells has an associated basal body.

Expression of the various Ty1-tagged TbBILBO1 constructs was induced for two days using 20 ng/ml tetracycline. Detergent-extracted cells were labeled with anti-Ty1 and anti-TbCentrin4 antibodies. DAPI was used to stain DNA (blue). Boxed areas are enlarged in insets. (A) In replicating cells overexpressing Ty1-TbBILBO1-FL, both Ty1-TbBILBO1-FL and TbCentrin4 had normal localizations and were associated with both the old and new flagellum. (B-D) The detached new flagella in replicating cells overexpressing the other TbBILBO1 constructs are associated with basal bodies (arrowheads). Scale bars, 5 μ m.

6.7 Impaired TbBILBO1 function is lethal

Deletion or mutagenesis of the TbBILBO1-NTD was sufficient to cause inhibition of cell growth (Figure 22A), but it was not clear whether this was due to cell cycle arrest or cell death. To test this, a propidium iodide/Annexin V viability assay was performed. Propidium iodide is a membrane-impermeant DNA dye and a high signal indicates compromised cell viability; Annexin V binds to cells undergoing apoptosis. Overexpression of all four constructs was induced with 20 ng/ml tetracycline for four days, and the cells were then treated with fluorescein isothiocyanate-labeled Annexin V antibodies, stained with propidium iodide, and analyzed by FACS (Figure 25A).

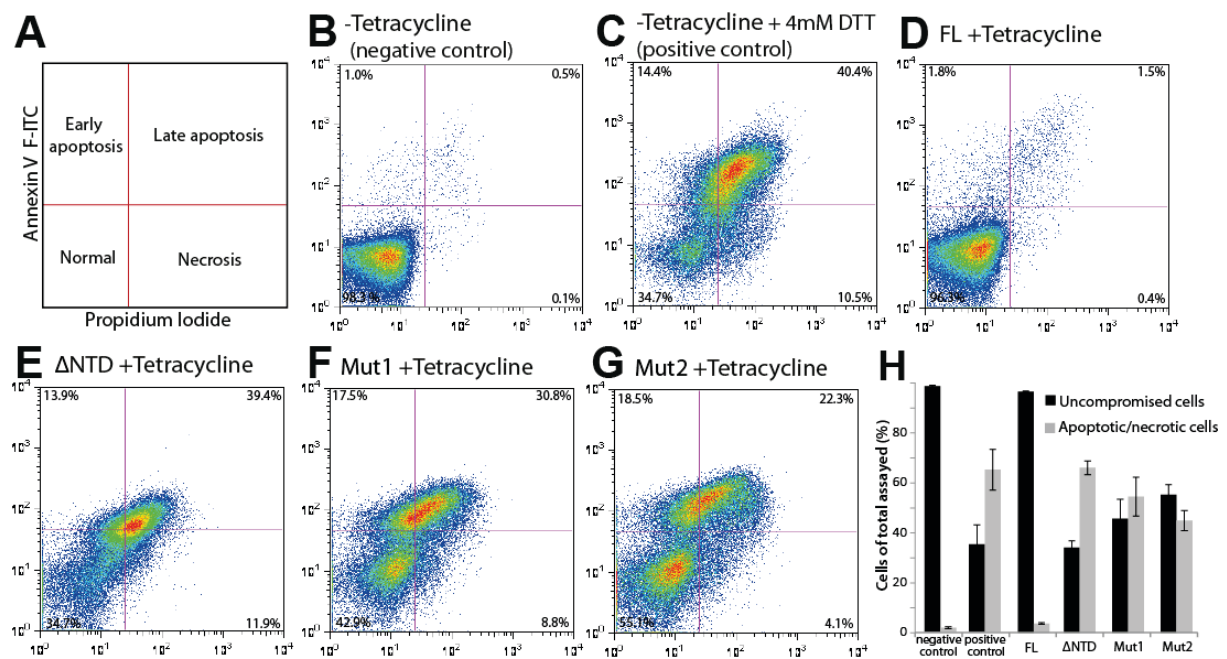


Figure 25 Overexpression of TbBILBO1-NTD deletion or mutation constructs causes cell death.

Stably-transfected cells conditionally expressing the indicated constructs were induced using 20 ng/ml tetracycline for four days. They were then treated with fluorescein isothiocyanate-labeled Annexin V antibodies, stained with propidium iodide (PI), and analyzed by FACS. (A) Diagram showing the different cell populations detected by staining with Annexin V and PI. (B) Negative control using uninduced cells. (C) Positive control for programmed cell death using 4mM DTT treatment for 24h. (D-G) FACS traces for cells overexpressing the indicated constructs. (H) Quantitation of the data shown in B-G. Values shown are the mean from three independent experiments. Bars show standard errors.

In the absence of tetracycline, most of the cells were viable with the majority of the population giving a low signal in each channel (Figure 25B). As a positive control for cell death, wild-type *T. brucei* cells were cultured in the presence of 4 mM DTT for 24h. DTT causes ER stress and induces a spliced leader RNA silencing pathway leading to

apoptosis. This stress response cannot be recovered even after DTT removal (Goldshmidt, Matas et al. 2010). Under these conditions, few cells were viable with most of the population undergoing apoptosis/necrosis (Figure 25C). Overexpression of Ty1-TbBILBO1-FL did not significantly affect the viability of the cells, similar to the negative control (Figure 25D). Conversely, overexpression of Ty1-TbBILBO1- Δ NTD, -Mut1, and -Mut2 showed that many of the cells in the population were undergoing apoptosis or necrosis (Figure 25E-G). Quantification of the results confirmed that deletion of the TbBILBO1-NTD had the most severe effect on cell viability, with only 34.7% viable cells compared to Ty1-TbBILBO1-Mut1 (42.9%) and -Mut2 (55.1%). In contrast, 96.3% cells overexpressing Ty1-TbBILBO1-FL were viable (Figure 25H). Therefore, the dominant negative effects seen upon overexpression of Ty1-TbBILBO1- Δ NTD, -Mut1, and -Mut2 lead to cell death.

6.8 Discussion

A detailed analysis of the TbBILBO1 primary structure revealed the presence of an LZ at the extreme C-terminus (Figure 6). Transient expression of TbBILBO1 truncation constructs *in vivo* demonstrated that this LZ is necessary but not sufficient for correct targeting of TbBILBO1 to the FPC (Figure 11). Conversely, deletion of the NTD had no effect on targeting. This non-requirement for correct localization implied that the NTD could have a functional role. Consistent with this hypothesis, the inducible overexpression of a TbBILBO1 construct lacking the NTD produced a dominant negative effect, and completely inhibited cell growth in a dose-dependent manner (Figure 12). The structure of the NTD was solved by NMR and latterly by X-ray crystallography, and revealed a ubiquitin-like fold. Importantly, the structural model revealed the presence of a conserved surface patch consisting of four aromatic and three basic residues that together form a crater-like structure (Figure 21). Site-directed mutagenesis on the residues comprising either the rim or bottom of the crater was sufficient to recapitulate the growth inhibition caused by deletion of the entire NTD when these constructs were overexpressed *in vivo* (Figure 22). Cells that were overexpressing constructs either lacking the NTD or carrying the mutant versions produced morphological phenotypes

that were consistent with published TbBILBO1 RNAi data (Bonhivers, Nowacki et al. 2008). FACS analysis on cells overexpressing the TbBILBO1 NTD deletion/mutant constructs confirmed that the effect was lethal, with an abundant production of necrotic cells (Figure 25). It was concluded that the NTD of TbBILBO1 was essential for its function *in vivo*.

It should be noted that the precise function of TbBILBO1 remains unclear. Based on published RNAi data (Bonhivers, Nowacki et al. 2008) and the dominant negative overexpression data provided here, it is clearly involved in FP and FPC biogenesis, but its role in interphase cells is undetermined. Whatever that function is, the data provided here suggest that the NTD could possibly provide it. Inter-domain pull-downs revealed that the NTD does not interact directly with other parts of TbBILBO1 (data not shown). It is therefore possible that the conserved surface patch on the NTD may be the binding site for either an unknown essential component of the FPC or a key regulatory protein (Figure 32B, hexagons in the inset). Mutations disrupting their interaction might therefore have a catastrophic impact on the integrity and/or function of the FPC, leading to the same phenotype as the NTD deletion (Figure 12).

The data provided here not only corroborate these statements but also extend the conclusions to single-residue resolution. The fact that mutations of the aromatic and basic residues arranged in a surface patch on the NTD were sufficient to recapitulate the effect of deleting the entire domain strongly suggests that this is a key functional region of the molecule (Figure 22). As such, this specific region represents a good candidate for pharmacological blockade. Given that orthologs of TbBILBO1 with high sequence conservation are present in other pathogenic trypanosomatids, and that no orthologs exist in humans, the protein could present an attractive pan-trypanocidal drug target.

One further hypothesis is prompted by the structure of the TbBILBO1-NTD. As noted, the Par6 protein also exhibits a ubiquitin-like domain, and binds atypical protein kinase C (aPKC) (Figure 26B). The structure of this complex has been solved (Hirano, Yoshinaga et al. 2005), allowing superimposition of the TbBILBO1-NTD (Figure 26C). Interestingly, the region of the TbBILBO1-NTD corresponding to the aPKC interacting interface in Par6 is blocked by a C-terminal loop (Figure 26A, C). A testable prediction is that this loop regulates the interaction of TbBILBO1 with other FPC proteins. Notable

also is that the conserved surface patch is distal to this interaction surface (Figure 26D). This could mean either that the patch's function is unrelated to protein-protein interaction, or that TbBILBO1 makes contacts via two separate interfaces. Future work will test these hypotheses in depth.

In summary, this work has provided a structural insight into the NTD of TbBILBO1, the first characterized and only known cytoskeletal protein in the *T. brucei* FPC. The conserved surface patch identified in the TbBILBO1-NTD appears to be essential for the proper function of TbBILBO1 in the parasite and therefore represents an attractive candidate site for therapeutic drug design.

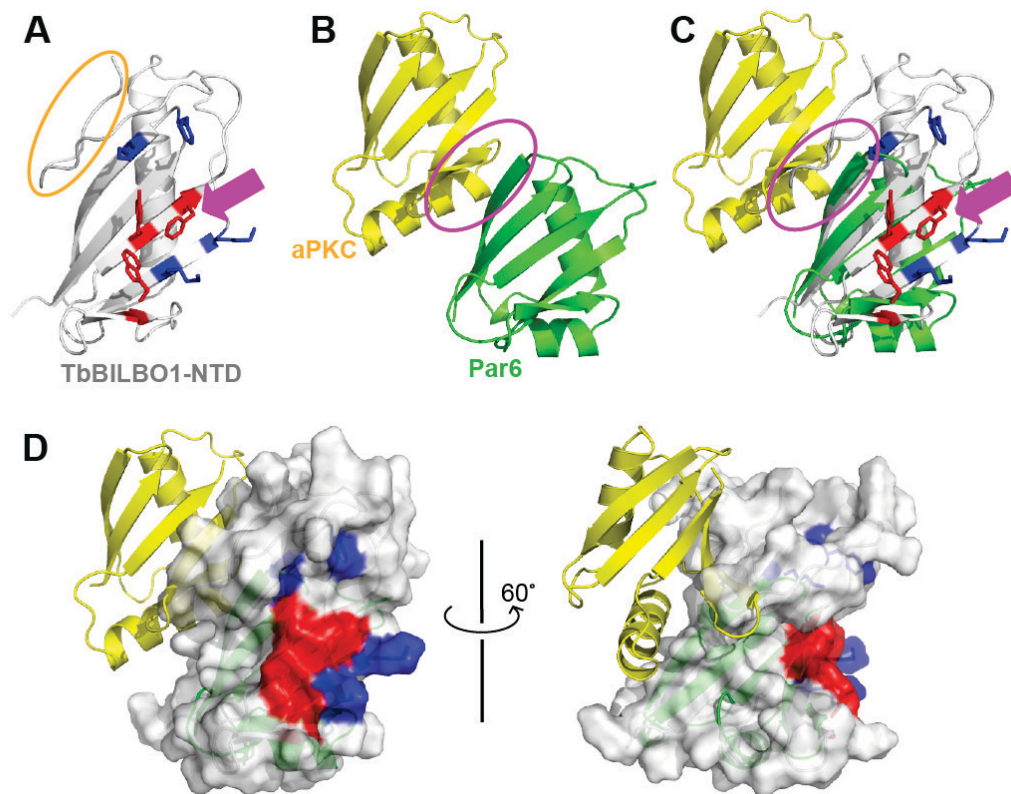


Figure 26 Structural comparison between the TbBILBO1-NTD and Par6 in the Par6-aPKC complex.

(A) Ribbon diagram of the TbBILBO1-NTD NMR structure. Residues in the essential surface patch are shown as red/blue sticks. The magenta arrow indicates the crater-like area mutated in this study. The orange oval encircles the flexible loop at the C-terminus of the NTD. (B) Ribbon diagram of the Par6-aPKC complex (1WMH.pdb). The magenta oval indicates the interaction interface between the two proteins. (C) Superposition of the TbBILBO1-NTD onto Par6 in the Par6-aPKC complex. The C-terminal loop of the TbBILBO1-NTD obscures the surface corresponding to the aPKC binding site in Par6. The conserved surface patch of the TbBILBO1-NTD is also distant from the corresponding aPKC binding site on Par6. (D) Two views of the superimposed structures with the TbBILBO1-NTD shown in surface plot.

7 Oligomerization and assembly mechanisms of TbBILBO1

7.1 Summary

Having determined the structure of the NTD and its essential role *in vivo* (chapter 6), I further investigated other domains of TbBILBO1. It was hypothesized that these domains are important for the assembly of TbBILBO1 at the FPC. In this chapter, we show that full-length TbBILBO1 forms a filament-like structure via both the antiparallel arrangement of the central coiled-coil and an LZ-mediated inter-dimer interaction. This structure further assembles into condensed fibers via lateral association between the filaments.

7.2 The TbBILBO1-CCD forms an antiparallel homodimer

It is necessary to know the structural arrangement of the CCD (aa262-533) in order to find out how TbBILBO1 assembles. This domain represents nearly half of the full-length protein. Using the SLS method, it was found that the CCD in isolation forms a dimer with a molecular weight of 63 kDa (theoretical molecular weight is 62.6 kDa) (Figure 27A). Initial crystallization experiments using the CCD did not yield any crystals that diffracted well, so low-resolution EM methods were instead employed to elucidate the relative orientation of the two helices in the dimer. For these experiments, recombinant TbBILBO1-CCD was expressed with an N-terminal MBP tag. The 42-kDa MBP has a globular structure of ~5 nm in diameter, which is significantly larger than the ~1.5 nm width of a two-stranded coiled coil. If the CCD forms an antiparallel dimer, one would expect to see a dumbbell-like structure with two globules at opposite ends of the coiled-coil rod. Conversely, a parallel dimer would show a hammer-like structure with both MBP moieties spatially close to each other (Figure 27B). Using rotary metal shadowing EM the fusion protein was found to always appear in a dumbbell-like configuration (Figure 27C,D), suggesting that the TbBILBO1-CCD forms an antiparallel dimer.

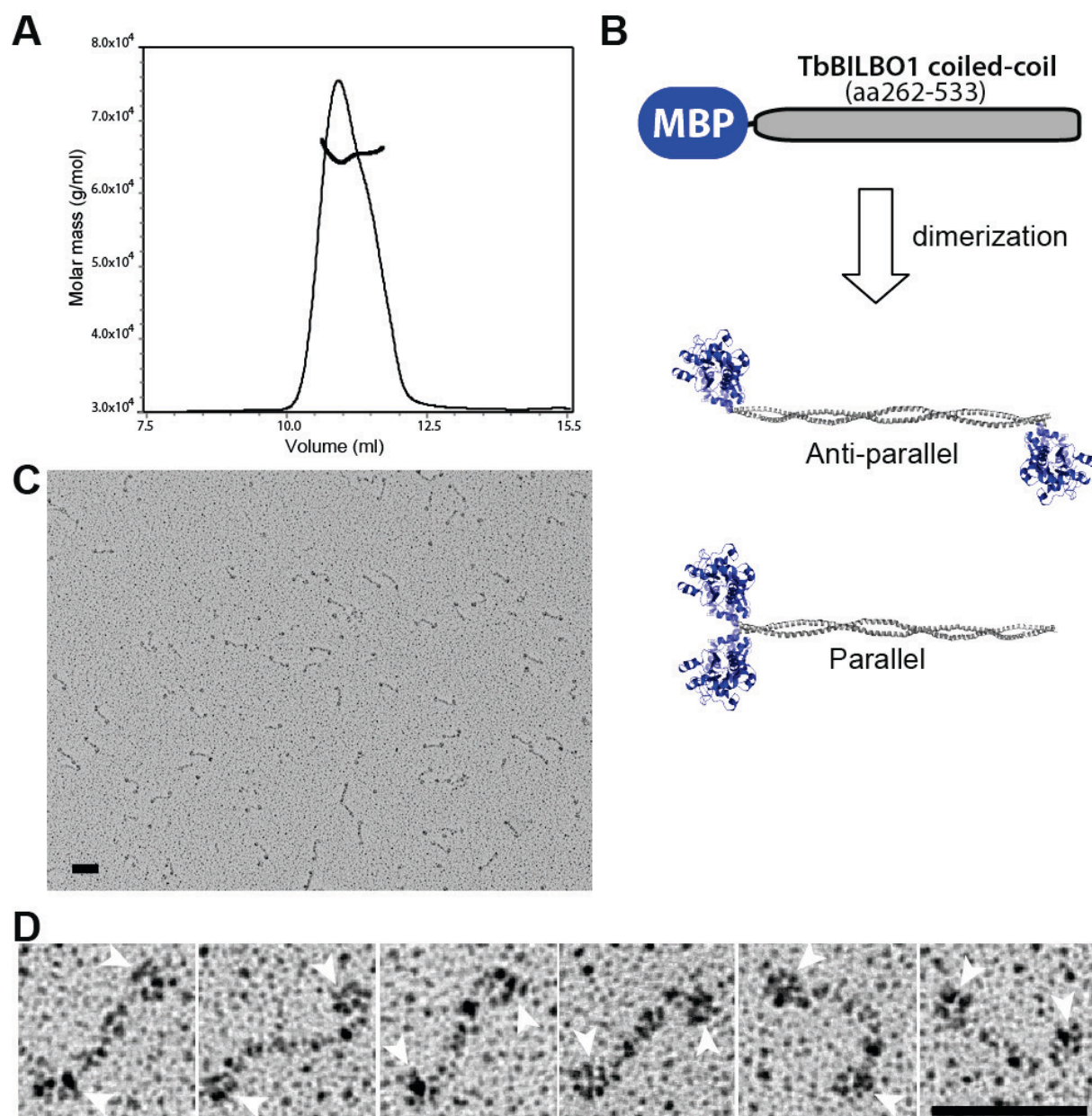


Figure 27 The TbBILBO1-CCD forms an antiparallel dimer.

(A) SLS result of the recombinant TbBILBO1-CCD (aa262-533) showed a molecular weight of 63 kDa, suggesting that it forms a dimer. For this experiment, the MBP tag was removed by the TEV protease. (B) Schematic showing the cloning construct with predicted results. A MBP tag (42 kDa) was added to the N-terminus of the CCD. An antiparallel dimer is expected to form a dumbbell-like structure, whereas a parallel dimer would be hammer-like. (C) Rotary metal shadowing EM image of the MBP-tagged TbBILBO1-CCD. (D) Gallery of images taken from (C). Arrowheads indicate the globular MBP tags. Scale bars, 50 nm.

7.3 The TbBILBO1-LZ mediates oligomerization

Recombinant 6×His-tagged TbBILBO1-FL was expressed in bacteria but no soluble protein could be purified by affinity chromatography (Figure 28, lanes 2-4). To increase the solubility of the protein, a 6×His MBP-tag was fused to the N-terminus of TbBILBO1-FL (Figure 28, lanes 5-7). Soluble fusion protein purified by affinity chromatography was checked by SEC on an FPLC system. Curiously, a large fraction of 6×His-MBP-TbBILBO1-FL failed to pass through the column. The intact protein that did pass through was almost exclusively present in the void volume (V_0) of the column, suggesting that it was either aggregated or formed very large oligomers (Figure 29A, B). Deletion of the EFh domain resulted in more protein being eluted, but the majority remained in V_0 (Figure 29A, C). Interestingly, however, deletion of the C-terminal LZ not only allowed almost all protein to pass through the column but also shifted the elution peak to a position corresponding to the dimeric size of the protein (Figure 29A, D). This implied that the LZ mediates oligomerization of TbBILBO1.

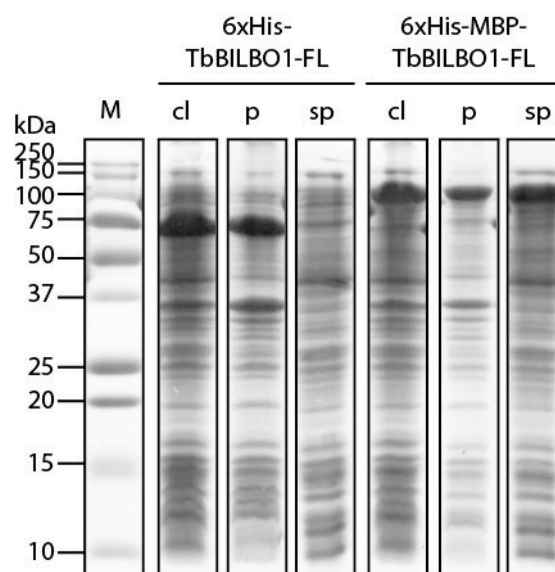


Figure 28 Solubility test of TbBILBO1 with an N-terminal 6×His or 6×His-MBP tag.

Recombinant 6×His-TbBILBO1-FL and 6×His-MBP-TbBILBO1-FL were overexpressed in *E. coli* BL21(DE3). The cells were lysed in an EmulsiFlex-C3 homogenizer and centrifuged to pelleting cell debris. The cells lysate (cl), pellet of cell debris (p) and the supernatant (sp) were then subjected to SDS-PAGE to check the protein overexpression and solubility. The results showed that both proteins are overexpressed but only the recombinant 6×His-MBP-TbBILBO1-FL was soluble.

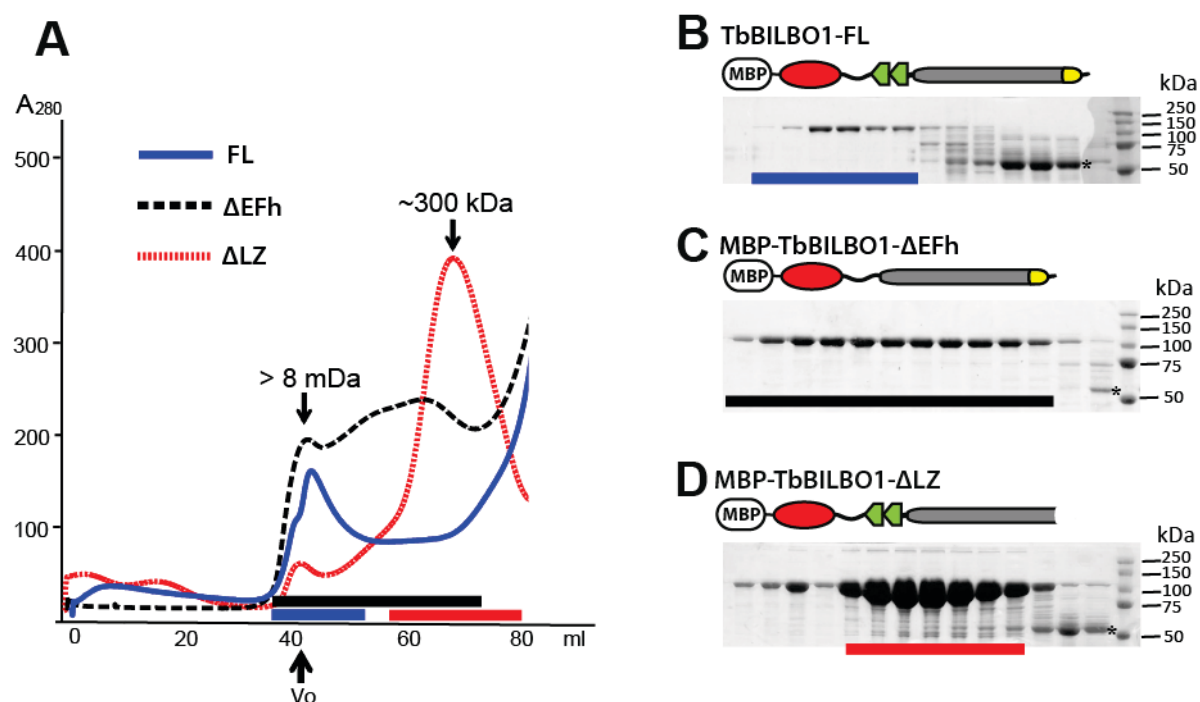


Figure 29 Analysis of TbBILBO1 oligomerization by size exclusion chromatography.

(A) SEC elution profiles (S-400 16/60) of three different constructs of TbBILBO1. The FL protein is predominantly in the void volume (V_0). Note that while deletion of the EFh (Δ EFh) does not significantly alter its elution, removal of the LZ (Δ LZ) causes a nearly complete shift to the lower molecular weight fractions. (B-D) Coomassie-stained SDS-PAGE gels showing proteins in the fractions indicated with colored bars in (A). Asterisks indicate degradation products.

7.4 The TbBILBO1-LZ mediates filament assembly

The behavior of the purified 6×His-MBP-TbBILBO1-FL suggested that it could form large oligomers. To examine this, rotary metal shadowing EM experiments were carried out using the purified 6×His-MBP-TbBILBO1 eluted in V_0 of the column. The EM images revealed a filament-like structure decorated with paired globules along the filament (Figure 30A). The lengths of the interval rods were measured to be 40 - 45 nm, in good agreement with the predicted size of the TbBILBO1-CCD (Figure 27). The globular structures of 5-7 nm in diameter matched the size of the MBP moiety together with the fused TbBILBO1-NTD. This assembly mode suggests that the oligomerization of TbBILBO1 is mediated by one or more of the structural elements flanking the CCD namely the NTD and the EFh on the N-terminal side, and the C-terminal LZ. This

hypothesis was systematically tested by removal of each domain in turn and observation of the purified protein by rotary metal shadowing EM.

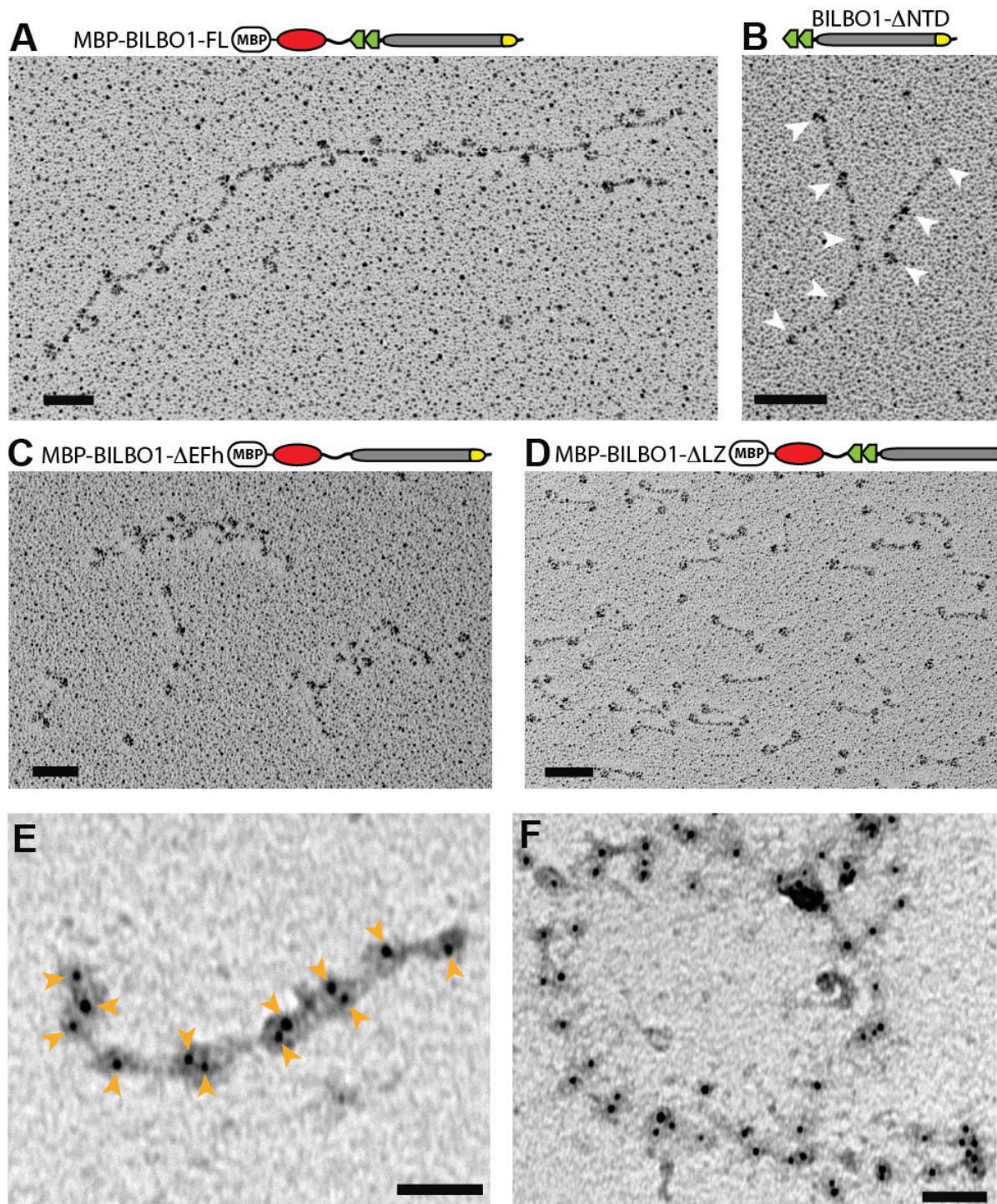


Figure 30 The TbBILBO1-LZ is essential for oligomerization.

(A) Rotary metal shadowing EM image of MBP-tagged TbBILBO1-FL. The protein formed a linear structure with globular MBP moieties packed along the filament. (B) Deletion of the NTD did not preclude filament formation. Note that this construct was soluble even when expressed without an MBP tag, with the smaller bead-like structures of the EFhs still being visible (arrowheads). (C) Deletion of the EFh did not preclude filament formation, although the average length was decreased. (D) Deletion of the LZ

completely disrupted filament assembly. Only dumbbell-like structures were observed. (E) Negative staining EM image of 6×His-MBP-TbBILBO1-FL labeled with 5-nm Ni-NTA-Nanogold. The oligomer is a linear filament. Orange arrowheads indicate the back gold particles. (F) Negative staining image as in E. Some oligomers had sufficient flexibility to form a complete circle. Scale bars, 50 nm.

Removal of the NTD did not significantly affect filament formation, although it led to a slight reduction in the average filament length (Figure 30B). Deletion of the EFh produced a similar effect (Figure 30C). However, deletion of the LZ completely abolished filament assembly, resulting in only dumbbell-like structures as seen for the CCD alone (Figure 30D, compare with Figure 27). These results are consistent with the SEC data showing that deleting the LZ favored dimer formation (Figure 29D).

To further confirm the linear assembly of TbBILBO1-FL, the N-terminal 6×His tag was labeled using 5-nm Ni-NTA-Nanogold (Nanoprobes). The labeled sample was then examined by negative-staining EM, which showed a similar filament-like structures decorated with gold particle pairs being 40-45 nm apart from neighboring pairs (Figure 30E). Furthermore, the filaments seemed very flexible and could even bend to form circular structures (Figure 30F).

7.5 TbBILBO1 assembles into fibers

Given that 6×His-MBP-TbBILBO1-FL forms filament-like oligomers and the majority of it was unable to pass through the size-exclusion column (Figure 29A, B), it seemed likely that TbBILBO1 might form even larger and higher-order assemblies. Therefore, TbBILBO1-FL was further examined directly after affinity purification without doing SEC. It was found that the linear filaments were capable of forming much larger assemblies. Negative-staining EM images showed that two TbBILBO1 filaments could laterally interact with each other (Figure 31A, B). This two-filament structure was often maintained for several micrometers, suggesting that the bilateral interaction was neither random nor nonspecific (Figure 31C). Furthermore, multiple filaments were frequently observed to interact laterally to assemble into a highly ordered fiber (Figure 31D). These bundled fibers could condense and extend for a few micrometers, suggesting that it is a specific interaction-mediated higher-order assembly (Figure 31E).

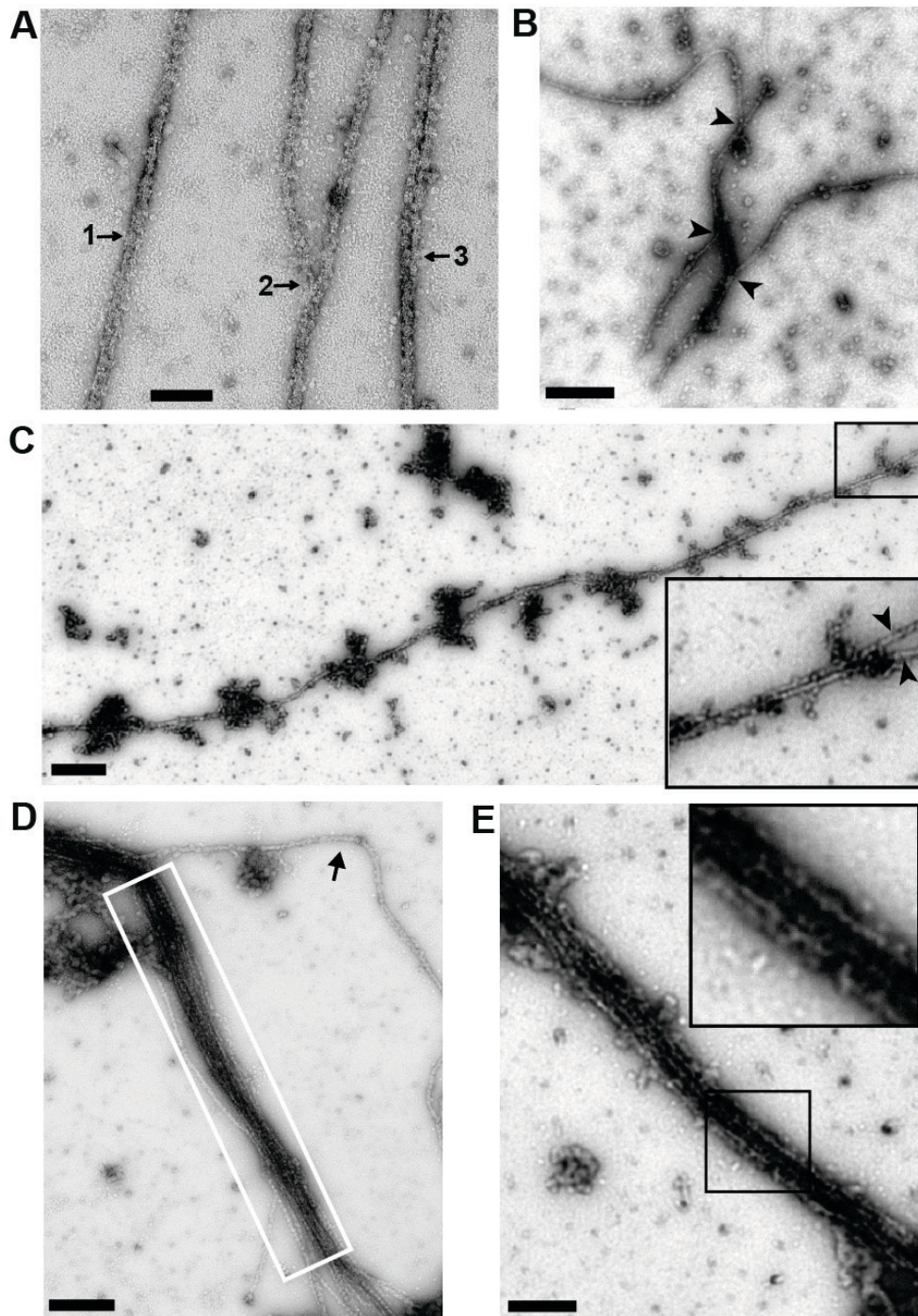


Figure 31 TbBILBO1 linear oligomers further form condensed lateral assemblies.

(A) Lateral interaction of TbBILBO1-FL filaments at three different stages: 1 - single filament; 2 - two semi-aligned filaments; 3 - a parallel two-filament structure. (B) Lateral association of three filaments. Arrowheads indicate the junctions of the interactions. (C) Two long filaments with tight lateral association forming a structure several micrometers long. The inset shows a fork-like structure with the two filaments indicated by arrowheads. (D) Multiple laterally associated filaments of TbBILBO1 forming a bundle (white box). The arrow indicates a filament that is only partially associated to one end of the multi-filament bundle. (E) A condensed bundle formed by multiple tightly associated TbBILBO1 filaments. The inset shows an enlarged view of a segment of the structure. All images were acquired by negative staining EM. Scale bars, 50 nm in (A), 200 nm in (B - E).

7.6 Discussion

Having demonstrated the essential functional role of the NTD and its 3D structure (chapter 6), the TbBILBO1 assembly mechanism was then considered. Rotary metal shadowing EM studies demonstrated that the central coiled-coil region forms an antiparallel dimer (Figure 25). SEC results showed that purified recombinant TbBILBO1 forms large assemblies (Figure 29). Further experiments were then carried out on the purified recombinant full-length protein and various truncations. Results from both SEC and rotary metal shadowing EM demonstrated that the full-length protein forms linear oligomers, and that deletion of either the NTD or EFh domains did not significantly impair oligomerization capacity (Figure 30). Removal of the C-terminal LZ, however, prevented the formation of oligomers and led to dimeric forms predominating. When purified recombinant full-length TbBILBO1 was analyzed by EM without first separating the preparations by SEC, it was found that the protein formed large filamentous bundles with multiple strands associated together laterally (Figure 31).

Drawing all these observations, the following model for the structure and assembly of TbBILBO1 is proposed (Figure 32A). TbBILBO1 forms an antiparallel dimer via its central coiled-coil region, with the NTD and EFh domains projecting outward from the dimer in opposing directions. During purification of the various constructs of TbBILBO1, it was observed that the variable loop region between the NTD and EFh was more prone to degradation than the rest of the protein (data not shown). This supports the theory that the linkers act to sustain the NTDs at a distance from the plane of the dimer.

The formation of inter-dimer contacts via the projecting C-terminal LZs then leads to the formation of long linear filaments (Figure 32A). The localization experiments showed that the LZ is necessary but not sufficient for correct targeting, but it is unclear whether these domains specifically contain the targeting information, or if assembly of TbBILBO1 into oligomeric forms is a prerequisite for retention at the FPC. In the absence of the LZs, the truncated TbBILBO1 molecules were observed to form cytoplasmic punctae that clustered in the vicinity of the FPC, providing some support for the latter hypothesis (Figure 11E).

Another open question is whether the position of the LZs makes the dimers radially symmetric - this has implications for the pitch of the filament, and the relative orientation of the dimers within it. The positioning of the NTDs and EFhs in the filaments makes it possible that these domains have a role in coordinating the oligomeric interactions (Figure 32A, inset). This is partially supported by the observation that although deletion of these two regions does not affect filament assembly, it does appear to shorten the total length of the oligomers, implying a stabilizing function (Figure 30B, C).

The creation of the observed fibers of TbBILBO1 (Figure 31) is predicted to occur by means of lateral interactions between filaments. It is not possible to conclude, based on the current data, whether the filaments within the threads are parallel (as shown in Figure 32B, C) or staggered. The threads could assemble to form the FPC in at least three different ways. They could conceivably form a zigzag arrangement with the individual dimers running parallel to the long axis of the flagellum, although this seems unlikely given the lack of extreme flexibility between the dimers and the observed propensity of the threads to form long linear assemblies. Alternatively, they could wrap around the neck of the FP in a solenoid (Figure 32B). A caveat here is that the FPC must permit passage of the MtQ that extends from the basal body region along the longitudinal axis of the cell towards the cell anterior. It could perhaps be accommodated by a localized displacement of the solenoid. A third possibility is suggested by a recent electron tomography study of the region around the FP (Lacomble, Vaughan et al. 2009). Here, the electron-dense material comprising the FPC was observed to form a horseshoe shape, thus leaving a gap for placement of the MtQ. Although it is not known if TbBILBO1 is part of the electron-dense component of the FPC, if it is assumed to be then a third model is possible. Here, parallel threads of TbBILBO1 wrap around the FP neck but are of insufficient length to completely encircle it. This model implies the existence of some kind of capping protein to limit filament growth (Figure 32C). A possible means of distinguishing between these models would be to analyze in the future whether the FPC becomes either thicker or wider upon overexpression of TbBILBO1.

It was reported previously that overexpression of untagged full-length TbBILBO1 is nontoxic (Bonhivers, Nowacki et al. 2008). The small size of the Ty1 epitope tag used in the *in vivo* studies here is presumably sufficient to prevent any deleterious effects on

full-length TbBILBO1 function. The previous study also stated that overexpression of either N- or C-terminally EGFP-tagged TbBILBO1 caused a growth arrest and a dominant negative phenotype similar to that seen following RNAi depletion of the protein - namely a detached flagellum in an abnormally elongated cell posterior (Bonhivers, Nowacki et al. 2008). As here, no FPC was reported to be present at the detached posterior flagella. The authors postulated that this growth arrest was due to a dominant negative effect. Given the large size of the EGFP tag (37 kDa), it seems likely that this growth arrest was due to the EGFP module interfering with the normal function of the NTD. The fact that this arrest was seen also in C-terminal EGFP-tagged TbBILBO1 constructs supports the notion that the NTD (or EFh) might communicate with the C-termini of dimers/oligomers (Figure 32A, inset).

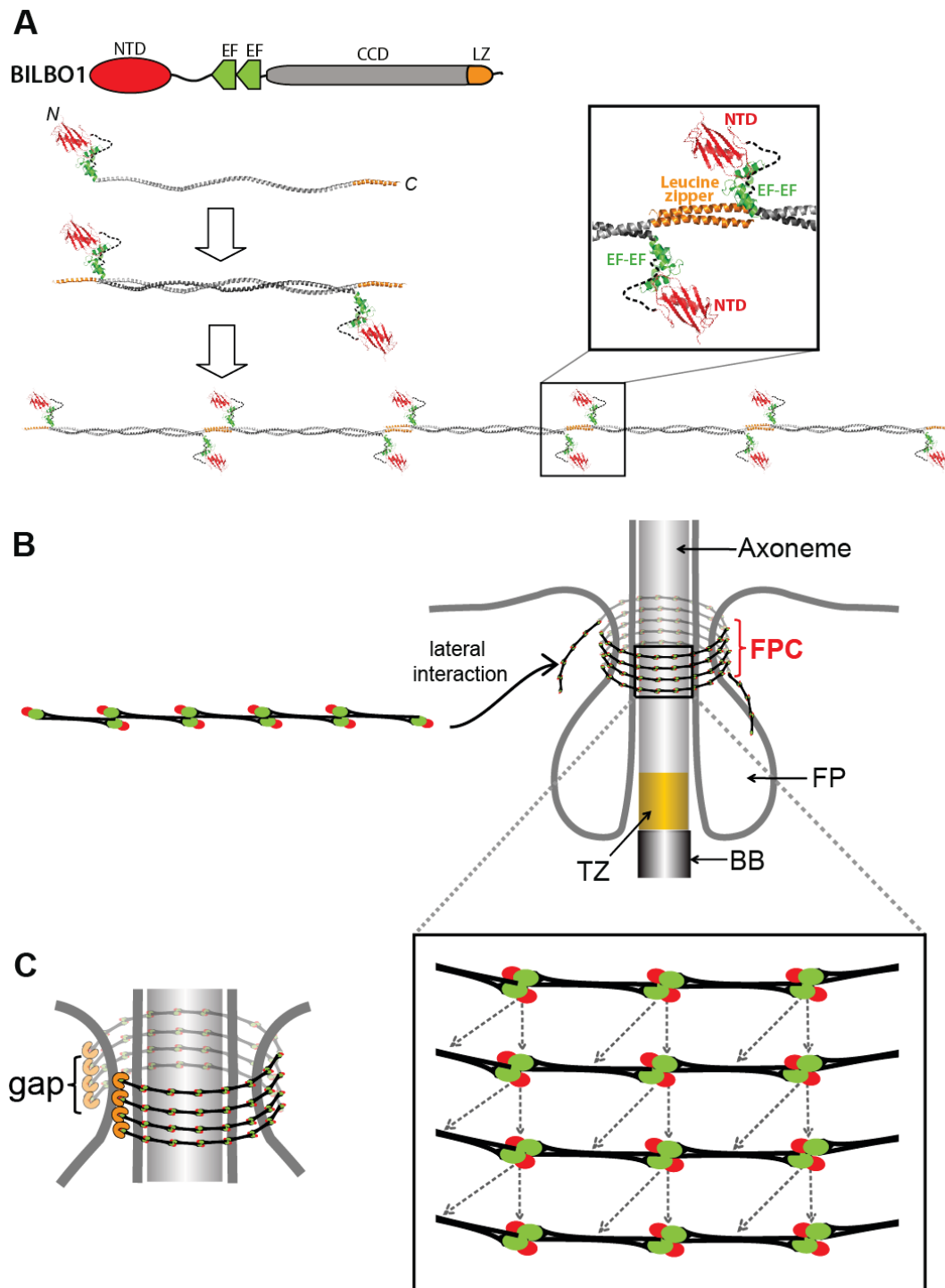


Figure 32 Assembly mechanisms of TbBILBO1 at the FPC.

(A) Schematic of the inferred assembly mechanism of the TbBILBO1 filament. Two molecules form an antiparallel dimer via their CCDs, which then assemble into a linear structure through the interactions between the C-terminal LZs. Enlarged is a close-up view of the predicted inter-dimer junction. (B) A hypothetical model showing the possible assembly of TbBILBO1 at the FPC. The filament forms a solenoid to encircle the FP neck. An enlarged view of the boxed region shows the possible lateral interactions between filaments. FP: flagellar pocket; TZ: transition zone; BB: basal body. (C) An alternative model showing a horseshoe-like arrangement of TbBILBO1 filaments at the FPC. A possible capping protein at the tip of the filaments is indicated by orange crescents.

8 The EF-hand motif, filament junction visualization, and a TbBILBO1 binding partner

8.1 Summary

In chapter 6, it was shown that the conserved surface patch identified in the TbBILBO1-NTD appears to be essential for the proper function of TbBILBO1 in the parasite and therefore represents an attractive candidate site for therapeutic drug design. In chapter 7, it was shown that TbBILBO1 can form filament-like structures which further assemble into fibers by lateral interactions. Here we try to identify the interacting partner(s) of the TbBILBO1-NTD and its possible regulatory interaction with the EFh in the assembly and operation of the FPC.

8.2 Calcium-binding property of the TbBILBO1-EFh motif

In chapter 7, it was mentioned that TbBILBO1 filament could form fiber-like structures by lateral interaction between filaments. At this moment, it is unknown how this interaction occurs, whether via amino acid-specific interactions or via unspecific van der Waals interactions within filaments. However they are formed, we hypothesized that the EFh might play a regulatory role in the assembly and/or function of the FPC.

TbBILBO1 has two EFh motifs ranging from residue 183 to residue 249. EFh motifs have the ability to bind calcium and undergo structural rearrangements upon binding (Lewit-Bentley and Rety 2000; Zheng, Liu et al. 2010). To analyze whether the EFh motifs in TbBILBO1 have this ability, we performed biophysical analysis using CD, SLS, and thermofluor method (Figure 33). The far-UV CD analysis showed that stripping off calcium using EDTA resulted in a classical random coil structure with a maximum below 0 mdeg and minimum at ~200 nm. In contrast, calcium binding led to a characteristic spectrum of α helices with two minima at 209 and 220 nm and a positive signal at ≤ 200 nm (Figure 33A).

The SLS results showed that in the presence of 2mM EDTA (apo form), the EFh was eluted much earlier than the calcium-loaded form, even though both proteins were monomeric and had the same molecular weight (Figure 33B). It suggested that in the absence of calcium the EFh is improperly folded therefore more loosely packed. Furthermore, thermofluor assays showed that the melting temperature (T_m) for the calcium-bound and the apo forms were 57.0°C and 38.5°C, respectively, which further demonstrates that binding to calcium makes the EFh well-folded with a very compact structure (Figure 33B). Homology modeling of the EFh by the (PS)2-v2 protein structure prediction server using the human calmodulin-like protein (hCLP) structure as the modeling template showed that the EFh has acidic residues in the loops, which are likely to coordinate calcium binding (Figure 33D) (Han, Han et al. 2002; Chen, Hwang et al. 2009).

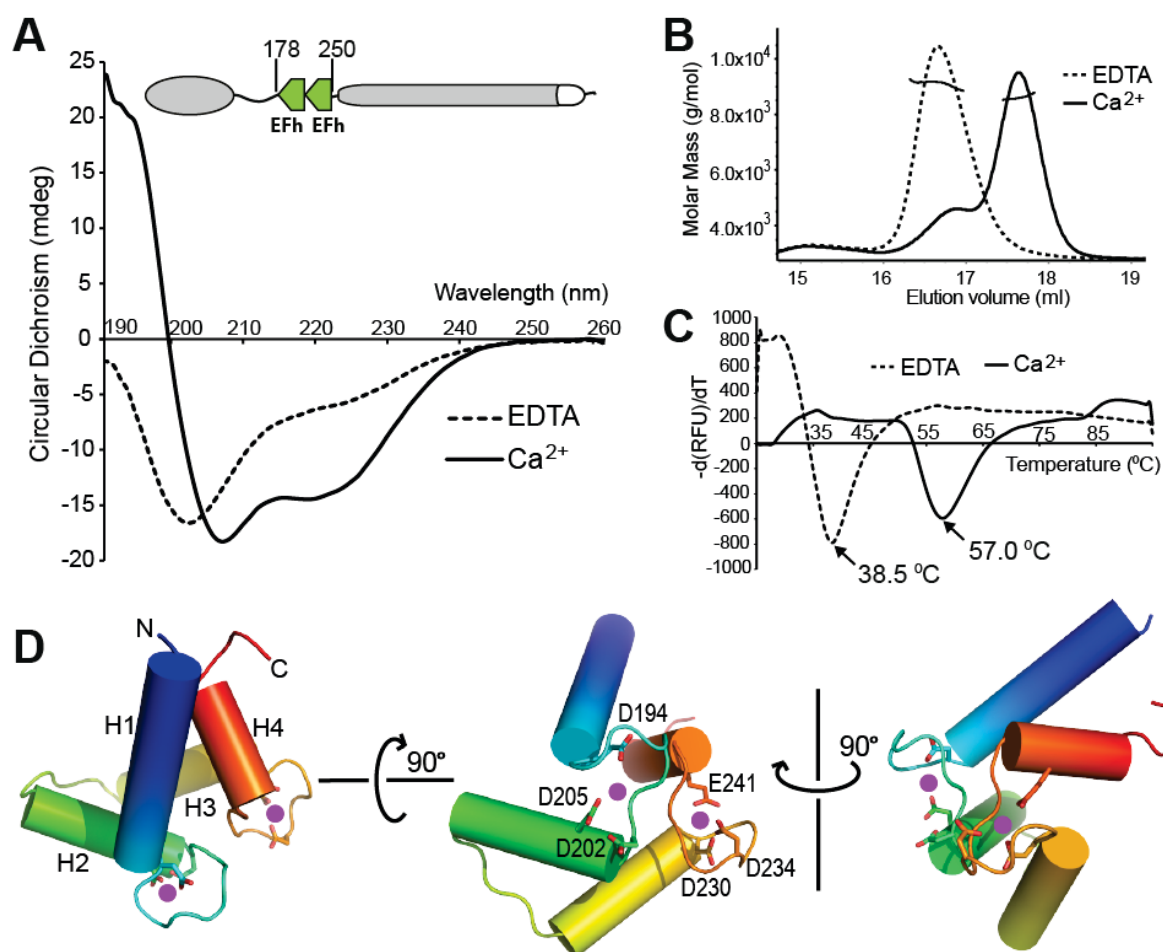


Figure 33 Calcium-binding property of the TbBILB01-EFh motifs.

(A) Far-UV CD spectra of the TbBILB01-EFh (aa178-250) in the presence of either 2mM CaCl_2 or 2mM EDTA. Complete stripping off of calcium by EDTA resulted in the apo form that has a classical random coil structure with maximum below 0 mdeg and minimum at ~200 nm. Conversely, calcium binding led to a characteristic spectrum of α helices with two minima at 209 and 220 nm and positive signals with $\lambda \leq$

200 nm. (B) SLS results of the two forms of the TbBILBO1-EFh. The two forms were both monomeric but the apo form was eluted much earlier than the calcium-loaded form, suggesting that in the absence of calcium, the EFh is improperly folded and therefore more loosely packed. (C) Melting curves of the TbBILBO1-EFh with and without loaded calcium measured by thermofluor assays. The melting temperature (T_m) for the apo and calcium-bound form were 38.5°C and 57.0°C, respectively. This further demonstrates that binding to calcium makes the EFh undergo conformational switch from unfolded random coils to a well-folded compact structure. (D) Three orthogonal views of the homology-based modeling result of the TbBILBO1-EFh (aa178-250). The model was generated by the (PS)2-v2 protein structure prediction server (Chen, Hwang et al. 2009). The cartoon is color-ramped from blue at the N-terminus to red at the C-terminus. The four α helices (H1-4) in the two EFh motifs are shown as cylinders. Acidic residues in the loops, which are likely to coordinate calcium binding, are shown as sticks. The two predicted calcium binding sites are shown as magenta dots.

8.3 Visualization of the filament junction formation

The filament formation of TbBILBO1 is via the C-terminal LZ (Chapter 7). However, due to the low-resolution limit, the precise interaction mechanism and amino acids responsible for this filament formation are difficult to determine. To address this, two constructs were generated to study the complex formation of the filament junction by X-ray crystallography. The first construct consists of residues 1 - 370 (TbBILBO1-NH); the DNA fragment was ligated into MalpET vector. The second construct consists of residues 400 - 587 (TbBILBO1-CH); the DNA fragment was ligated into pET15b vector (Figure 34A). If the two constructs can form a complex, based on the proposed model (Chapter 7), it will consist of two TbBILBO1-NH and two TbBILBO1-CH in an antiparallel configuration (Figure 34A).

The constructs were coexpressed in *E. coli* BL21(DE3) and soluble proteins subsequently purified. SLS analysis of the proteins after SEC confirmed the formation of the complex with the observation of a peak at the molecular weight of 220 kDa, which corresponded to an assembly with two copies of MBP-TbBILBO1-NH (MW of 85 kDa) and two copies of 6 \times his-TbBILBO1-CH (MW of 23.5 kDa) (Figure 34B). For crystallization, the MBP and the loosely linked TbBILBO1-NTD were removed by the addition of thrombin since this protease can cleave the linker region of TbBILBO1 at position of R175. Meanwhile, thrombin also releases the N-terminal 6 \times His-tag from the TbBILBO1-CH. After a second passage through a Ni-Hitrap column to remove MBP-TbBILBO1-NTD, the complex was purified further by SEC (Superdex-200 16/60) (Figure 34C). The Coomassie-stained SDS-PAGE gels of the SEC result showed that TbBILBO1-

NH and TbBILBO1-CH were co-eluted in the same fractions along with the additional impurity of uncut MBP-TbBILBO1-NH (Figure 34D). The impurity was removed by applying the fractions to an amylose column (Figure 34E). The pure complex was then subjected to crystallization screening. An initial crystallization hit was obtained from the Wizard screen in the condition containing 0.1M phosphate-citrate pH 4.2, 0.2M Li₂SO₄, and 20% (w/v) polyethylene glycol 1000 (Figure 34F). An attempt to reproduce crystals manually in this condition did not succeed, and crystallization could be replicated only by micro-seeding. However, the result did not produce high-quality crystals as they only diffracted to a very low resolution of 8-10 Å (Figure 34G). To overcome this problem, further optimization in the future would be needed.

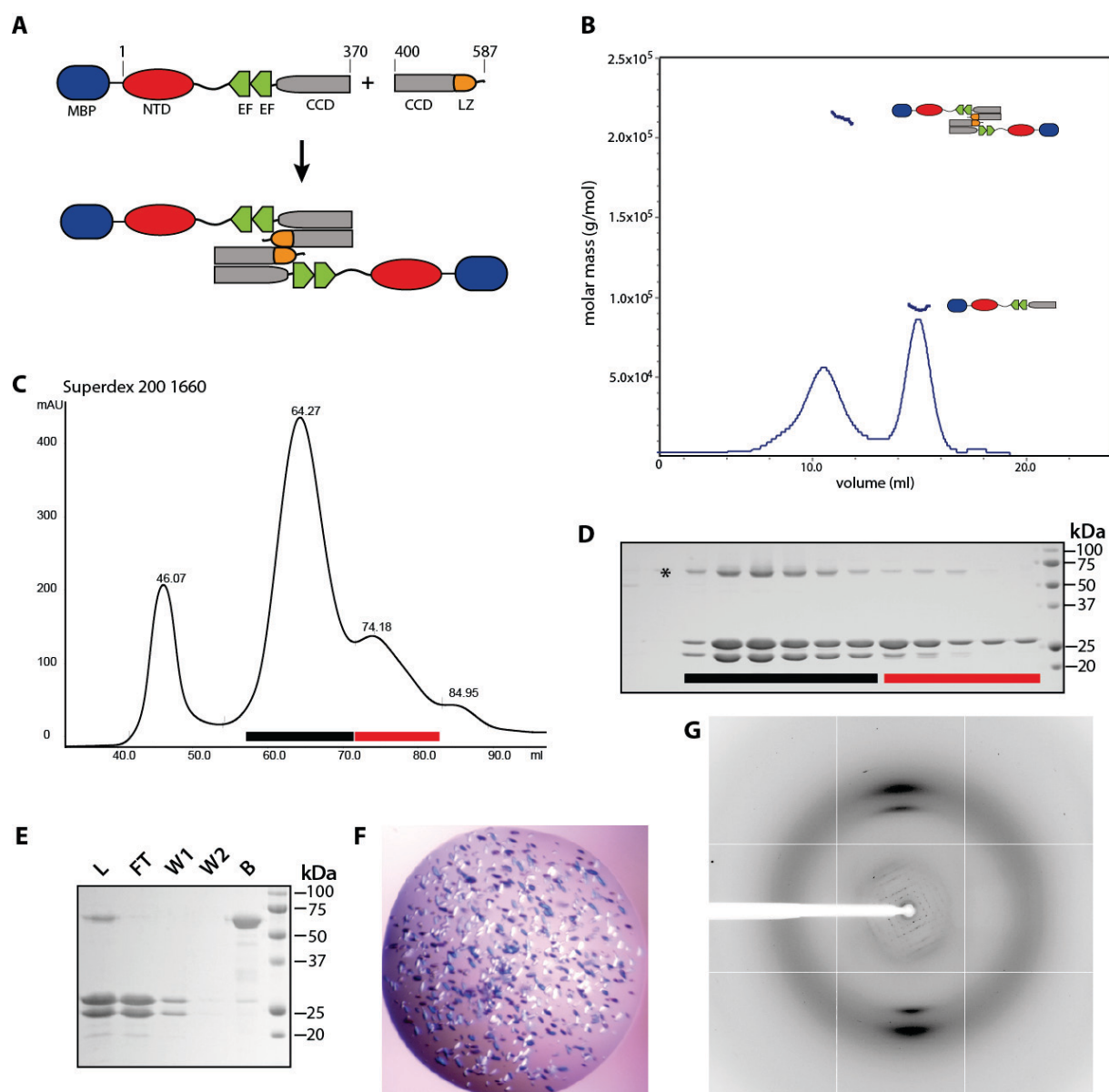


Figure 34 Attempts to structurally characterize the complex formation at the filament junction.

(A) Constructs used for probing complex formation of the filament junction. For this purpose, two constructs were generated: MBP-TbBILBO1-NH (aa1-370) and TbBILBO1-CH (aa400-587). If they can form a complex, it was predicted to consist of two copies of MBP-TbBILBO1-NH and two copies of TbBILBO1-CH oriented in an antiparallel manner. (B) SLS analysis showed that the two constructs could form a complex with the molecular weight of 220 kDa. (C) SEC elution profile of the complex of TbBILBO1-NH and TbBILBO1-CH after removing its MBP and 6×his-tag. (D) Coomassie-stained SDS-PAGE gel showing proteins in the fractions indicated with colored bars in (C). Asterisk marks the uncut MBP-TbBILBO1-NH. (E) Amylose column purification to remove uncut MBP-TbBILBO1-NH. L, load; FT, flow-through; W1, the first wash; W2, the second wash; B, the protein retained on the amylose beads. (F) Crystals of the filament junction complex. (G) X-ray diffraction image of the crystal.

8.4 FPC4 is a TbBILBO1 binding partner

Previously, it was shown that the NTD of TbBILBO1 has a conserved surface patch required for its function (Chapter 6). It was hypothesized that the NTD might be responsible for interacting with other protein. Based on predictions using FTsite, the NTD may have two potential binding sites for its interaction partner(s) (Figure 35) (Ngan, Hall et al. 2012). The prediction is based on experimental evidence that ligand-binding sites also bind small organic molecules of different shapes and polarity. The first predicted binding site (with the highest ranking score) is located on the solvent-exposed side of the β -sheet (Figure 35B), similar to the crater-like structure where the conserved surface patch is located. This binding site consists of residues Asp10, Lys15, Lys62, Trp71, Tyr87, Phe89, Glu98, Ser99, Gln100, Lys101, Glu102, and Ile103 (Figure 35C). Interestingly, most of the conserved surface patch essential for NTD function is located within this region. The second predicted binding site is located on the cleft of the distal end of the domain, between β 4/ β 3 and α 1 (Figure 35D). The residues contributing to this binding are Ile28, Thr32, Glu36, Ser58, Ser59, Lys60, Ile61, Asp73, Leu74, and Ile75 (Figure 35E).

Our collaborators at the Universite Bordeaux Segalen, Dr. Melanie Bonhivers and Dr. Derrick Robinson, have identified another novel FPC component (Gene ID: 3659636) as a potential TbBILBO1 binding partner as indicated by the yeast two-hybrid assay (unpublished data). Preliminary data have suggested that FPC4 localizes to the FPC, overlapping with TbBILBO1 (unpublished data). FPC4 is predicted to be highly disordered over both its N- and C-terminal domains, with a globular part in the middle

region (aa71-259) (Figure 36A). This globular part is predicted to have five α -helices and one β -strand (Figure 36B). Since FPC4 seem to directly interact with TbBILBO1, we set out to determine their mechanism of interaction.

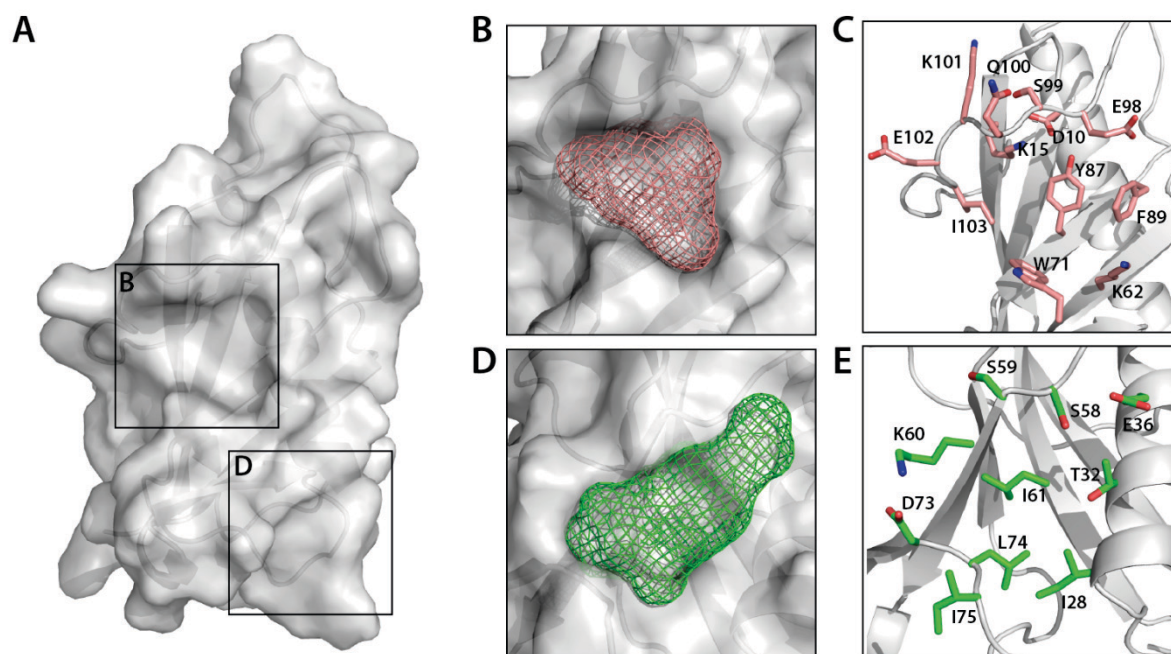


Figure 35 Predicted ligand binding sites on the N-terminal domain of TbBILBO1.

(A) Surface plot of the TbBILBO1-NTD crystal structure showing two predicted ligand binding sites (boxes B and D). The prediction was generated by the FTsite server (Ngan, Hall et al. 2012). (B) Enlarged rectangular inset in (A) showing the first putative ligand-binding site (shown in salmon colored mesh). (C) The residues in the first predicted ligand binding site. (D) Enlarged rectangular inset in (A) showing the second putative ligand-binding site (shown in green colored mesh). (E) The residues in the second predicted ligand binding site

Based on the yeast two-hybrid data, the region of FPC4 essential for interacting with TbBILBO1-NTD was predicted to be residues 357 - 440. To check the complex formation *in vitro*, the DNA fragment encoding these residues was ligated into pET28a expression vector and co-expressed with TbBILBO1-NTD. The NTD of TbBILBO1 used for this experiment consisted of residues 1 - 120; its DNA fragment was ligated into pET15b expression vector. Co-expression of both domains in *E. coli* and purification with Ni-HiTrap and SEC Superdex200 1660 resulted in two elution peaks at the retention volume of 86,88 ml (corresponding to complex formation) and at the retention volume of 94.51 ml (corresponding only to TbBILBO1-NTD molecules) (Figure 37A,B). Analysis by SLS showed that the complex had a molecular weight of 25 kDa, which roughly

corresponded to one molecule of 6×His-TbBILB01-NTD' (1 - 120) (MW = 15.6 kDa) and one molecule of 6×His-FPC4-CTD (residues 357 - 440) (MW = 12.2 kDa).

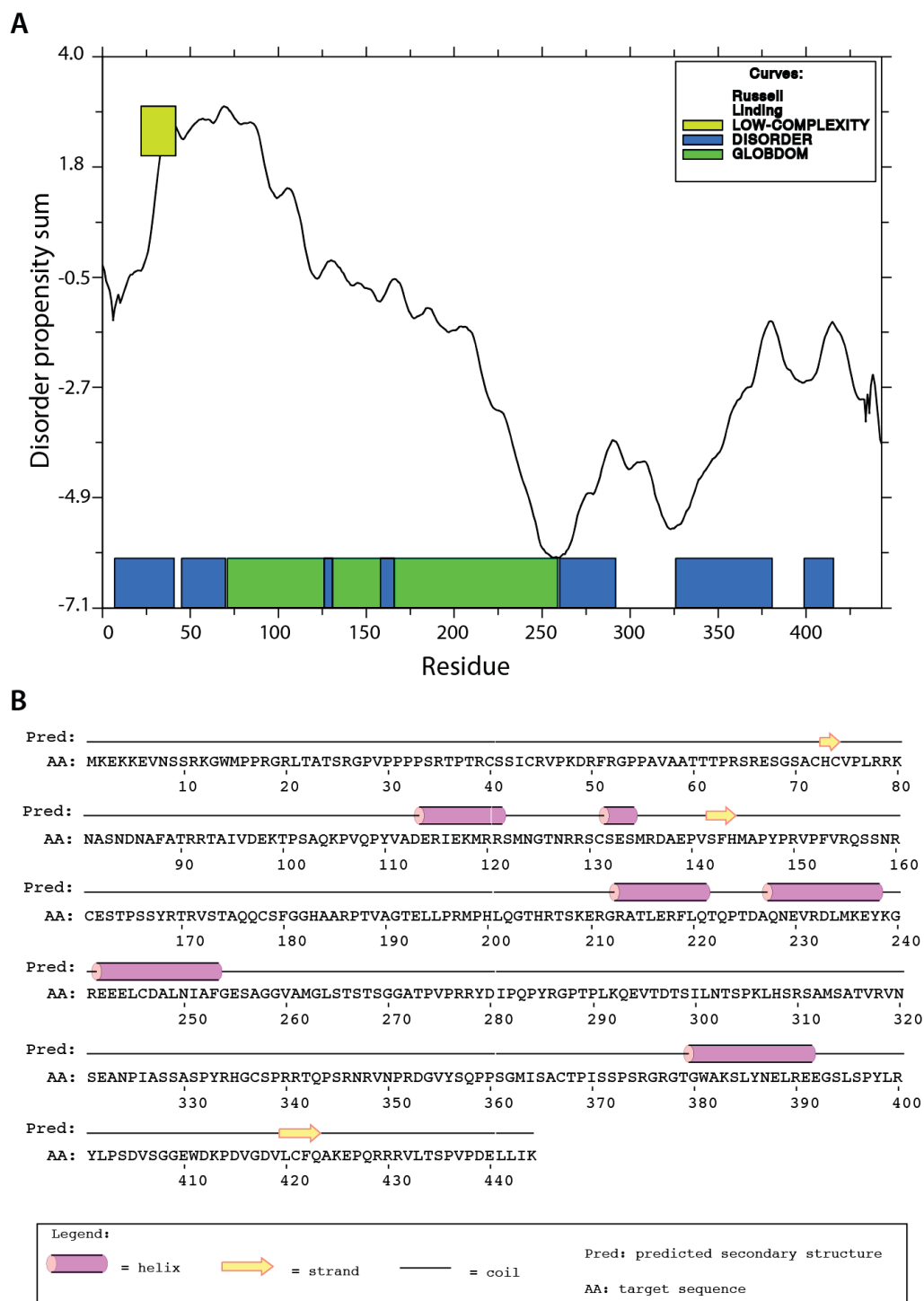


Figure 36 Primary sequence based bioinformatics analyses of *T. brucei* FPC4.

(A) Globularity/disorder prediction based on protein sequence of FPC4. The result showed that the middle region of the sequence (aa71-259) is likely to form a globular domain, while the rest residues are

predicted to be mostly disordered. The prediction was generated by the GLOBPLOT 2 server (Linding, Russell et al. 2003). (B) Secondary structure predictions of FPC4. The result showed that most of the sequence is predicted to be random coil/unstructured, with some parts forming α -helices. The prediction was generated by PSIPRED (Jones 1999).

An attempt to remove the His-tag from both proteins resulted in the degradation of FPC4 (aa357-440) to a lower molecular weight (Figure 37C). This is probably due to the presence of a thrombin protease site in its protein sequence at position R377. The shorter construct of FPC4, which consisted of residues 394 - 444, was generated to avoid the thrombin protease site. This construct was ligated into MalpET expression vector which provides an N-terminal MBP and a 6 \times His tag. This construct was then co-expressed with TbBILBO1-NTD' (aa1-120) and purified. After removing the MBP-tag and 6 \times His-tag, the proteins were further purified by SEC Superdex-75 16/60 (Figure 37D, E). SLS was used for molecular weight determination, which showed that the complex still formed, with a molecular weight of 18 kDa (Figure 37G). It corresponded to one molecule of TbBILBO1-NTD' (MW = 13.4 kDa) and one molecule of FPC4-CTD (aa394- 444) (MW = 5.8 kDa).

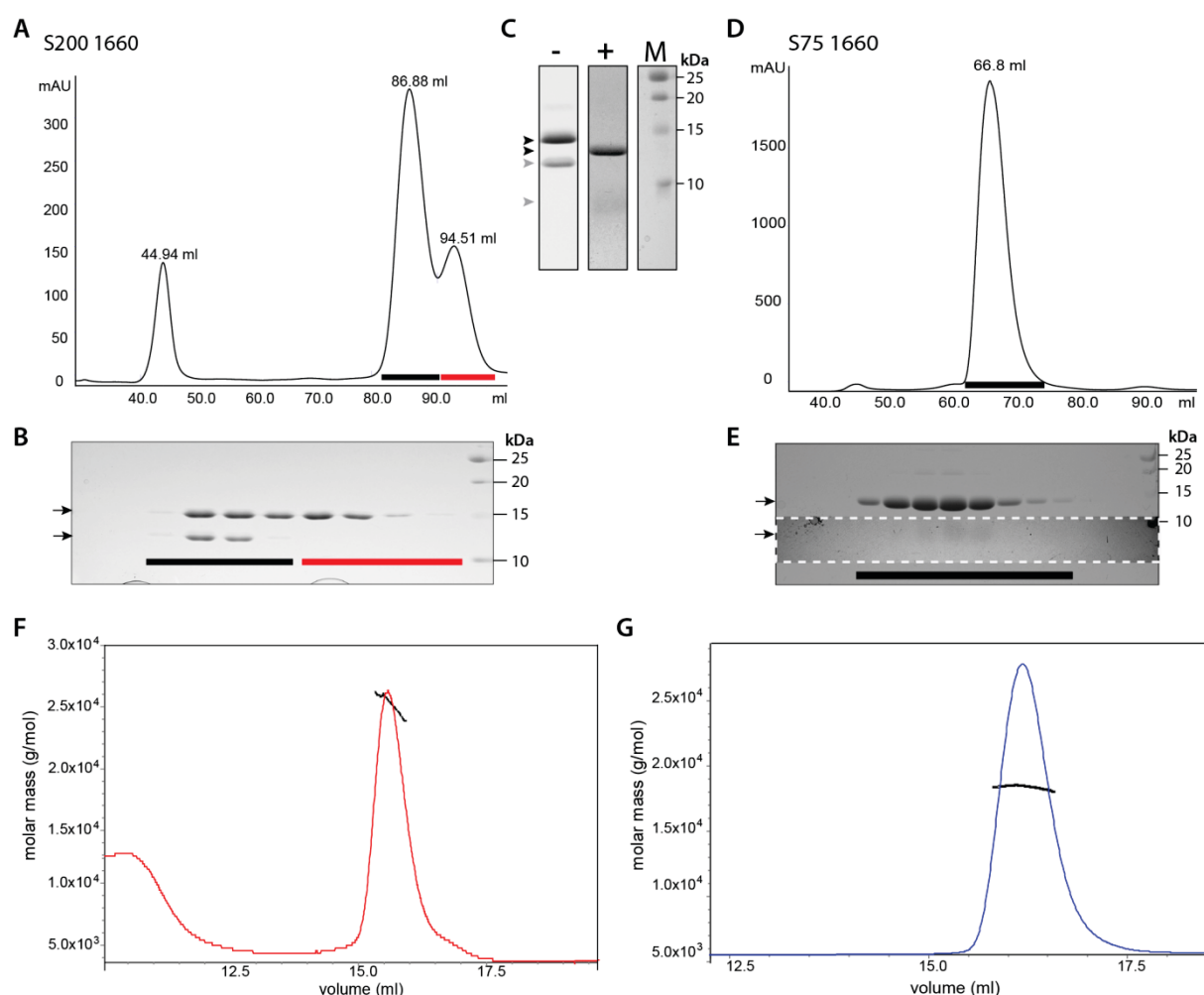


Figure 37 Formation of a stable complex between the TbBILBO1-NTD and the FPC4-CTD.

(A) SEC elution profile (S-200 16/60) of the copurified 6xHis-TbBILBO1-NTD' (aa1-120) and 6xHis-FPC4-CTD (aa357-440). Both proteins were co-eluted in the elution peak of 86.88 ml. (B) Coomassie-stained SDS-PAGE gel showing proteins in the fractions indicated with colored bars in (A). Upper arrow indicates the 6xHis-TbBILBO1-NTD' and lower arrow indicates 6xHis-FPC4-CTD. (C) Coomassie-stained SDS-PAGE gels of the complex fractions treated by thrombin. Upper and lower black arrowheads indicate the 6xHis-TbBILBO1-NTD' without (-) and with (+) thrombin cleavage, respectively. Upper and lower gray arrowheads indicate the 6xHis-FPC4-CTD without (-) and with (+) thrombin cleavage, respectively. M, proteins marker. (D) SEC elution profile (Superdex-75 16/60) of the copurified TbBILBO1-NTD (aa1-120) and FPC4-CTD (aa394-444). Both proteins were co-eluted in the elution peak of 66.80 ml. (E) Coomassie-stained SDS-PAGE gel showing proteins in fractions indicated by a black bar in (D). The area in the white dashed box was exposed more to show the lower molecular weight bands. Upper arrow indicates the TbBILBO1-NTD' (aa1-120) and lower arrow indicates FPC4-CTD (aa394-444). (F) SLS results of the complex of 6xHis-TbBILBO1-NTD' (aa1-120) and 6xHis-FPC4-CTD (aa357-440). The apparent molecular weight of 25 kDa indicates the formation of a hetero-dimer. (G) SLS result of the complex of TbBILBO1-NTD' (aa1-120) and the shorter construct of the FPC4-CTD (aa394-444). The apparent molecular weight of 18 kDa indicates that the hetero-dimer formation was still maintained.

8.5 Discussion

As discussed in chapter 7, in both the solenoid and the horseshoe models of TbBILBO1 assembly in the FPC, the EFh might play a regulatory role in the assembly and/or function of the FPC. Here, we have confirmed that the EFh motif can reversibly bind calcium. Furthermore, we found that calcium binding induces conformational changes to the EFh. It is therefore conceivable that the EFh, in response to calcium availability, might reversibly interact with another region of TbBILBO1 in a neighboring strand. The lateral association between neighboring filaments not only facilitates the formation of a condensed structure, but might also serve to regulate the size of the FPC in a calcium-dependent manner by the EFh.

The filament formation of TbBILBO1 via the C-terminal LZ could be visualized precisely if we could determine the complex formation of the junction region. To that end, two constructs were generated for crystallization experiments. SEC and SLS confirmed formation of a complex that consisted of two molecules of TbBILBO1-NH and two molecules of TbBILBO-CH, with a molecular ratio of 1:1. Even though crystallization experiments produced some crystals, they did not diffract X-rays very well. This might be due to a packing problem in the crystals. In the future, further optimizations for the crystallization conditions should be carried out, such as by lysine methylation or by preparing shorter constructs that are still competent for complex formation.

The TbBILBO1-NTD has two potential ligand binding sites as predicted by the FTsite server. One of the binding sites agrees with the conserved patch we have characterized to be essential for *T. brucei* viability. This result further implies that the NTD is likely required for protein-protein interaction. However, the FTsite did not predict the region of the TbBILBO1-NTD corresponding to the aPKC interacting interface in Par6 as a binding site (Figure 26A, C). This might be because this region is blocked by a C-terminal loop therefore it could not form a pocket favorable for binding site predictions. Fortunately, our collaborator has found a TbBILBO1 binding partner, FPC4, following a yeast two-hybrid screen. Its CTD was predicted to interact with the NTD of TbBILBO1. Based on protein primary sequence analysis, the N- and C-terminal regions of FPC4 are predicted to be unstructured. It is possible that the unstructured C-terminus of FPC4 is

wrapping around the TbBILBO1-NTD from one binding site to the second one via the cleft connecting both predicted binding sites. We have also found that the short version of the FPC4 C-terminus (aa394-444) still maintains complex formation with the TbBILBO1-NTD. In the future, we plan to continue pursuing the structure of the complex of both proteins either by X-ray crystallography or by NMR spectroscopy.

9 Conclusions and perspectives

Trypanosoma brucei is a protist parasite that causes trypanosomiasis in sub-Saharan Africa, colloquially known as sleeping sickness (in humans) and nagana (in animals). The disease is transmitted by tsetse flies of the genus *Glossina* and resulted in approximately 10,000 cases in 2009 with approximately 55 million people at risk (Malvy and Chappuis 2011; Simarro, Cecchi et al. 2011). Currently, there is no vaccine available to treat the disease and the available drugs can have lethal side effects (Absalon, Blisnick et al. 2008).

T. brucei is a unicellular and serpentine-shaped organism with a single flagellum emerging near the posterior end of the cell. The flagellum is important for the parasite motility and attachment to the salivary gland epithelium of tsetse fly (Tetley and Vickerman 1985). In the area where the flagellum emerges from the cytoplasm, there is a specialized organelle termed the FP. The FP is the invagination of the plasma membrane and has an important role as the only site for all endocytosis and exocytosis activities of the cell (Overath and Engstler 2004). This organelle is also essential for periodically changing its major VSG so that the parasite is able to evade immune response of the host cells (O'Beirne, Lowry et al. 1998)

At the neck region of the FP is a dense cytoskeletal barrier element called the FPC. The diameter of this region is slightly larger than the flagellum. The FPC presumably serves to anchor the membrane and the axoneme and to position the flagellum in the greater cytoskeleton (Field and Carrington 2009; Lacomble, Vaughan et al. 2009). TbBILBO1 was the first identified component of the FPC, and its depletion by RNAi was shown to prevent FP and FPC biogenesis (Bonhivers, Nowacki et al. 2008). TbBILBO1 is only found in kinetoplastids without apparent orthologs in humans or other organisms (Bonhivers, Nowacki et al. 2008). Based on the homology prediction, TbBILBO1 consists of four main domains - the NTD (aa1-110), two putative EFh (aa183-213 and 221-249), a central CCD (aa263-533), and a C-terminal LZ (aa534-578).

We have determined the structure of the NTD and proposed a possible assembly mechanism for TbBILBO1, which provides a basis for rational drug design and is expected to guide future studies on both TbBILBO1 and the FPC. We also hypothesize that TbBILBO1 binding partners might be able to refine knowledge of assembly mechanisms in the collar.

We have showed that the TbBILBO1 *in vitro* could form filament-like structures via its C-terminal LZ. These filaments can laterally interact to form larger fiber-like structures. At the moment, it is unknown how the lateral interactions occur. However, due to its ability to assemble into high order oligomers, it seems likely that TbBILBO1 could be the main building block of the FPC. The EFh, in response to calcium availability, might have an essential function in the operation of the FPC as a whole. It was shown that the EFh could reversibly interact with calcium and might be facilitating the lateral interaction of TbBILBO1 molecules with those in a neighboring strand in a calcium-dependent manner.

The conserved surface patch on the TbBILBO1-NTD is essential for viability of the cells. This surface patch is possibly a binding site for the CTD of FPC4, a newly identified FPC component. Our collaborators in the Universite Bordeaux Segalen, Dr. Melanie Bonhivers and Dr. Derrick Robinson, also mentioned that the NTD of FPC might bind microtubules. It is therefore possible that FPC4 acts as an anchor of the FPC to the membrane in the neck region of the FP, with its CTD interacting with the TbBILBO1-NTD and its NTD interacting with microtubules (Figure 38A, B). During the interaction of FPC4 with the TbBILBO1-NTD and microtubules, it is possible that both of NTD and CTD of FPC become folded. However, it is still unknown which microtubules can interact with FPC4, whether at random or perhaps only the specialized microtubules of this organism, such as the MtQ that runs along the flagellum from the area of the basal body. If FPC4 specifically interacts with the MtQ, then it could also possibly act as the capping protein mentioned in Chapter 7 which then inhibits the further growth of TbBILBO1 filaments in the FPC.

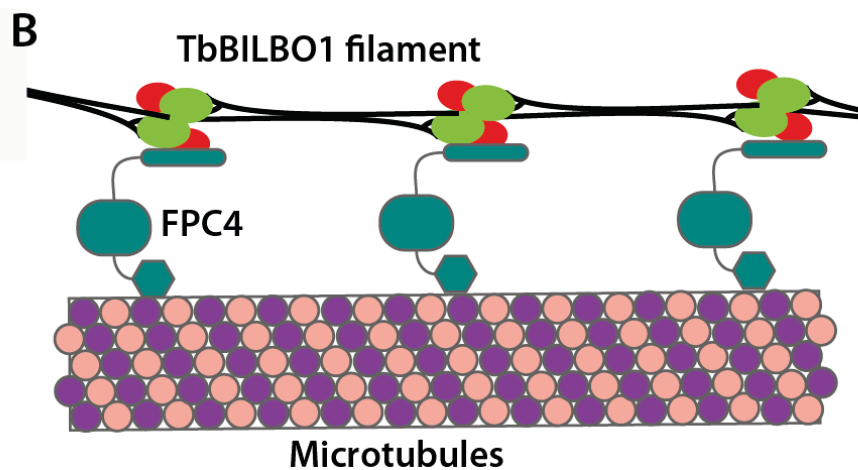
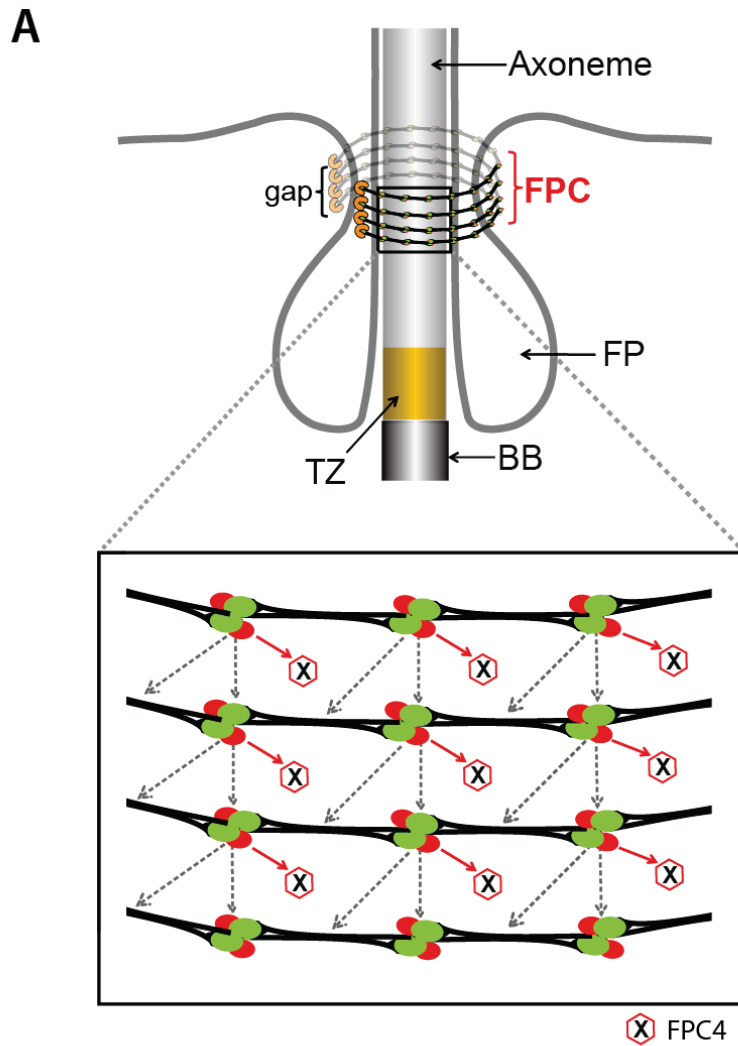


Figure 38 Predicted assembly mechanisms of TbBILBO1 at the FPC.

(A) A hypothetical model showing a horseshoe-like arrangement of TbBILBO1 filaments at the FPC with a possible capping protein at the tip of the filaments is indicated by orange crescents. An enlarged view of the boxed region shows the possible lateral interactions mediated by the NTD and/or the EFh (dashed arrows). The NTD interacts with the CTD of FPC4 (red arrows and hexagons). FP: flagellar pocket; TZ: transition zone; BB: basal body. (B) The possible interactions of NTDs of TbBILBO1 filament with FPC4s

and CTD of FPC4s with microtubules. FPC4 could possibly act as the anchor of the collar to the microtubules in the membrane region of the FP neck to facilitate FPC assembly.

Many questions remain unanswered. In the future, it will be interesting to see if we can determine the high-resolution structure of the filament junction complex to better understand how the interactions occur. It would also be interesting to see if we can solve the structure of the complex of the TbBILBO1-NTD with the FPC4-CTD (and, even more ambitiously, the FPC4-CTD/microtubules complex) to further understand the assembly mechanism of these proteins in the FPC.

References

Absalon, S., T. Blisnick, et al. (2008). "Flagellum elongation is required for correct structure, orientation and function of the flagellar pocket in *Trypanosoma brucei*." J Cell Sci **121**(Pt 22): 3704-3716.

Ackers, J. P., V. Dhir, et al. (2005). "A bioinformatic analysis of the RAB genes of *Trypanosoma brucei*." Mol Biochem Parasitol **141**(1): 89-97.

Allen, C. L., D. Goulding, et al. (2003). "Clathrin-mediated endocytosis is essential in *Trypanosoma brucei*." EMBO J **22**(19): 4991-5002.

Bangs, J. D., E. M. Brouch, et al. (1996). "A soluble secretory reporter system in *Trypanosoma brucei*. Studies on endoplasmic reticulum targeting." J Biol Chem **271**(31): 18387-18393.

Bangs, J. D., L. Uyetake, et al. (1993). "Molecular cloning and cellular localization of a BiP homologue in *Trypanosoma brucei*. Divergent ER retention signals in a lower eukaryote." J Cell Sci **105** (Pt 4): 1101-1113.

Barquilla, A., J. L. Crespo, et al. (2008). "Rapamycin inhibits trypanosome cell growth by preventing TOR complex 2 formation." Proc Natl Acad Sci U S A **105**(38): 14579-14584.

Barry, J. D. (1979). "Capping of variable antigen on *Trypanosoma brucei*, and its immunological and biological significance." J Cell Sci **37**: 287-302.

Bax, A., G. M. Clore, et al. (1990). "¹H-¹H correlation via isotropic mixing of ¹³C magnetization, a new three-dimensional approach for assigning ¹H and ¹³C spectra of ¹³C-enriched proteins." Journal of Magnetic Resonance (1969) **88**(2): 425-431.

Bax, A. and M. Ikura (1991). "An efficient 3D NMR technique for correlating the proton and ¹⁵N backbone amide resonances with the alpha-carbon of the preceding residue in uniformly ¹⁵N/¹³C enriched proteins." J Biomol NMR **1**(1): 99-104.

Bodenhausen, G. and D. J. Ruben (1980). "Natural abundance nitrogen-15 NMR by enhanced heteronuclear spectroscopy." Chemical Physics Letters **69**(1): 185-189.

Bonhivers, M., S. Nowacki, et al. (2008). "Biogenesis of the trypanosome endo-exocytotic organelle is cytoskeleton mediated." PLoS Biol **6**(5): e105.

Bridges, D. J., A. R. Pitt, et al. (2008). "Characterisation of the plasma membrane subproteome of bloodstream form *Trypanosoma brucei*." Proteomics **8**(1): 83-99.

Brown, W. J., D. B. DeWald, et al. (1995). "Role for phosphatidylinositol 3-kinase in the sorting and transport of newly synthesized lysosomal enzymes in mammalian cells." J Cell Biol **130**(4): 781-796.

Brun, R., J. Blum, et al. (2010). "Human African trypanosomiasis." Lancet **375**(9709): 148-159.

Burri, C. (2010). "Chemotherapy against human African trypanosomiasis: is there a road to success?" Parasitology **137**(14): 1987-1994.

Cachon, J., M. Cachon, et al. (1988). "The Paraflagellar Rod - a Structure in Search of a Function." Biology of the Cell **63**(2): 169-181.

Cavanagh, J., W. J. Fairbrother, et al. (2006). Protein NMR Spectroscopy: Principles and Practice. San Diego, Academic Press.

Chappuis, F. o., N. Udayraj, et al. (2005). "Eflornithine Is Safer than Melarsoprol for the Treatment of Second-Stage *Trypanosoma brucei gambiense* Human African Trypanosomiasis." Clinical Infectious Diseases **41**(5): 748-751.

Checchi, F., J. A. Filipe, et al. (2008). "Estimates of the duration of the early and late stage of gambiense sleeping sickness." BMC Infect Dis **8**: 16.

Chen, C. C., J. K. Hwang, et al. (2009). "(PS)2-v2: template-based protein structure prediction server." BMC Bioinformatics **10**: 366.

Chen, V. B., W. B. Arendall, 3rd, et al. (2010). "MolProbity: all-atom structure validation for macromolecular crystallography." Acta Crystallogr D Biol Crystallogr **66**(Pt 1): 12-21.

Clubb, R. T., V. Thanabal, et al. (1992). "A new 3D HN(CA)HA experiment for obtaining fingerprint HN-Halpha peaks in 15N- and 13C-labeled proteins." J Biomol NMR **2**(2): 203-210.

Cross, G. A. (1975). "Identification, purification and properties of clone-specific glycoprotein antigens constituting the surface coat of *Trypanosoma brucei*." Parasitology **71**(3): 393-417.

Cross, G. A. M. (1996). "Antigenic variation in trypanosomes: Secrets surface slowly." BioEssays **18**(4): 283-291.

Czichos, J., C. Nonnengaesser, et al. (1986). "Trypanosoma brucei: cis-aconitate and temperature reduction as triggers of synchronous transformation of bloodstream to procyclic trypomastigotes in vitro." Exp Parasitol **62**(2): 283-291.

Delaglio, F., S. Grzesiek, et al. (1995). "NMRPipe: a multidimensional spectral processing system based on UNIX pipes." J Biomol NMR **6**(3): 277-293.

Dilbeck, V., M. Berberof, et al. (1999). "Characterization of a coiled coil protein present in the basal body of *Trypanosoma brucei*." J Cell Sci **112 (Pt 24)**: 4687-4694.

Doherty, G. J. and H. T. McMahon (2009). "Mechanisms of Endocytosis." Annual Review of Biochemistry **78**(1): 857-902.

Domenicali Pfister, D., G. Burkard, et al. (2006). "A Mitogen-activated protein kinase controls differentiation of bloodstream forms of *Trypanosoma brucei*." Eukaryot Cell **5**(7): 1126-1135.

Edeling, M. A., C. Smith, et al. (2006). "Life of a clathrin coat: insights from clathrin and AP structures." Nat Rev Mol Cell Biol **7**(1): 32-44.

Emsley, P. and K. Cowtan (2004). "Coot: model-building tools for molecular graphics." Acta Crystallogr D Biol Crystallogr **60**(Pt 12 Pt 1): 2126-2132.

Esson, H. J., B. Morriswood, et al. (2012). "Morphology of the trypanosome bilobe, a novel cytoskeletal structure." Eukaryot Cell **11**(6): 761-772.

Evans, P. (2006). "Scaling and assessment of data quality." Acta Crystallogr D Biol Crystallogr **62**(Pt 1): 72-82.

Fenn, K. and K. R. Matthews (2007). "The cell biology of *Trypanosoma brucei* differentiation." Curr Opin Microbiol **10**(6): 539-546.

Fernandez-Borja, M., R. Wubbolts, et al. (1999). "Multivesicular body morphogenesis requires phosphatidyl-inositol 3-kinase activity." Curr Biol **9**(1): 55-58.

Field, M. C. and M. Carrington (2009). "The trypanosome flagellar pocket." Nat Rev Microbiol **7**(11): 775-786.

Gadelha, C., S. Rothery, et al. (2009). "Membrane domains and flagellar pocket boundaries are influenced by the cytoskeleton in African trypanosomes." Proc Natl Acad Sci U S A **106**(41): 17425-17430.

Gallo, J.-M., E. Précigout, et al. (1988). "Subcellular sequestration of an antigenically unique β -tubulin." Cell Motility and the Cytoskeleton **9**(2): 175-183.

Garrett, D. S., J. Kuszewski, et al. (1994). "The impact of direct refinement against three-bond HN-C α H coupling constants on protein structure determination by NMR." J Magn Reson B **104**(1): 99-103.

Gibson, W., L. Peacock, et al. (2006). "Analysis of a cross between green and red fluorescent trypanosomes." Biochem Soc Trans **34**(Pt 4): 557-559.

Ginger, M. L., E. S. Ngazoa, et al. (2005). "Intracellular positioning of isoforms explains an unusually large adenylate kinase gene family in the parasite *Trypanosoma brucei*." J Biol Chem **280**(12): 11781-11789.

Goldshmidt, H., D. Matas, et al. (2010). "Persistent ER stress induces the spliced leader RNA silencing pathway (SLS), leading to programmed cell death in *Trypanosoma brucei*." PLoS Pathog **6**(1): e1000731.

Gonzalez Jr, L. and R. H. Scheller (1999). "Regulation of Membrane Trafficking: Structural Insights from a Rab/Effector Complex." Cell **96**(6): 755-758.

Grunfelder, C. G., M. Engstler, et al. (2003). "Endocytosis of a glycosylphosphatidylinositol-anchored protein via clathrin-coated vesicles, sorting by default in endosomes, and exocytosis via RAB11-positive carriers." Mol Biol Cell **14**(5): 2029-2040.

Grzesiek, S., H. Dobeli, et al. (1992). " ^1H , ^{13}C , and ^{15}N NMR backbone assignments and secondary structure of human interferon-gamma." Biochemistry **31**(35): 8180-8190.

Gull, K. (2003). "Host-parasite interactions and trypanosome morphogenesis: a flagellar pocketful of goodies." Current Opinion in Microbiology **6**(4): 365-370.

Hall, B. S., C. Gabernet-Castello, et al. (2006). "TbVps34, the trypanosome orthologue of Vps34, is required for Golgi complex segregation." J Biol Chem **281**(37): 27600-27612.

Han, B. G., M. Han, et al. (2002). "Crystal structure of human calmodulin-like protein: insights into its functional role." FEBS Lett **521**(1-3): 24-30.

Headd, J. J., N. Echols, et al. (2012). "Use of knowledge-based restraints in phenix.refine to improve macromolecular refinement at low resolution." Acta Crystallogr D Biol Crystallogr **68**(Pt 4): 381-390.

Hendrickson, W. A. (1976). "Radiation damage in protein crystallography." J Mol Biol **106**(3): 889-893.

Herman, P. K. and S. D. Emr (1990). "Characterization of VPS34, a gene required for vacuolar protein sorting and vacuole segregation in *Saccharomyces cerevisiae*." Mol Cell Biol **10**(12): 6742-6754.

Hirano, Y., S. Yoshinaga, et al. (2005). "Structure of a cell polarity regulator, a complex between atypical PKC and Par6 PB1 domains." J Biol Chem **280**(10): 9653-9661.

Holm, L. and P. Rosenstrom (2010). "Dali server: conservation mapping in 3D." Nucleic Acids Res **38**(Web Server issue): W545-549.

Hung, C. H., X. Qiao, et al. (2004). "Clathrin-dependent targeting of receptors to the flagellar pocket of procyclic-form *Trypanosoma brucei*." Eukaryot Cell **3**(4): 1004-1014.

Iten, M., H. Mett, et al. (1997). "Alterations in ornithine decarboxylase characteristics account for tolerance of *Trypanosoma brucei rhodesiense* to D,L-alpha-difluoromethylornithine." Antimicrob Agents Chemother **41**(9): 1922-1925.

Jacobs, R. T., B. Nare, et al. (2011). "SCYX-7158, an Orally-Active Benzoxaborole for the Treatment of Stage 2 Human African Trypanosomiasis." Plos Neglected Tropical Diseases **5**(6).

Jeffries, T. R., G. W. Morgan, et al. (2001). "A developmentally regulated rab11 homologue in *Trypanosoma brucei* is involved in recycling processes." J Cell Sci **114**(Pt 14): 2617-2626.

Jones, D. T. (1999). "Protein secondary structure prediction based on position-specific scoring matrices." J Mol Biol **292**(2): 195-202.

Kabiri, M. and D. Steverding (2000). "Studies on the recycling of the transferrin receptor in *Trypanosoma brucei* using an inducible gene expression system." Eur J Biochem **267**(11): 3309-3314.

Kaiser, M., M. A. Bray, et al. (2011). "Antitrypanosomal activity of fexinidazole, a new oral nitroimidazole drug candidate for treatment of sleeping sickness." Antimicrob Agents Chemother **55**(12): 5602-5608.

Karle, J. (1980). "Some developments in anomalous dispersion for the structural investigation of macromolecular systems in biology." International Journal of Quantum Chemistry **18**(S7): 357-367.

Kay, L. E., M. Ikura, et al. (1990). "Three-dimensional triple-resonance NMR spectroscopy of isotopically enriched proteins." Journal of Magnetic Resonance (1969) **89**(3): 496-514.

King, S. M. (2003). "Organization and regulation of the dynein microtubule motor." Cell Biol Int **27**(3): 213-215.

Klingbeil, M. M., M. E. Drew, et al. (2001). "Unlocking the secrets of trypanosome kinetoplast DNA network replication." Protist **152**(4): 255-262.

Koradi, R., M. Billeter, et al. (1996). "MOLMOL: a program for display and analysis of macromolecular structures." J Mol Graph **14**(1): 51-55, 29-32.

Lacomble, S., S. Vaughan, et al. (2009). "Three-dimensional cellular architecture of the flagellar pocket and associated cytoskeleton in trypanosomes revealed by electron microscope tomography." J Cell Sci **122**(Pt 8): 1081-1090.

Lacomble, S., S. Vaughan, et al. (2010). "Basal body movements orchestrate membrane organelle division and cell morphogenesis in *Trypanosoma brucei*." J Cell Sci **123**(Pt 17): 2884-2891.

LaCount, D. J., B. Barrett, et al. (2002). "Trypanosoma brucei FLA1 is required for flagellum attachment and cytokinesis." J Biol Chem **277**(20): 17580-17588.

LaCount, D. J., S. Bruse, et al. (2000). "Double-stranded RNA interference in Trypanosoma brucei using head-to-head promoters." Mol Biochem Parasitol **111**(1): 67-76.

Lamaze, C., A. Dujeancourt, et al. (2001). "Interleukin 2 receptors and detergent-resistant membrane domains define a clathrin-independent endocytic pathway." Mol Cell **7**(3): 661-671.

Landfear, S. M. and M. Ignatushchenko (2001). "The flagellum and flagellar pocket of trypanosomatids." Mol Biochem Parasitol **115**(1): 1-17.

Laskowski, R. A., M. W. MacArthur, et al. (1993). "PROCHECK: a program to check the stereochemical quality of protein structures." Journal of Applied Crystallography **26**(2): 283-291.

Lewit-Bentley, A. and S. Rety (2000). "EF-hand calcium-binding proteins." Current Opinion in Structural Biology **10**(6): 637-643.

Linding, R., R. B. Russell, et al. (2003). "GlobPlot: Exploring protein sequences for globularity and disorder." Nucleic Acids Res **31**(13): 3701-3708.

Louis, F. J. and P. P. Simarro (2005). "[Rough start for the fight against sleeping sickness in French equatorial Africa]." Med Trop (Mars) **65**(3): 251-257.

Maga, J. A. and J. H. LeBowitz (1999). "Unravelling the kinetoplastid paraflagellar rod." Trends Cell Biol **9**(10): 409-413.

Malvy, D. and F. Chappuis (2011). "Sleeping sickness." Clin Microbiol Infect **17**(7): 986-995.

Marion, D., P. C. Driscoll, et al. (1989). "Overcoming the overlap problem in the assignment of proton NMR spectra of larger proteins by use of three-dimensional heteronuclear proton-nitrogen-15 Hartmann-Hahn-multiple quantum coherence and nuclear Overhauser-multiple quantum coherence spectroscopy: application to interleukin 1.beta." Biochemistry **28**(15): 6150-6156.

Martin, M. B., J. S. Grimley, et al. (2001). "Bisphosphonates inhibit the growth of *Trypanosoma brucei*, *Trypanosoma cruzi*, *Leishmania donovani*, *Toxoplasma gondii*, and *Plasmodium falciparum*: a potential route to chemotherapy." J Med Chem **44**(6): 909-916.

Mayor, S. and H. Riezman (2004). "Sorting GPI-anchored proteins." Nat Rev Mol Cell Biol **5**(2): 110-120.

McConville, M. J., K. A. Mullin, et al. (2002). "Secretory pathway of trypanosomatid parasites." Microbiol Mol Biol Rev **66**(1): 122-154; table of contents.

McKean, P. G., A. Baines, et al. (2003). "Gamma-tubulin functions in the nucleation of a discrete subset of microtubules in the eukaryotic flagellum." Curr Biol **13**(7): 598-602.

Mehlert, A., M. R. Wormald, et al. (2012). "Modeling of the N-glycosylated transferrin receptor suggests how transferrin binding can occur within the surface coat of *Trypanosoma brucei*." PLoS Pathog **8**(4): e1002618.

Melville, S. E., V. Leech, et al. (1998). "The molecular karyotype of the megabase chromosomes of *Trypanosoma brucei* and the assignment of chromosome markers." Mol Biochem Parasitol **94**(2): 155-173.

Messerschmidt, A. (2007). Molecular Replacement. X-Ray Crystallography of Biomacromolecules, Wiley-VCH Verlag GmbH & Co. KGaA: 261-266.

Metcalf, B. W., P. Bey, et al. (1978). "Catalytic Irreversible Inhibition of Mammalian Ornithine Decarboxylase (E C 4 1 1 17) by Substrate and Product Analogs." Journal of the American Chemical Society **100**(8): 2551-2553.

Molla-Herman, A., C. Boularan, et al. (2008). "Targeting of beta-arrestin2 to the centrosome and primary cilium: role in cell proliferation control." PLoS One **3**(11): e3728.

Molla-Herman, A., R. Ghossoub, et al. (2010). "The ciliary pocket: an endocytic membrane domain at the base of primary and motile cilia." J Cell Sci **123**(Pt 10): 1785-1795.

Morgan, G. W., P. W. Denny, et al. (2005). "An evolutionarily conserved coiled-coil protein implicated in polycystic kidney disease is involved in basal body duplication and flagellar biogenesis in *Trypanosoma brucei*." Mol Cell Biol **25**(9): 3774-3783.

Morriswood, B., K. Havlicek, et al. (2013). "Novel bilobe components in *Trypanosoma brucei* identified using proximity-dependent biotinylation." Eukaryot Cell **12**(2): 356-367.

Morriswood, B., C. Y. He, et al. (2009). "The bilobe structure of *Trypanosoma brucei* contains a MORN-repeat protein." Mol Biochem Parasitol **167**(2): 95-103.

Mussmann, R., M. Engstler, et al. (2004). "Factors affecting the level and localization of the transferrin receptor in *Trypanosoma brucei*." J Biol Chem **279**(39): 40690-40698.

Ngan, C. H., D. R. Hall, et al. (2012). "FTSite: high accuracy detection of ligand binding sites on unbound protein structures." Bioinformatics **28**(2): 286-287.

Nichols, B. J. and J. Lippincott-Schwartz (2001). "Endocytosis without clathrin coats." Trends Cell Biol **11**(10): 406-412.

O'Beirne, C., C. M. Lowry, et al. (1998). "Both IgM and IgG anti-VSG antibodies initiate a cycle of aggregation-disaggregation of bloodstream forms of *Trypanosoma brucei* without damage to the parasite." Mol Biochem Parasitol **91**(1): 165-193.

Oberholzer, M., G. Langousis, et al. (2011). "Independent analysis of the flagellum surface and matrix proteomes provides insight into flagellum signaling in mammalian-infectious *Trypanosoma brucei*." Mol Cell Proteomics **10**(10): M111 010538.

Oberholzer, M., G. Marti, et al. (2007). "The *Trypanosoma brucei* cAMP phosphodiesterases TbrPDEB1 and TbrPDEB2: flagellar enzymes that are essential for parasite virulence." FASEB J **21**(3): 720-731.

Ogbadoyi, E., K. Ersfeld, et al. (2000). "Architecture of the *Trypanosoma brucei* nucleus during interphase and mitosis." Chromosoma **108**(8): 501-513.

Ogbadoyi, E. O., D. R. Robinson, et al. (2003). "A high-order trans-membrane structural linkage is responsible for mitochondrial genome positioning and segregation by flagellar basal bodies in trypanosomes." Mol Biol Cell **14**(5): 1769-1779.

Overath, P., J. Czichos, et al. (1986). "The effect of citrate/cis-aconitate on oxidative metabolism during transformation of *Trypanosoma brucei*." Eur J Biochem **160**(1): 175-182.

Overath, P. and M. Engstler (2004). "Endocytosis, membrane recycling and sorting of GPI-anchored proteins: *Trypanosoma brucei* as a model system." Mol Microbiol **53**(3): 735-744.

Pal, A., B. S. Hall, et al. (2003). "Rab5 and Rab11 mediate transferrin and anti-variant surface glycoprotein antibody recycling in *Trypanosoma brucei*." Biochem J **374**(Pt 2): 443-451.

Pal, A., B. S. Hall, et al. (2002). "Differential endocytic functions of *Trypanosoma brucei* Rab5 isoforms reveal a glycosylphosphatidylinositol-specific endosomal pathway." J Biol Chem **277**(11): 9529-9539.

Papermaster, D. S., B. G. Schneider, et al. (1985). "Vesicular transport of newly synthesized opsin from the Golgi apparatus toward the rod outer segment. Ultrastructural immunocytochemical and autoradiographic evidence in *Xenopus* retinas." Invest Ophthalmol Vis Sci **26**(10): 1386-1404.

Peck, R. F., A. M. Shiflett, et al. (2008). "The LAMP-like protein p67 plays an essential role in the lysosome of African trypanosomes." Mol Microbiol **68**(4): 933-946.

Pradel, L. C., M. Bonhivers, et al. (2006). "NIMA-related kinase TbNRKC is involved in basal body separation in *Trypanosoma brucei*." J Cell Sci **119**(Pt 9): 1852-1863.

Priotto, G., S. Kasparian, et al. (2009). "Nifurtimox-eflornithine combination therapy for second-stage African *Trypanosoma brucei* gambiense trypanosomiasis: a multicentre, randomised, phase III, non-inferiority trial." Lancet **374**(9683): 56-64.

Qiao, X., B. F. Chuang, et al. (2006). "Sorting signals required for trafficking of the cysteine-rich acidic repetitive transmembrane protein in *Trypanosoma brucei*." Eukaryot Cell **5**(8): 1229-1242.

Ralston, K. S. and K. L. Hill (2008). "The flagellum of *Trypanosoma brucei*: new tricks from an old dog." Int J Parasitol **38**(8-9): 869-884.

Ralston, K. S., Z. P. Kabututu, et al. (2009). "The *Trypanosoma brucei* flagellum: moving parasites in new directions." Annu Rev Microbiol **63**: 335-362.

Robinson, D. R. and K. Gull (1991). "Basal body movements as a mechanism for mitochondrial genome segregation in the trypanosome cell cycle." Nature **352**(6337): 731-733.

Rogers, D. J., G. Hendrickx, et al. (1994). "Tsetse flies and their control." Rev Sci Tech **13**(4): 1075-1124.

Rohatgi, R. and W. J. Snell (2010). "The ciliary membrane." Curr Opin Cell Biol **22**(4): 541-546.

Rolin, S., J. Hancocq-Quertier, et al. (1998). "Mild acid stress as a differentiation trigger in *Trypanosoma brucei*." Mol Biochem Parasitol **93**(2): 251-262.

Rule, G. S. and T. K. Hitchens (2006). Fundamentals of Protein NMR Spectroscopy. Netherlands, Springer.

Rupp, B. (2010). Biomolecular crystallography: principles, practice, and application to structural biology, Garland Science.

Russell, D. G., R. J. Newsam, et al. (1983). "Structural and biochemical characterisation of the paraflagellar rod of *Crithidia fasciculata*." Eur J Cell Biol **30**(1): 137-143.

Sbicego, S., E. Vassella, et al. (1999). "The use of transgenic *Trypanosoma brucei* to identify compounds inducing the differentiation of bloodstream forms to procyclic forms." Mol Biochem Parasitol **104**(2): 311-322.

Schwieters, C. D., J. J. Kuszewski, et al. (2003). "The Xplor-NIH NMR molecular structure determination package." J Magn Reson **160**(1): 65-73.

Shapiro, S. Z., J. Naessens, et al. (1984). "Analysis by flow cytometry of DNA synthesis during the life cycle of African trypanosomes." Acta Trop **41**(4): 313-323.

Shapiro, T. A. and P. T. Englund (1995). "The structure and replication of kinetoplast DNA." Annu Rev Microbiol **49**: 117-143.

Shen, Y., F. Delaglio, et al. (2009). "TALOS+: a hybrid method for predicting protein backbone torsion angles from NMR chemical shifts." J Biomol NMR **44**(4): 213-223.

Sherwin, T. and K. Gull (1989). "The cell division cycle of *Trypanosoma brucei brucei*: timing of event markers and cytoskeletal modulations." Philos Trans R Soc Lond B Biol Sci **323**(1218): 573-588.

Shi, J., J. B. Franklin, et al. (2008). "Centrin4 coordinates cell and nuclear division in *T. brucei*." J Cell Sci **121**(Pt 18): 3062-3070.

Simarro, P. P., G. Cecchi, et al. (2011). "Risk for human African trypanosomiasis, Central Africa, 2000-2009." Emerg Infect Dis **17**(12): 2322-2324.

Simarro, P. P., A. Diarra, et al. (2011). "The human African trypanosomiasis control and surveillance programme of the World Health Organization 2000-2009: the way forward." PLoS Negl Trop Dis **5**(2): e1007.

Smith, D. H., J. Pepin, et al. (1998). "Human African trypanosomiasis: an emerging public health crisis." Br Med Bull **54**(2): 341-355.

Smith, E. F. and P. Yang (2004). "The radial spokes and central apparatus: mechanochemical transducers that regulate flagellar motility." Cell Motil Cytoskeleton **57**(1): 8-17.

Sorokin, S. (1962). "Centrioles and the formation of rudimentary cilia by fibroblasts and smooth muscle cells." J Cell Biol **15**: 363-377.

Strub, M. P., F. Hoh, et al. (2003). "Selenomethionine and selenocysteine double labeling strategy for crystallographic phasing." Structure **11**(11): 1359-1367.

Szoor, B., J. Wilson, et al. (2006). "Protein tyrosine phosphatase TbPTP1: A molecular switch controlling life cycle differentiation in trypanosomes." J Cell Biol **175**(2): 293-303.

Teng, Q. (2005). Structural Biology: Practical NMR Applications. New York, Springer.

Terwilliger, T. C., P. D. Adams, et al. (2009). "Decision-making in structure solution using Bayesian estimates of map quality: the PHENIX AutoSol wizard." Acta Crystallogr D Biol Crystallogr **65**(Pt 6): 582-601.

Tetley, L. and K. Vickerman (1985). "Differentiation in *Trypanosoma brucei*: host-parasite cell junctions and their persistence during acquisition of the variable antigen coat." J Cell Sci **74**: 1-19.

Van Den Abbeele, J., Y. Claes, et al. (1999). "Trypanosoma brucei spp. development in the tsetse fly: characterization of the post-mesocyclic stages in the foregut and proboscis." Parasitology **118 (Pt 5)**: 469-478.

Vanhamme, L., F. Paturiaux-Hanocq, et al. (2003). "Apolipoprotein L-I is the trypanosome lytic factor of human serum." Nature **422(6927)**: 83-87.

Vanhollebeke, B., G. De Muylder, et al. (2008). "A haptoglobin-hemoglobin receptor conveys innate immunity to *Trypanosoma brucei* in humans." Science **320(5876)**: 677-681.

Vassella, E., R. Kramer, et al. (2001). "Deletion of a novel protein kinase with PX and FYVE-related domains increases the rate of differentiation of *Trypanosoma brucei*." Mol Microbiol **41(1)**: 33-46.

Vassella, E., B. Reuner, et al. (1997). "Differentiation of African trypanosomes is controlled by a density sensing mechanism which signals cell cycle arrest via the cAMP pathway." J Cell Sci **110 (Pt 21)**: 2661-2671.

Vaughan, S., L. Kohl, et al. (2008). "A repetitive protein essential for the flagellum attachment zone filament structure and function in *Trypanosoma brucei*." Protist **159(1)**: 127-136.

Wirtz, E., S. Leal, et al. (1999). "A tightly regulated inducible expression system for conditional gene knock-outs and dominant-negative genetics in *Trypanosoma brucei*." Mol Biochem Parasitol **99(1)**: 89-101.

Woods, K., N. Nic a'Bhaird, et al. (2013). "Identification and characterization of a stage specific membrane protein involved in flagellar attachment in *Trypanosoma brucei*." PLoS One **8(1)**: e52846.

Wuthrich, K. (1995). "NMR - this other method for protein and nucleic acid structure determination." Acta Crystallogr D Biol Crystallogr **51(Pt 3)**: 249-270.

Yelinek, J. T., C. Y. He, et al. (2009). "Ultrastructural study of Golgi duplication in *Trypanosoma brucei*." Traffic **10(3)**: 300-306.

Zerial, M. and H. McBride (2001). "Rab proteins as membrane organizers." Nat Rev Mol Cell Biol **2**(2): 107-117.

Zhao, Z., M. E. Lindsay, et al. (2008). "p166, a link between the trypanosome mitochondrial DNA and flagellum, mediates genome segregation." EMBO J **27**(1): 143-154.

Zheng, C., H. H. Liu, et al. (2010). "EF-hand domains of MCFD2 mediate interactions with both LMAN1 and coagulation factor V or VIII." Blood **115**(5): 1081-1087.

Zhou, Q., B. H. Liu, et al. (2011). "A coiled-coil- and C2-domain-containing protein is required for FAZ assembly and cell morphology in *Trypanosoma brucei*." Journal of Cell Science **124**(22): 3848-3858.

Ziegelbauer, K. and P. Overath (1993). "Organization of two invariant surface glycoproteins in the surface coat of *Trypanosoma brucei*." Infect Immun **61**(11): 4540-4545.

Appendix

Table 3 Chemical shift assignment of TbBILB01-NTD

Residue	Atom	Atom type	Shift	Error
1	c	¹³ C	174.686	0.062
1	ca	¹³ C	53.728	0.291
1	cb	¹³ C	32.523	0.012
1	ce	¹³ C	15.861	0.009
1	ha	¹ H	4.502	0.155
1	hb#	¹ H	2.013	0.004
1	he#	¹ H	2.098	0.003
1	hg#	¹ H	2.261	0
1	hn	¹ H	8.321	0.02
1	n	¹⁵ N	121.043	0.141
2	c	¹³ C	175.678	0.041
2	ca	¹³ C	51.309	0.187
2	cb	¹³ C	19.171	0.19
2	ha	¹ H	4.407	0.058
2	hb#	¹ H	1.304	0.011
2	hn	¹ H	7.914	0.022
2	n	¹⁵ N	123.848	0.192
3	c	¹³ C	173.742	0.006
3	ca	¹³ C	56.25	0.619
3	cb	¹³ C	39.93	0.485
3	ha	¹ H	4.605	0.045
3	hb#	¹ H	2.602	0.012
3	he#	¹ H	7.482	0.005

3	hn	1H	9.06	0.024
3	n	15N	124.636	0.131
4	c	13C	176.58	0.005
4	ca	13C	52.724	0.11
4	cb	13C	44.199	0.099
4	cd1	13C	24.098	0.205
4	cd2	13C	23.37	0.116
4	cg	13C	26.816	0.029
4	ha	1H	5.622	0.029
4	hb	1H	1.59	0.008
4	hb1	1H	1.632	0.026
4	hb2	1H	1.247	0.021
4	hd1#	1H	0.756	0.019
4	hd2#	1H	0.762	0.027
4	hg	1H	1.661	0.009
4	hn	1H	8.466	0.015
4	n	15N	130.373	0.195
5	c	13C	173.306	0.015
5	ca	13C	59.186	0.168
5	cb	13C	35.148	0.174
5	cg1	13C	21.91	0.082
5	cg2	13C	20.14	0.069
5	ha	1H	4.508	0.019
5	hb	1H	2.157	0.015
5	hg1#	1H	1.152	0.014
5	hg2#	1H	1.074	0.016
5	hn	1H	8.75	0.027
5	n	15N	114.967	0.162
6	c	13C	175.328	0.029
6	ca	13C	53.721	0.2
6	cb	13C	31.301	0.208
6	ha	1H	5.235	0.013

6	he1	1H	6.398	0.006
6	he2	1H	6.472	0.009
6	hn	1H	8.596	0.017
6	n	15N	122.337	0.184
6	ne	15N	108.51	0.001
7	c	13C	172.224	0.013
7	ca	13C	59.154	0.157
7	cb	13C	33.347	0.245
7	cg#	13C	19.937	0.144
7	ha	1H	4.719	0.023
7	hb	1H	2.037	0.016
7	hg#	1H	1.011	0.013
7	hn	1H	9.634	0.027
7	n	15N	119.805	0.278
8	c	13C	174.92	0.01
8	ca	13C	48.242	0.158
8	cb	13C	22.037	0.14
8	ha	1H	6.069	0.018
8	hb#	1H	1.402	0.021
8	hn	1H	8.323	0.023
8	n	15N	127.863	0.223
9	c	13C	175.484	0
9	ca	13C	50.127	0.165
9	cb	13C	20.418	0.133
9	ha	1H	3.724	0.013
9	hb#	1H	0.154	0.009
9	hn	1H	7.931	0.04
9	n	15N	115.648	0.252
10	ca	13C	53.559	0.052
10	cb	13C	42.983	0.139
10	ha	1H	4.781	0
10	hb1	1H	2.584	0.013

10	hb2	1H	2.237	0.01
10	hn	1H	7.8	0.056
10	n	15N	119.695	0.221
11	ca	13C	65.694	0.103
11	cb	13C	36.145	0.055
11	cd1	13C	8.632	0.098
11	cg2	13C	16.918	0.104
11	ha	1H	3.791	0.474
11	hb	1H	1.993	0.015
11	hd1#	1H	0.464	0.056
11	hg2#	1H	0.813	0.019
11	hn	1H	8.601	0.018
11	n	15N	119.99	0.271
12	ca	13C	60.254	0
12	cb	13C	40.503	0
13	c	13C	173.971	0.003
13	ca	13C	53.742	1.13
13	cb	13C	37.74	0.108
13	hn	1H	9.637	0.014
13	n	15N	126.142	0.054
14	c	13C	172.907	0.058
14	ca	13C	51.447	0.152
14	cb	13C	41.145	0.328
14	ha	1H	5.086	0.012
14	hb#	1H	2.657	0.026
14	hd1	1H	7.004	0.009
14	hd2	1H	7.764	0.015
14	hn	1H	8.261	0.017
14	n	15N	117.599	0.237
14	nd	15N	115.356	0.182
15	c	13C	175.216	0.007
15	ca	13C	54.23	0.122

15	cb	13C	31.751	0.184
15	ha	1H	4.814	0.037
15	hn	1H	8.35	0.015
15	n	15N	123.014	0.168
16	c	13C	173.177	0.015
16	ca	13C	59.373	0.101
16	cb	13C	33.186	0.096
16	cg1	13C	20.356	0.056
16	cg2	13C	20.052	0.087
16	ha	1H	4.156	0.017
16	hb	1H	1.606	0.015
16	hg1#	1H	0.495	0.015
16	hg2#	1H	0.662	0.009
16	hn	1H	8.642	0.014
16	n	15N	123.989	0.079
17	c	13C	174.527	0
17	ca	13C	50.363	0.112
17	cb	13C	40.665	0.168
17	ha	1H	5.476	0.013
17	hb1	1H	2.753	0.012
17	hb2	1H	2.127	0.027
17	hd1	1H	6.926	0.006
17	hd2	1H	7.424	0.009
17	hn	1H	7.617	0.014
17	n	15N	119.87	0.275
17	nd	15N	109.077	0.081
18	c	13C	174.816	0.04
18	ca	13C	52.231	0.263
18	cb	13C	41.159	0.174
18	ce#	13C	130.634	0.083
18	cz	13C	127.989	0.028
18	ha	1H	6.173	0.025

18	hb#	1H	2.59	0.028
18	he#	1H	7.41	0.008
18	hn	1H	9.547	0.015
18	hz	1H	7.073	0.008
18	n	15N	126.021	0.17
19	c	13C	174.617	0.013
19	ca	13C	53.842	0.122
19	cb	13C	30.919	0.025
19	ha	1H	4.649	0.012
19	hn	1H	8.404	0.018
19	n	15N	121.898	0.137
20	c	13C	174.463	0.028
20	ca	13C	52.261	0.157
20	cb	13C	42.543	0.143
20	cd#	13C	20.704	0.088
20	cg	13C	24.904	0.147
20	ha	1H	4.573	0.017
20	hb1	1H	1.745	0.023
20	hb2	1H	1.194	0.012
20	hd#	1H	0.568	0.053
20	hg	1H	0.771	0.013
20	hn	1H	9.108	0.019
20	n	15N	126.961	0.173
21	c	13C	173.461	0
21	ca	13C	55.146	0.158
21	cb	13C	64.085	0.141
21	ha	1H	5.229	0.013
21	hb#	1H	3.503	0.012
21	hn	1H	7.709	0.023
21	n	15N	113.881	0.178
22	c	13C	173.453	0
22	ca	13C	54.169	0.19

22	cb	13C	40.912	0.276
22	cd#	13C	130.99	0.025
22	ce#	13C	133.184	0.009
22	cz	13C	128.686	0.056
22	ha	1H	4.996	0.041
22	hb#	1H	2.992	0.023
22	hd#	1H	7.188	0.009
22	he#	1H	7.497	0.005
22	hn	1H	9.126	0.024
22	hz	1H	7.154	0.045
22	n	15N	123.976	0.138
26	c	13C	174.963	0.041
26	ca	13C	61.148	0.076
26	cb	13C	30.808	0
27	c	13C	175.918	0.041
27	ca	13C	55.568	0.141
27	cb	13C	63.92	0.169
27	ha	1H	4.506	0.014
27	hb#	1H	3.959	0.01
27	hn	1H	7.741	0.017
27	n	15N	110.428	0.166
28	ca	13C	63.659	0.125
28	cb	13C	34.788	0.072
28	cd1	13C	9.328	0.077
28	cg1	13C	28.136	0.111
28	cg2	13C	16.043	0.091
28	ha	1H	3.586	0.013
28	hb	1H	1.947	0.011
28	hd1#	1H	0.562	0.121
28	hg11	1H	1.511	0.014
28	hg12	1H	1.175	0.011
28	hg2#	1H	0.838	0.009

28	hn	1H	9.182	0.031
28	n	15N	121.549	0.184
29	c	13C	176.793	0
29	ca	13C	56.264	2.352
29	cb	13C	63.105	0.204
29	ha	1H	4.436	0.022
29	hb#	1H	3.801	0.025
29	hn	1H	7.445	0.015
29	n	15N	107.809	0.192
30	c	13C	179.372	0.002
30	ca	13C	57.998	0.154
30	cb	13C	28.931	0.18
30	cg	13C	35.085	0.144
30	ha	1H	4.08	0.014
30	hb#	1H	1.982	0.018
30	hg#	1H	2.326	0.021
30	hn	1H	7.89	0.021
30	n	15N	124.633	0.154
31	c	13C	177.844	0.03
31	ca	13C	57.285	0.166
31	cb	13C	41.171	0.145
31	cd1	13C	25.145	0.141
31	cd2	13C	23.487	0.098
31	cg	13C	26.27	0.221
31	ha	1H	4.057	0.019
31	hb1	1H	1.9	0.02
31	hb2	1H	1.184	0.012
31	hd1#	1H	0.815	0.016
31	hd2#	1H	0.85	0.024
31	hg	1H	1.484	0.014
31	hn	1H	8.49	0.019
31	n	15N	122.222	0.158

32	c	13C	175.673	0.008
32	ca	13C	67.118	0.114
32	cb	13C	67.904	0.009
32	cg	13C	19.762	0.048
32	ha	1H	3.62	0.01
32	hb	1H	4.32	0.022
32	hg#	1H	1.262	0.015
32	hn	1H	8.519	0.018
32	n	15N	115.628	0.159
33	c	13C	179.408	0
33	ca	13C	58.612	0.205
33	cb	13C	29.372	0
33	cd	13C	42.173	0.04
33	ha	1H	4.278	0.015
33	hd#	1H	3.283	0.008
33	he	1H	7.192	0.001
33	hn	1H	8.052	0.017
33	n	15N	121.04	0.175
34	ca	13C	61.152	0.138
34	cb	13C	62.359	0.248
34	ha	1H	4.255	0.024
34	hn	1H	8.112	0.023
34	n	15N	115.412	0.245
35	c	13C	177.713	0.029
35	ca	13C	54.325	0.135
35	cb	13C	16.006	0.119
35	ha	1H	3.687	0.009
35	hb#	1H	1.412	0.009
35	hn	1H	8.728	0.012
35	n	15N	124.071	0.188
36	c	13C	180.382	0.032
36	ca	13C	59.651	0.338

36	cg	13C	36.751	1.756
36	ha	1H	3.855	0.01
36	hg1	1H	2.387	0.017
36	hg2	1H	3.006	0.021
36	hn	1H	8.981	0.016
36	n	15N	116.036	0.138
37	c	13C	175.199	0.012
37	ca	13C	66.141	0.119
37	cb	13C	67.965	0.226
37	cg	13C	20.326	0.058
37	ha	1H	3.943	0.025
37	hb	1H	4.264	0.024
37	hg#	1H	1.201	0.005
37	hn	1H	8.317	0.025
37	n	15N	118.853	0.148
38	c	13C	180.402	0.013
38	ca	13C	54.058	0.134
38	cb	13C	16.346	0.163
38	ha	1H	3.959	0.015
38	hb#	1H	0.884	0.012
38	hn	1H	7.567	0.013
38	n	15N	123.902	0.173
39	c	13C	179.142	0.028
39	ca	13C	59.045	0.188
39	cb	13C	38.009	0.154
39	cd#	13C	130.277	0.047
39	ce#	13C	130.237	0.069
39	cz	13C	130.171	0.03
39	ha	1H	4.416	0.018
39	hb1	1H	1.799	0.012
39	hb2	1H	2.414	0.025
39	hd#	1H	6.185	0.126

39	he#	1H	6.837	0.017
39	hh	1H	6.744	0
39	hn	1H	8.508	0.015
39	hz	1H	6.649	0.016
39	n	15N	114.925	0.16
40	c	13C	176.669	0.008
40	ca	13C	62.659	0.427
40	cb	13C	61.809	0.119
40	ha	1H	4.388	0.021
40	hb#	1H	4.012	0.019
40	hn	1H	8.736	0.008
40	n	15N	118.703	0.144
41	c	13C	177.569	0.028
41	ca	13C	54.704	0.152
41	cb	13C	35.564	0.2
41	ha	1H	4.511	0.023
41	hb1	1H	2.666	0.014
41	hb2	1H	3.079	0.014
41	hd1	1H	6.696	0.006
41	hd2	1H	8.226	0.002
41	hn	1H	8.303	0.014
41	n	15N	124.178	0.163
41	nd	15N	113.173	0.092
42	ca	13C	58.133	0.146
42	cb	13C	28.179	0
42	ha	1H	4.5	0.02
42	hn	1H	8.026	0.015
42	n	15N	124.062	0.153
43	c	13C	177.564	0.005
43	ca	13C	65.865	0.043
43	cb	13C	37.377	0.095
43	cd1	13C	13.488	0.371

43	cg2	13C	15.368	0.055
43	ha	1H	4.314	0.038
43	hb	1H	1.904	0.027
43	hd1#	1H	0.747	0.01
43	hg2#	1H	0.536	0.01
43	hn	1H	8.592	0.024
43	n	15N	119.669	0.186
44	c	13C	176.824	0.006
44	ca	13C	60.378	0.193
44	cb	13C	60.909	0.773
44	ha	1H	4.144	0.041
44	hb#	1H	4.15	0.012
44	hn	1H	7.747	0.015
44	n	15N	112.036	0.165
45	c	13C	179.322	0.613
45	ca	13C	56.083	0.199
45	cb	13C	41.754	0.097
45	cd1	13C	23.739	0.183
45	cd2	13C	22.451	0.175
45	cg	13C	25.716	0.125
45	ha	1H	4.217	0.019
45	hb1	1H	1.896	0.013
45	hb2	1H	1.623	0.025
45	hd1#	1H	0.914	0.014
45	hd2#	1H	0.915	0.016
45	hg	1H	1.707	0.025
45	hn	1H	7.751	0.017
45	n	15N	119.868	0.172
46	c	13C	176.822	0.039
46	ca	13C	53.391	0.132
46	cb	13C	30.594	0.119
46	cd	13C	41.383	0.179

46	cg	13C	25.836	0.167
46	ha	1H	4.428	0.011
46	hb#	1H	1.962	0.014
46	hd#	1H	3.107	0.018
46	he	1H	7.093	0
46	hg#	1H	2.002	0.018
46	hn	1H	7.953	0.109
46	n	15N	115.109	0.185
47	c	13C	173.997	0
47	ca	13C	53.94	0.116
47	cb	13C	29.566	0.125
47	ha	1H	3.902	0.025
47	hb#	1H	1.889	0.011
47	he	1H	7.092	0.001
47	hn	1H	7.843	0.026
47	n	15N	122.194	0.171
48	c	13C	176.662	0.012
48	ca	13C	60.928	0.058
48	cb	13C	30.997	0.59
48	n	15N	114.814	0
49	c	13C	176.693	0.022
49	ca	13C	55.636	0.174
49	cb	13C	39.963	0.036
49	ha	1H	4.23	0.002
49	hn	1H	8.392	0.02
49	n	15N	118.162	0.144
50	c	13C	174.429	0.007
50	ca	13C	51.99	0.152
50	cb	13C	36.092	0.221
50	ha	1H	4.541	0.017
50	hb1	1H	2.711	0.028
50	hb2	1H	3.08	0.016

50	hd1	1H	6.743	0.003
50	hd2	1H	7.599	0.002
50	hn	1H	8.063	0.013
50	n	15N	112.476	0.258
51	c	13C	172.818	0
51	ca	13C	58.169	0.475
51	cb	13C	32.679	0.117
51	cg1	13C	20.528	0.061
51	cg2	13C	17.855	0.046
51	ha	1H	4.221	0.025
51	hb	1H	1.772	0.015
51	hg1#	1H	0.663	0.01
51	hg2#	1H	0.283	0.008
51	hn	1H	7.481	0.012
51	n	15N	124.117	0.154
52	c	13C	176.467	0
52	ca	13C	60.048	0.335
52	cb	13C	29.084	0.081
52	cd	13C	49.082	0.054
52	ha	1H	3.766	0.027
52	hb1	1H	1.086	0.012
52	hb2	1H	1.617	0.015
52	hd#	1H	3.568	0.04
52	n	15N	114.966	0
53	c	13C	173.891	0.004
53	ca	13C	58.77	0.083
53	cb	13C	62.327	0.29
53	ha	1H	4.766	0.011
53	hb#	1H	4.383	0.019
53	hn	1H	8.633	0.014
53	n	15N	116.636	0.156
54	c	13C	172.328	0.028

54	ca	13C	54.734	0.397
54	cb	13C	28.633	0.135
54	cd2	13C	119.511	0
54	ha	1H	4.838	0.022
54	hb#	1H	3.36	0.041
54	hd2	1H	7.157	0.007
54	hn	1H	7.535	0.019
54	n	15N	120.57	0.148
55	c	13C	174.168	0.003
55	ca	13C	53.348	0.168
55	cb	13C	33.649	0
55	ha	1H	4.407	0.006
55	hn	1H	8.705	0.03
55	n	15N	118.551	0.164
56	c	13C	174.223	0
56	ca	13C	56.19	0.118
56	cb	13C	36.387	0
56	ha	1H	4.616	0
56	hn	1H	8.945	0.011
56	n	15N	124.637	0.255
57	c	13C	172.694	0.128
57	ca	13C	53.483	0.135
57	cb	13C	30.798	0.122
57	cd2	13C	119.927	0.039
57	ce1	13C	138.694	0.038
57	ha	1H	4.794	0.002
57	hb	1H	2.782	0.005
57	hb1	1H	2.769	0.021
57	hb2	1H	2.989	0.019
57	hd2	1H	7.008	0.016
57	he1	1H	7.772	0.01
57	hn	1H	7.867	0.021

57	n	15N	127.585	0.159
58	c	13C	176.131	0
58	ca	13C	57.243	0.144
58	cb	13C	63.583	0.078
58	ha	1H	4.78	0.03
58	hb1	1H	3.773	0.012
58	hb2	1H	3.951	0.02
58	hn	1H	9.345	0.018
58	n	15N	117.49	0.161
59	c	13C	174.912	0.002
59	ca	13C	56.885	0.225
59	cb	13C	63.075	0.127
59	ha	1H	4.59	0.025
59	hb1	1H	3.775	0.021
59	hb2	1H	3.395	0.004
59	hn	1H	9.37	0.006
59	n	15N	120.126	0.161
60	c	13C	173.472	0.038
60	ca	13C	55.235	0.18
60	cb	13C	33.127	0.012
60	ha	1H	4.555	0.013
60	hn	1H	7.555	0.016
60	n	15N	120.064	0.163
61	c	13C	175.756	0.011
61	ca	13C	60.014	0.16
61	cb	13C	39.8	0.14
61	cd1	13C	12.243	0.125
61	cg2	13C	18.797	0.074
61	ha	1H	5.296	0.011
61	hb#	1H	1.896	0.018
61	hd1#	1H	0.892	0.012
61	hg2#	1H	1.091	0.013

61	hn	1H	8.841	0.029
61	n	15N	121.99	0.17
62	c	13C	174.282	0.006
62	ca	13C	53.515	0.191
62	cb	13C	36.751	0.159
62	cd	13C	28.796	0.186
62	ha	1H	5.598	0.016
62	hb#	1H	2.021	0.018
62	hd#	1H	1.664	0.018
62	hn	1H	9.53	0.03
62	n	15N	124.817	0.189
63	c	13C	174.111	0.008
63	ca	13C	52.843	0.089
63	cb	13C	37.451	0.081
63	ce	13C	17.512	0.022
63	cg	13C	30.749	0.095
63	ha	1H	5.587	0.014
63	hb#	1H	2.235	0.012
63	he#	1H	2.15	0.006
63	hg#	1H	2.24	0.013
63	hn	1H	10.034	0.018
63	n	15N	121.957	0.171
64	c	13C	173.302	0
64	ca	13C	57.562	0.241
64	cb	13C	35.197	0.111
64	cd	13C	132.427	0.017
64	cd#	13C	132.307	0
64	ce#	13C	117.204	0.005
64	ha	1H	3.674	0.013
64	hb	1H	0.72	0.012
64	hd#	1H	5.616	0.01
64	he#	1H	6.388	0.006

64	hn	1H	8.714	0.016
64	n	15N	129.415	0.165
65	c	13C	176.009	0.025
65	ca	13C	52.015	0.146
65	cb	13C	41.323	0.151
65	ha	1H	4.521	0.008
65	hb#	1H	2.205	0.008
65	hn	1H	8.25	0.014
65	n	15N	131.284	0.169
66	c	13C	177.495	0.019
66	ca	13C	57.272	0.123
66	cb	13C	28.77	0.113
66	cg	13C	35.324	0.113
66	ha	1H	3.74	0.016
66	hb#	1H	2.164	0.052
66	hg#	1H	2.352	0.037
66	hn	1H	8.608	0.024
66	n	15N	125.474	0.18
67	c	13C	178.509	0.004
67	ca	13C	57.122	0.303
67	cb	13C	28.452	0.195
67	cg	13C	35.276	0.069
67	ha	1H	4.121	0.013
67	hb#	1H	2.111	0.021
67	hg#	1H	2.279	0.018
67	hn	1H	8.264	0.014
67	n	15N	119.296	0.175
68	c	13C	176.938	0
68	ca	13C	53.174	0.112
68	cb	13C	41.976	0.085
68	cd1	13C	24.524	0.116
68	cd2	13C	20.852	0.06

68	cg	13C	25.577	0.108
68	ha	1H	4.174	0.018
68	hb#	1H	1.304	0
68	hb1	1H	1.331	0.018
68	hb2	1H	1.284	0.107
68	hd1#	1H	0.81	0.012
68	hd2#	1H	0.773	0.015
68	hg	1H	1.59	0.019
68	hn	1H	7.775	0.021
68	n	15N	117.038	0.179
69	ca	13C	53.1	0.141
69	cb	13C	35.74	0.135
69	ha	1H	3.943	0.011
69	hb1	1H	3.03	0.008
69	hb2	1H	2.758	0.016
69	hn	1H	8.171	0.027
69	n	15N	117.375	0.143
70	ca	13C	53.634	0.148
70	cb	13C	35.736	0.042
70	ha	1H	4.62	0.004
70	hn	1H	7.009	0.013
70	n	15N	113.681	0.184
71	c	13C	176.785	0.012
71	ca	13C	55.751	0.17
71	cb	13C	28.924	0.159
71	cd1	13C	128.268	0.045
71	ce3	13C	119.431	0.037
71	ch2	13C	123.549	0.035
71	cz2	13C	114.98	0.037
71	h#	1H	7.19	0.107
71	ha	1H	5.139	0.014
71	hb1	1H	3.044	0.016

71	hb2	1H	3.229	0.01
71	hd1	1H	7.529	0.004
71	he1	1H	10.321	0.007
71	he3	1H	7.32	0.012
71	hh2	1H	6.778	0.008
71	hn	1H	8.783	0.019
71	hz2	1H	7.286	0.016
71	n	15N	121.885	0.176
71	ne1	15N	131.549	0.112
72	c	13C	175.439	0.024
72	ca	13C	57.816	0.153
72	cb	13C	34.216	0.125
72	cg1	13C	20.369	0.385
72	cg2	13C	17.725	0.97
72	ha	1H	4.903	0.007
72	hb	1H	2.359	0.015
72	hg1#	1H	0.949	0.009
72	hg2#	1H	0.955	0.014
72	hn	1H	9.692	0.014
72	n	15N	118.73	0.151
73	ca	13C	55.429	0.107
73	cb	13C	39.838	0.016
73	ha	1H	4.749	0.011
73	hn	1H	8.848	0.016
73	n	15N	123.194	0.143
74	c	13C	174.39	0.048
74	ca	13C	53.685	0.149
74	cb	13C	40.346	0.247
74	cd#	13C	22.854	0.076
74	cg	13C	27.665	0.094
74	ha	1H	4.535	0.028
74	hb#	1H	2.551	0.027

74	hd#	1H	1.264	0.021
74	hg	1H	1.502	0.057
74	hn	1H	8.676	0.016
74	n	15N	125.684	0.122
75	c	13C	175.804	0.013
75	ca	13C	60.045	0.111
75	cb	13C	39.599	0.246
75	cd1	13C	11.868	0.103
75	cg1	13C	25.44	0.036
75	ha	1H	4.511	0.023
75	hb	1H	1.984	0.016
75	hd1#	1H	0.905	0.013
75	hg11	1H	1.227	0.016
75	hg12	1H	1.382	0.007
75	hn	1H	9.536	0.016
75	n	15N	125.355	0.23
76	c	13C	176.334	0.004
76	ca	13C	54.003	0.119
76	cb	13C	33.792	0.013
76	cg	13C	26.404	0.29
76	ha	1H	4.757	0.076
76	hb#	1H	1.298	0.006
76	hg#	1H	0.857	0.017
76	hn	1H	8.727	0.021
76	n	15N	120.539	0.12
77	c	13C	177.281	0.024
77	ca	13C	58.665	0.106
77	cb	13C	27.456	0.159
77	ha	1H	3.829	0.014
77	hb1	1H	2.194	0.021
77	hb2	1H	1.983	0.021
77	hn	1H	9.306	0.026

77	n	15N	122.107	0.194
78	c	13C	176.922	0.013
78	ca	13C	53.9	0.055
78	cb	13C	38.605	0.146
78	ha	1H	4.787	0.007
78	hb1	1H	2.84	0.001
78	hb2	1H	2.592	0
78	hn	1H	8.116	0.017
78	n	15N	115.471	0.176
79	c	13C	177.179	0
79	ca	13C	56.684	0.186
79	cb	13C	32.03	0
79	cg	13C	35.854	0.088
79	ha	1H	4.107	0.016
79	he1	1H	7.053	0.002
79	he2	1H	7.93	0.004
79	hg#	1H	2.514	0.01
79	hn	1H	7.589	0.014
79	n	15N	116.954	0.125
79	ne	15N	109.518	0.1
80	c	13C	176.537	0.007
80	ca	13C	55.009	0.166
80	cb	13C	42.59	0.001
80	cd#	13C	24.466	0.04
80	ha	1H	4.279	0.016
80	hd#	1H	0.925	0.018
80	hn	1H	7.525	0.014
80	n	15N	114.931	0.172
81	c	13C	173.632	0.025
81	ca	13C	58.893	0.077
81	cb	13C	71.124	0.01
81	cg	13C	20.811	0.064

81	ha	1H	4.798	0.007
81	hg#	1H	1.277	0.011
81	hn	1H	7.243	0.017
81	n	15N	111.532	0.196
82	c	13C	177.139	0.037
82	ca	13C	55.09	0.095
82	cb	13C	40.164	0.125
82	ha	1H	3.659	0.007
82	hb1	1H	2.303	0.017
82	hb2	1H	2.415	0.013
82	hn	1H	8.434	0.026
82	n	15N	121.672	0.188
83	c	13C	175.764	0.002
83	ca	13C	59.897	0.091
83	cb	13C	37.491	0.157
83	cd#	13C	132.883	0.044
83	ce	13C	117.864	0.037
83	ce#	13C	117.78	0
83	ha	1H	3.536	0.032
83	hb1	1H	2.825	0.013
83	hb2	1H	3.434	0.016
83	hd#	1H	7.028	0.014
83	he#	1H	6.685	0.012
83	hn	1H	9.623	0.03
83	n	15N	125.759	0.094
84	c	13C	170.458	0.067
84	ca	13C	56.588	0.162
84	cb	13C	27.649	0.093
84	ha	1H	4.572	0.013
84	hb1	1H	3.133	0.016
84	hb2	1H	3.58	0.012
84	hn	1H	8.086	0.016

84	n	15N	116.406	0.16
85	ca	13C	53.66	0.172
85	cb	13C	28.92	0.696
85	cg	13C	35.437	0.216
85	ha	1H	4.958	0.013
85	hb#	1H	1.974	0.027
85	hg#	1H	2.333	0.013
85	hn	1H	9.336	0.013
85	n	15N	119.803	0.166
86	ca	13C	51.761	0.11
86	cb	13C	43.592	0.163
86	cd#	13C	23.243	0.126
86	cg	13C	26.41	0.112
86	ha	1H	6.136	0.019
86	hb#	1H	2.243	0.046
86	hd#	1H	1.059	0.025
86	hg	1H	0.944	0.016
86	hn	1H	9.55	0.05
86	n	15N	126.206	0.161
87	c	13C	173.274	0
87	ca	13C	56.408	0.196
87	cb	13C	41.175	0.117
87	cd#	13C	133.107	0.046
87	ce#	13C	117.063	0.021
87	ha	1H	5.193	0.014
87	hb#	1H	2.01	0
87	hd#	1H	6.113	0.007
87	he#	1H	5.711	0.025
87	hh	1H	8.7	0
87	hn	1H	9.704	0.073
87	n	15N	124.878	0.191
88	c	13C	173.695	0.011

88	ca	13C	60.442	0.175
88	cb	13C	31.882	0.099
88	cg1	13C	20.379	0.506
88	cg2	13C	21.728	0.053
88	ha	1H	4.738	0.009
88	hb	1H	1.934	0.211
88	hg1#	1H	1.077	0.22
88	hg2#	1H	1.305	0.114
88	hn	1H	8.197	0.027
88	n	15N	128.251	0.17
89	c	13C	175.594	0
89	ca	13C	57.083	0.172
89	cb	13C	40.211	0.292
89	cd#	13C	131.166	0.05
89	ce#	13C	132.538	0.077
89	ha	1H	4.568	0.002
89	hb#	1H	3.029	0.018
89	hd#	1H	7.093	0.009
89	he#	1H	7.392	0.013
89	hn	1H	8.857	0.019
89	hz	1H	6.844	0
89	n	15N	125.336	0.112
90	ca	13C	53.23	0.167
90	cb	13C	31.523	0
90	ha	1H	5.341	0.011
90	hn	1H	8.521	0.027
90	n	15N	118.285	0.174
91	ca	13C	63.355	0.077
91	cb	13C	30.623	0
91	cd	13C	49.084	0.002
91	cg	13C	25.63	0
91	ha	1H	4.14	0.005

91	hb#	1H	1.837	0
91	hd#	1H	3.204	0.001
91	hg#	1H	2.134	0
91	n	15N	115.026	0
92	c	13C	175.79	0
92	ca	13C	62.085	0.024
93	ca	13C	52.76	0
93	ha	1H	4.086	0.004
93	hb#	1H	1.301	0.007
93	hn	1H	7.895	0.014
93	n	15N	129.941	0.127
94	c	13C	176.472	0.019
94	ca	13C	56.442	0.038
94	ha	1H	4.768	0.002
94	hn	1H	8.154	0.003
94	n	15N	116.822	0.163
95	c	13C	178.553	0
95	ca	13C	57.79	0.113
95	cb	13C	29.392	0.152
95	cd1	13C	126.23	0.074
95	ce3	13C	124.254	0.082
95	ch2	13C	121.448	0.063
95	cz2	13C	114.415	0.044
95	ha	1H	4.71	0.012
95	hb1	1H	2.172	0.022
95	hb2	1H	2.848	0.011
95	hd1	1H	6.978	0.008
95	he1	1H	10.164	0.013
95	he3	1H	7.124	0.01
95	hh2	1H	6.795	0.013
95	hn	1H	7.443	0.02
95	hz2	1H	7.369	0.003

95	n	15N	117.276	0.159
95	ne1	15N	129.4	0.11
96	c	13C	175.287	0.008
96	ca	13C	53.688	0.11
96	cb	13C	31.404	0.022
96	cd2	13C	128.767	0.034
96	ce1	13C	132.819	3.431
96	ha	1H	4.963	0.001
96	hd2	1H	6.686	0.006
96	he1	1H	7.136	0.02
96	hn	1H	8.578	0.023
96	n	15N	119.616	0.182
97	c	13C	175.296	0
97	ca	13C	54.256	0.963
97	cb	13C	33.26	0.133
97	ha	1H	4.53	0.014
97	hb#	1H	1.74	0.019
97	hn	1H	8.663	0.036
97	n	15N	124.949	0.144
98	c	13C	176.262	0
98	ca	13C	55.303	1.014
98	cb	13C	29.037	0
98	ha	1H	4.773	0
98	hb#	1H	2.263	0.005
98	hn	1H	8.612	0.015
98	n	15N	122.717	0.114
99	ca	13C	56.283	0.148
99	cb	13C	66.005	0.105
99	ha	1H	4.826	0.029
99	hb1	1H	4.029	0.001
99	hb2	1H	3.831	0.007
99	hn	1H	8.238	0.103

99	n	15N	120.989	0.434
100	c	13C	175.603	0
100	ca	13C	54.576	0.869
100	ha	1H	4.781	0
100	hn	1H	8.239	0.133
100	n	15N	123.467	0.999
101	c	13C	176.011	0.036
101	ca	13C	56.113	0.103
101	cb	13C	33.508	0.067
101	ha	1H	4.78	0.003
101	hn	1H	7.339	0.014
101	n	15N	119.556	0.195
102	c	13C	176.058	0.012
102	ca	13C	55.167	0.122
102	cb	13C	28.974	0.165
102	cg	13C	35.047	0.052
102	ha	1H	4.044	0.018
102	hb#	1H	1.868	0.01
102	hg#	1H	2.237	0.01
102	hn	1H	8.506	0.054
102	n	15N	120.28	0.135
103	c	13C	174.491	0
103	ca	13C	58.695	0.125
103	cb	13C	37.06	0.084
103	cd1	13C	11.984	0.078
103	cg1	13C	28.61	0.094
103	cg2	13C	16.612	0.131
103	ha	1H	3.927	0.03
103	hb	1H	1.691	0.035
103	hd1#	1H	0.956	0.022
103	hg1#	1H	0.657	0.011
103	hg2#	1H	0.855	0.021

103	hn	1H	8.547	0.036
103	n	15N	124.001	0.106
105	c	13C	176.72	0
105	ca	13C	61.702	0.33
105	cb	13C	30.859	0.056
105	ha	1H	4.368	0.026
106	c	13C	177.824	0.021
106	ca	13C	51.771	0.137
106	cb	13C	17.804	0.16
106	ha	1H	4.047	0.014
106	hb#	1H	1.386	0.012
106	hn	1H	8.529	0.019
106	n	15N	125.34	0.106
107	c	13C	175.822	0.006
107	ca	13C	52.194	0.126
107	cb	13C	35.703	0.16
107	ce	13C	16.038	0.025
107	cg	13C	30.14	0.044
107	ha	1H	4.975	0.019
107	hb#	1H	2.391	0.259
107	he#	1H	2.195	0.006
107	hg#	1H	2.758	0.014
107	hn	1H	8.513	0.02
107	n	15N	119.863	0.134
108	c	13C	174.241	0
108	ca	13C	54.057	0.05
108	cb	13C	30.358	0.139
108	cd	13C	27.87	0.072
108	ce	13C	41.099	0.032
108	cg	13C	23.871	0.036
108	ha	1H	4.658	0.004
108	hb#	1H	1.817	0.013

108	hd#	1H	1.685	0.012
108	he#	1H	3.016	0.005
108	hg#	1H	1.568	0.027
108	hn	1H	8.741	0.016
108	n	15N	123.688	0.167

CURRICULUM VITAE

PERSONAL INFORMATION

Full name : KENI VIDILASERIS

Sex : Male

Place of birth : Cilacap

Date of birth : July 23th 1985

Nationality : Indonesian

Languages : English
Indonesian (native)

Address : Hafengasse 7/11
1030 Wien, Austria

Phone : +43-1-4277-61626 (Lab)
: +436507578254 (mobile)

E-Mail : keni.vidilaseris@univie.ac.at
keni105@yahoo.com

ACADEMIC BACKGROUND

2009-present : Ph.D student in Max F. Perutz Laboratory, Vienna University, under supervision of Dr. Gang Dong

2007-2008 : M.Si with distinction (*Cum laude*) in Chemistry

GPA 4.0 (scale 0-4)

Department of Chemistry, Bandung Institute of Technology,
Indonesia

2003-2007 : S.Si with distinction (*Cum laude*) in Chemistry

GPA 3.84 (scale 0-4)

Department of Chemistry, Bandung Institute of Technology,
Indonesia

RESEARCH INTERESTS

My main interest is to elucidate the protein structure and protein-protein interactions by X-ray crystallography and NMR spectroscopy as well as to characterize their properties using other biophysical/biochemical techniques such as circular dichroism (CD), isothermal calorimetry (ITC), and thermofluor. I am also interested in understanding the roles of protein functions within the cell using immunofluorescence technique.

RESEARCH EXPERIENCES

- 2009-present : Structural studies of *Trypanosoma brucei* BILB01, a protein essential for flagellar pocket biogenesis and cell survival (under supervision of Dr. Gang Dong, Computational and Structural Biology Department - MFPL, Medical University of Vienna)
- 2007-2008 : Properties of amylolytic enzymes from *Saccharomycopsis fibuligera* R64 (under supervision of Dr. Dessy Natalia, Chemistry Department – Bandung Institute of Technology (ITB) and Prof. Bauke Dijkstra, Department of Protein Crystallography, University of Groningen, The Netherlands)
- 2006-2007 : Characterization of raw starch degradation α -amylase of marine *Bacillus subtilis* ALSHL3 (under supervision of Dr. Dessy Natalia, Chemistry Department - Bandung Institute of Technology (ITB))
- 2006 : Organic tool construction using ultraviolet emitted nanoparticle and photocatalyst Titanium Oxide.
- 2006 : Production and characterization of Virgin Coconut Oil

PUBLICATIONS

- 2014 : **Vidilaseris, Keni; Morriswood, Brooke; Dong, Gang (2014). Assembly mechanism of TbBILB01 at the flagellar pocket collar of *Trypanosoma brucei*. (Submitted)**
- 2013 : **Vidilaseris, Keni; Dong, Gang (2013). Expression, purification and preliminary crystallographic analysis of the N-terminal**

domain of *Trypanosoma brucei* BILBO1. (Submitted)

- 2013 : **Vidilaseris, Keni**; Morriswood, Brooke; Kontaxis, Georg; Dong, Gang (2013) **Structure of the TbBILBO1 N-terminal domain from *Trypanosoma brucei* reveals an essential requirement for a conserved surface patch.** *J Biol Chem*. PMID:24362019
- 2013 : Morriswood, Brooke; Havlicek, Katharina; Demmel, Lars; Yavuz, Sevil; Sealey-Cardona, Marco; **Vidilaseris, Keni**; Anrather, Dorothea; Kostan, Julius; DjinoVIC-Carugo, Kristina; Roux, Kyle; Warren, Graham (2013). **Novel bilobe components in *Trypanosoma brucei* identified using proximity-dependent biotinylation.** *EUKARYOT CELL*;12(2):356-67. PMID: 23264645
- 2012 : Esson, Heather J; Morriswood, Brooke; Yavuz, Sevil; **Vidilaseris, Keni**; Dong, Gang; Warren, Graham (2012). **Morphology of the trypanosome bilobe, a novel cytoskeletal structure.** *EUKARYOT CELL*;11(6):761-772 . PMID: 22327007
- 2011 : Natalia, D., **Vidilaseris, K.**, Satrimafitrah, P., Ismaya, W., Purkan, Permentier H., Fibriansah, G., Puspasari, F., Nurachman, Z., Dijkstra, B., Soemitro, S. 2011. **Biochemical characterization of a glucoamylase from *Saccharomycopsis fibuligera* R64.** *Biologia*. 66(1). p. 27-32.
- 2009 : **Vidilaseris, K.**, Hidayat, K., Retnoningrum, D., Nurachman, Z., Noer, A., Natalia, D. 2009. **Biochemical characterization of a raw starch degrading α -amylase from the Indonesian marine bacterium *Bacillus* sp. ALSHL3.** *Biologia*, 64(6), p. 1047-1052

ACHIEVEMENTS, AWARDS AND SCHOLARSHIPS

- 2013 : Best poster presentation on the occasion of the MFPL Scientific Advisory Board meeting 2013, Vienna, Austria
- 2013 : Best oral presentation award at the CFC3013 conference, Marseilles, France
- 2009-2012 : The ASEAN-European Academic University Network (ASEA-UNINET) PhD scholarship from the Austrian Federal Ministry of Education, Science and Culture through the Austrian Council for Science and Technology Development.
- 2007-2008 : Fast-Track Sandwich Master Student of Bandung Institute of Technology (ITB), Indonesia - University of Groningen (RuG), The Netherlands
- 2007-2008 : Unggulan scholarship from Department of National Education, Indonesia
- 2004-2007 : Dean's List for Academic Performance, Faculty Mathematics and Natural Science, Bandung Institute of Technology (dedicated for students who earn grade point average of 3.5 or higher, first introduced in 2004)
- 2003-2007 : TPSDP scholarship from Department of National Education, Indonesia

TRAINING/WORKSHOP/SEMINAR

- 2013 : MFPL Scientific Advisory Board meeting 2013, held in Vienna, Austria
- 2013 : CFC2013 conference, held in Marseilles, France
- 2012 : ASCB meeting 2012, held in San Francisco, USA
- 2012 : 4th Austrian Association of Molecular Life Science and Biotechnology (OGMBT) Meeting, held in Graz, Austria
- 2012 : LRZ life science molecular modeling workshop and demo, held in Munich, Germany.
- 2007 : International meeting of the second symposium and workshop on carbohydrates and carbohydrate acting enzymes bioengineering, held in Indonesia University
- 2007 : Australian education international seminar series in science, held in Australian Embassy, Jakarta, Indonesia
- 2006 : Gruber-Soedigdo join lecture of ITB and University of Groningen, held in Bandung Institute of Technology
- 2006 : International Conference on Mathematics and Natural Sciences, held in Bandung Institute of Technology
- 2005 : Training of event organizer and journalistic, held in Bandung Institute of Technology

WORKING EXPERIENCES

- 2007 - 2009 : Senior assistant of basic chemistry experiment in Bandung Institute of Technology
- 2007 : Private teacher of chemistry for first year university students
- 2006 and 2007 : Trainer of Success strategy in campus
- 2006 : Coordinator of simple chemistry training in Chemistry EXPO 2006
- 2004 : Private teacher of chemistry for senior high school student
- 2004-2007 : Laboratory assistant of basic chemistry, biochemistry, and physical chemistry in Chemistry Department, Bandung Institute of Technology

ORGANIZATIONAL EXPERIENCES

- 2003-2007 : Board of Chemistry Student Association (AMISCA), Bandung Institute of Technology (ITB)
- 2003-2007 : Broad of Chemistry Moslem Community KAMAMUKI, ITB
- 2003 : Member of Mata' Salman, ITB

I hereby certify that all information submitted on this application is true and accurate to the best of my knowledge.